Connecting Galaxy Formation and Galaxy Clustering

by Geraint John Alan Harker

A thesis submitted to the University of Durham
in accordance with the regulations for
admittance to the Degree of Doctor of Philosophy.

Department of Physics
University of Durham
January 2007

Connecting Galaxy Formation and Galaxy Clustering

by Geraint John Alan Harker

PhD Thesis, January 2007

Abstract

We study the environmental dependence of the formation history of dark matter haloes in a large dark matter simulation, the Millennium Run. Adopting a sensitive test of this dependence — the marked correlation function — reveals highly significant evidence that haloes of a given mass form earlier in denser regions. We explore the effect further using a new variant of this statistic, and confirm our results using some simpler tests made possible by the size and resolution of the simulation.

We go on to study the effect of this environmental dependence on the galaxy population generated by a recent semi-analytic model run in the Millennium Run. We show that environmentally dependent halo formation imparts a small but cleanly detected change to the correlation function and void probability function of galaxies. We can model this change by applying a modulation based on local density to the halo occupation distribution of galaxies. We also note that having the correct placement scheme for galaxies within haloes is at least as important as correctly accounting for environmental effects.

Two more dark matter simulations are run, and their outputs are appropriately relabelled and rescaled to represent different cosmologies. We generate consistent semi-analytic galaxy populations in these simulations, using two versions of each of three variants of our semi-analytic model. We compare the predictions for the galaxy clustering from these models to the projected two-point correlation function of the SDSS, obtaining a constraint on the amplitude of the fluctuations in the mass, $\sigma_8 = 0.96 \pm 0.05$. We find that environmental effects do not significantly affect this estimate, but discuss other possible effects which might. We remark on how this result compares to other recent determinations of σ_8.

Contents

List of Figures

List of Tables

Declaration

The work described in this thesis was undertaken between 2003 and 2006 while the author was a research student under the supervision of Prof. Shaun Cole in the Department of Physics at the University of Durham. This work has not been submitted for any other degree at the University of Durham or any other University.

Portions of this work have appeared in the paper, 'A marked correlation function analysis of halo formation times in the Millennium Simulation' by Harker, Geraint J. A.; Cole, Shaun M.; Helly, John C.; Frenk, C.S. & Jenkins, Adrian R: *MNRAS* **367**, 1039.

Acknowledgements

Thanks firstly to Shaun: for great depths of insight and patience; for finding a fascinating project for me to work on; and for taking on a mathematician, whom some suspect of playing more bridge than is good for him, as a student in the first place. One couldn't hope for a better supervisor.

The data used in this thesis are the fruit of the time, effort and skill of a large number of people. John Helly, in particular, provided the code to read in the N-body simulations and constructed the merger trees on which the results of Chapters 2 and 3 are based. Adrian Jenkins generated the initial conditions for, and ran, the simulations used in Chapter 4. The other members of the Virgo Consortium, and the creators of GADGET and GALFORM, have enabled this project to go ahead.

John, Adrian, Shaun and Carlos Frenk offered many helpful suggestions to improve the paper upon which Chapter 2 is based. I must, however, thank Liang Gao and the anonymous referee for spotting an error which sneaked past us all. Gao, Darren Croton and Jeremy Tinker generously shared data, code and some useful insights, while David Weinberg helped to initiate and plan the project described in Chapter 4.

Many of my memories of studying for a PhD will concern playing bridge. I'd like to thank my regular competition partners, Adam Matthews and Phil Smith; many semi-regular and occasional partners; the friendlier of my opponents; and all the members of Durham University Bridge Club. I never thought DUBC would give me the chance to take part in a World Championships in China; thanks to Robin Zigmond, Tom Dessain, Nicola Macdougall, John Probst and many generous bridge players for making it possible.

Thanks to Małgosia Sobolewska and Nick Schurch for being crazy enough to let a writing up PhD student live in their spare room; to my officemates who've had no choice but to put up with me, in particular to Rowena Malbon and Dave Wilman who helped show me the ropes when I turned up; to many other members of the group who've kept me sane by coming out for drinks, kept me busy as a goalkeeper for Astro, and kept me amused at coffee time; to Chris Simpson for showing that coffee time is a flexible concept; to Lydia Heck and Alan Lotts for keeping everything running and saving me from the dreaded 'rm *'; to Saleem Zaroubi for providing me with a deadline; and to PPARC for a studentship that nearly lasted until that deadline.

Finally, I would be lost without the knowledge my parents are always there to encourage and support me whatever I do. I can never thank them enough.

Chapter 1 | *Introduction*

1.1 Background

1.1.1 Overview

On the largest scales accessible to study, observations of the Universe are consistent with it being homogeneous and isotropic. That this should be the case is the cherished 'cosmological principle'. Adopting this principle allows us to characterize the evolution of the Universe on these large scales — in particular its density and rate of expansion — in terms of just a few parameters which describe the contribution of different components to the energy density of the Universe.

Fortunately for cosmologists, however, the Universe displays a great wealth of structure on smaller scales. In the early, high redshift Universe, this structure was imprinted as small fluctuations in the temperature of the cosmic microwave background (CMB) radiation, which have been measured to increasingly high precision by many experiments. At moderate and low redshifts, though, the structure is seen most strikingly in the spatial distribution of galaxies. Galaxy redshift surveys, most notably in recent times the Two-degree Field Galaxy Redshift Survey (2dFGRS; Colless et al., 2001) and the Sloan Digital Sky Survey (SDSS; York et al., 2000), produce maps of galaxy positions in three dimensions which show that galaxies form a beautiful network of walls and filaments, which resolve on closer inspection into groups of between one galaxy and thousands of galaxies.

Producing the rich structure seen in the galaxy distribution from the small initial fluctuations seen in the CMB requires that the fluctuations grow under the influence of gravity: matter streaming into larger structures, with progressively deeper potential wells forming. If the gas becomes dense enough to start to cool, creating even denser clouds in which stars can form, these potential wells provide the sites for the formation of galaxies. Clearly, then, the formation of galaxies, in addition to involving a great deal of physics concerning the gas, stars, dust, black holes and other objects which interact in

the galaxy's potential well, is closely related to the growth of structure in the Universe. Conversely, if we wish to study the growth of large-scale structure — which itself provides insight into the composition of the Universe, its initial conditions and the gravitational physics at play — we must also understand the galaxies which light up this structure for us. In this thesis we explore some of the connections between galaxy formation and the large-scale structure of the Universe, as quantified by the statistics of galaxy clustering. Our modelling of galaxy formation is performed with an eye to improving the constraints that galaxy clustering statistics can provide on cosmological parameters. We will see, also, that examining how galaxies cluster can provide us with information about the physics of galaxy formation.

We are able to perform a detailed analysis of the connections between galaxy formation and large-scale structure because we have a robust framework in which each can be studied and understood. This framework, which comprises a description of the components contributing to the energy density of the Universe, the form and origin of the initial conditions and the physics governing the growth of structure, is known as the Lambda Cold Dark Matter (ΛCDM) cosmogony. We give a brief description of this framework below.

1.1.2 The ΛCDM cosmogony

In the light of alternative theories proposed to explain certain observations which are normally considered to be evidence for dark matter (Milgrom, 1983; Bekenstein, 2004; Moffat, 2006), it is perhaps worth stating that ΛCDM is a general relativistic theory. Therefore on the assumption of homogeneity and isotropy on large scales, we have the Friedmann-Robertson-Walker (FRW) metric,

$$\mathrm{d}s^2 = -c^2\mathrm{d}t^2 + a^2(t)\left[\frac{\mathrm{d}r^2}{1-kr^2} + r^2(\mathrm{d}\theta^2 + \sin^2\theta\mathrm{d}\phi^2)\right] \quad , \tag{1.1}$$

where $k = +1, 0$ or -1 if the spatial hypersurfaces have positive, zero or negative curvature respectively. The evolution of the scale factor, a (that is, the expansion of the Universe), is determined by the Friedmann equation:

$$H^2(a) = H_0^2\left[\Omega_\Lambda + \Omega_\mathrm{m}a^{-3} + \Omega_\mathrm{r}a^{-4} - (\Omega_\mathrm{tot} - 1)a^{-2}\right] \quad , \tag{1.2}$$

where a is conventionally taken to be equal to 1 at the present day, so that redshift, z, is given by $a = 1/(1+z)$. The Hubble parameter, $H \equiv \dot{a}/a$, gives the instantaneous rate of expansion of the Universe, and H_0 is its present value. We adopt the common notation

$H \equiv 100\ h$ km s^{-1} Mpc^{-1}. The different terms on the right-hand side of the Friedmann equation correspond to different components of the energy density of the Universe. The different Ω parameters give the density at the present day of each component, normalized to the critical density; that is,

$$\Omega_i \equiv \frac{\rho_i}{\rho_{\rm crit}} = \frac{8\pi G\rho_i}{3H_0^2} \quad . \tag{1.3}$$

The critical density is the density such that if the only density contribution to the Universe were from ordinary matter, then a universe with higher density would recollapse and a universe with lower density would expand forever, corresponding to closed and open geometries respectively (the critical case being a flat geometry). In ΛCDM we account for contributions from radiation, $\Omega_{\rm r}$ (negligible in the present, matter-dominated epoch), matter, $\Omega_{\rm m}$, a cosmological constant, Ω_Λ, and a curvature term (where the curvature is determined by the total energy density of the other components, hence the entry into the equations of $\Omega_{\rm tot}$). Since static solutions (with constant a) are unstable, this in principle is a prediction of an expanding or contracting universe; in practice, this was only appreciated following the observations of Hubble (1929).

The distinctive feature of cold dark matter (CDM) models is that some (usually most) of the mass accounted for by the matter term in the Friedmann equation is in the form of particles which interact only through gravity (and perhaps the weak force) and which are non-relativistic ('cold') at decoupling. Some form of dark matter was originally proposed to account for missing mass suggested by the dynamics of the luminous matter in clusters of galaxies (Zwicky, 1937) and, later, in individual spiral galaxies (Bosma, 1978; Rubin et al., 1980). Measurements of the mass of clusters of galaxies through gravitational lensing also imply a large amount of unseen mass (Clowe et al., 2006). So long as all we require is some kind of mass, these observations could in principle be accounted for by baryons sequestered away in dense, dark objects. Baryons, however, are able to support pressure and behave differently from cold, weakly interacting particles. In the early Universe they can couple strongly to photons leading to a different signature in the CMB; later, they affect the details of structure formation. Baryons are also able to take part in the primordial synthesis of light nuclei (Alpher et al., 1948; Gamow, 1948): the abundance of these nuclei (especially deuterium) constrains the density of baryons at nucleosynthesis. For example, Burles et al. (2001) quote $\Omega_{\rm b}h^2 = 0.020 \pm 0.002$ to 95 per cent confidence, while the analysis of a QSO spectrum by O'Meara et al. (2001) gives $\Omega_{\rm b}h^2 = 0.0205 \pm 0.0018$. It has been suggested that the dark matter could be in the form of neutrinos,

which also interact only through gravity and the weak force. However, since these are relativistic at decoupling, if they comprised a large fraction of the Universe's mass then they would quickly stream out of overdense regions in the early Universe and would wash out small scale structure to an extent incompatible with observations. A recent analysis by Tegmark et al. (2006) gives $\Omega_\nu < 0.024$ at 95 per cent confidence.

The 'Λ' in ΛCDM represents Einstein's cosmological constant. This arises as a coefficient multiplying the metric tensor in the gravitational field equations:

$$R_{\mu\nu} - \frac{1}{2}Rg_{\mu\nu} + \Lambda g_{\mu\nu} = \frac{8\pi G}{c^4}T_{\mu\nu} \quad , \tag{1.4}$$

adopting the same sign convention as Equation 1.1. Though the field equations are often written with $\Lambda = 0$, Equation 1.4 gives them in their most general form, and it can be derived from the variation of the most general form of the Einstein-Hilbert action. If the cosmological constant is expressed as a component of the energy-momentum tensor (moving the $\Lambda g_{\mu\nu}$ over to the right-hand side of Equation 1.4), it has an equation of state $p = -\rho c^2$; in other words, while it has a positive energy density, ρ, it exerts a negative pressure, p. Its effect, then, is to *accelerate* the expansion of the Universe, in contrast to matter, which slows it down. This acceleration was detected through observations of supernovae by Riess et al. (1998) and Perlmutter et al. (1999) which demonstrated that supernovae were fainter at high redshift than would be expected for a universe without Λ. Such an exotic result requires confirmation, and for this we return once more to the CMB — the radiation produced when the Universe cooled sufficiently that the 'average' photon could no longer ionize hydrogen, allowing the proton-electron plasma to recombine into hydrogen atoms and making the Universe transparent — which had already been instrumental in confirming the general picture of a universe beginning with a hot Big Bang (Dicke et al., 1965; Penzias & Wilson, 1965). The Cosmic Background Explorer (COBE) satellite confirmed that the CMB is very accurately described by a black-body spectrum (Fixsen et al., 1996) and measured anisotropies in the temperature of the radiation over the whole sky (Smoot et al., 1992; Bennett et al., 1996). Other experiments measured the anisotropies at higher resolution in limited portions of the sky (de Bernardis et al., 2000; Hanany et al., 2000). Subsequently, a breakthrough in the reliable, high precision measurement of the anisotropies arrived in the form of the Wilkinson Microwave Anisotropy Probe (WMAP; Jarosik et al., 2006), which has measured the temperature (Hinshaw et al., 2006) and polarization (Page et al., 2006) anisotropies with a view to providing tight constraints on cosmological parameters (Spergel et al., 2006). Note that

other experiments still make valuable contributions at small scales and for polarization measurements (Rajguru et al., 2005; Leitch et al., 2005). A review of the phenomenology and the cosmological implications of CMB anisotropies is given by Hu & Dodelson (2002).

The CMB contributes to detecting dark energy mainly by constraining the geometry of the Universe to be close to flat; that is, the total energy density of all its components is close to the critical density. To show that some of this is in the form of dark energy requires a constraint on the amount of matter; the remainder must then be composed of something exotic. Physical scales are imprinted on the CMB which depend on the matter density (e.g., Silk, 1968; Peebles & Yu, 1970; Sunyaev & Zel'dovich, 1970; Mészáros, 1974) and the baryon fraction (e.g., Eisenstein & Hu, 1998). The baryon acoustic peaks are particularly important. They are produced because the baryons are tightly coupled to the photons before recombination. The pressure in the photon-baryon fluid provides a restoring force to the initial fluctuations, setting up oscillations in the fluid (often likened to ripples when a stone is thrown into a pond, though in fact they are perhaps better viewed as standing waves). There are ripples of all wavelengths, and at any given time, some will be near the maximum of their oscillation and will have large amplitude, and others will be near the minimum and have small amplitude. The wavelengths with large amplitude at recombination are the ones contributing most power to the CMB anisotropies, the redshift of recombination being determined accurately by the CMB temperature. For a first estimate of these wavelengths, note that the longest wavelength mode to be at its maximum amplitude at recombination is the one that has completed half an oscillation by recombination. In other words, it has wavenumber k where $ks = \pi$ and s is the distance sound can travel before recombination: the sound horizon. Ignoring the dynamical effects of gravity and the inertia of the baryons, then because radiation has equation of state $p = \frac{1}{3}\rho c^2$ the sound speed in the fluid is $c_s \equiv \sqrt{\dot{p}/\dot{\rho}} = c/\sqrt{3}$. Therefore the sound horizon is $1/\sqrt{3}$ times the particle horizon, where the particle horizon, η_0, the maximum distance a light ray can travel since the Big Bang, is given at $t = t_0$ by

$$\int_0^{\eta_0} \frac{\mathrm{d}r}{\sqrt{1-kr^2}} = c\int_0^{t_0} \frac{\mathrm{d}t}{a(t)} \quad , \tag{1.5}$$

which is obtained by setting $\mathrm{d}s^2 = 0$ in Equation 1.1 and considering a radial photon. The scale of the acoustic peaks is given by the harmonic series $ks = n\pi$. Increasing the baryon fraction moves the peaks to a smaller scale by reducing the sound speed through inertia.

We cannot measure a physical scale, however: only an angular diameter scale on the

sky (information on the matter density is encoded in the relative heights of peaks in the CMB power spectrum, but this is a weaker signal). Hinshaw et al. (2006) measure the first acoustic peak in WMAP at $\ell = 220.7^{+0.7}_{-0.7}$, where ℓ is the multipole moment (the degree of the corresponding term in a spherical harmonic expansion) and is related to angular scale θ by $\ell \sim 1/\theta$. The precise measurement of this angular scale allows the tight constraint on the overall curvature of the Universe: in a more open universe the peak appears at a smaller angular scale, while in a more closed universe the peak appears at a larger angular scale. The relationship between physical scale and angular diameter depends on the expansion history of the Universe and therefore on the matter density. Measuring the matter density rather than just the curvature therefore requires low-redshift data to break this degeneracy, and so the first detection of dark energy from the CMB came from combining CMB data with galaxy clustering data from the 2dFGRS (Peacock et al. 2001; Percival et al. 2001; Efstathiou et al. 2002; for the final power spectrum measurement, see Cole et al. 2005). A prior on the Hubble parameter as provided by the Hubble Space Telescope (HST) Key Project (Freedman et al., 2001) also helps to break the degeneracy. Naturally, the SDSS power spectrum (Tegmark et al., 2004) can also be used for these measurements, and provides similar results.

If we express the equation of state of the dark energy as $p = w\rho c^2$ then $w = -1$ for the Einstein cosmological constant. Arguably, we could have $w > -1$, and possibly a w not constant with time, without drastically changing the overall ΛCDM picture. Spergel et al. (2006) quote $w = -1.062^{+0.128}_{-0.079}$ from combining their WMAP data with the 2dFGRS and SDSS power spectra, and with supernova measurements. If $w \neq -1$ there is no particular reason why it should be constant with time, as it cannot then be Einstein's cosmological constant (see Peebles & Ratra 2003 for a review of dark energy physics). Current measurements cannot tightly constrain the possible time evolution of w, though many efforts are under way. Given a standard ruler the physical length of which is known or can be inferred at some other time, such as the 'baryon wiggles' which are the relics in the galaxy population of the acoustic peaks and occur at $\sim 100\ h^{-1}$ Mpc, geometrical tests measure the evolution of its apparent length, or the difference between looking along and across the line of sight: the Alcock-Paczynski (1979) test. The baryon wiggles are discussed (and measured) by, for example, Cole et al. (2005), Eisenstein et al. (2005) and Tegmark et al. (2006). When dark energy begins to dominate the energy density it also slows down the rate of structure formation, leading to a variety of more complex tests involving cluster abundances (e.g., Jassal et al., 2005), weak lensing (Refregier, 2003), the

integrated Sachs-Wolfe (1967) effect, and so on.

The final piece of this general description of the model is the initial conditions. We have alluded to these several times above, since consideration and measurement of the 'background' cosmology, and of the perturbations to it, are closely linked. The standard picture is that the perturbations were seeded by quantum fluctuations during a period when the Universe underwent exponential inflation (Guth, 1981; Linde, 1982). Inflation was proposed to solve the 'flatness problem' (the density of the Universe is quite close to the critical density, and if it is not precisely this density it must have been even closer to it in the early Universe) and the 'horizon problem' (the temperature of the Universe is rather homogeneous; portions of it that could never have been in causal contact without a period of inflation have very similar temperatures). It also gives licence to theories which predict exotic topological defects (such as monopoles) in the early Universe by dispersing them rather widely and giving them an unobservably low space density at the present.

If we express the density contrast, $\delta(\boldsymbol{x}) \equiv (\rho(\boldsymbol{x}) - \bar{\rho})/\bar{\rho}$ in terms of its Fourier components δ_k, then the power spectrum $P(k) \equiv |\delta_k|^2$ gives the amount of power in density fluctuations of different wavelength. Inflation predicts a primordial spectrum of scalar fluctuations approximately given by $P(k) \propto k^n$ — 'scale-free' initial conditions. In addition, it predicts that n should be close to unity: the Harrison-Zel'dovich or scale-invariant spectrum (Harrison, 1970; Peebles & Yu, 1970; Zel'dovich, 1972), so called because the dimensionless power spectrum of *potential* perturbations is independent of k. $\delta(\boldsymbol{x})$ is a Gaussian random field with random phases and with mode amplitudes given by the above spectrum, so that $P(k)$ gives a complete statistical description of the density fluctuations. These more detailed predictions of inflationary models have also been upheld by CMB observations. For example, by combining the WMAP data with clustering data from the SDSS Luminous Red Galaxy (LRG) survey, Tegmark et al. (2006) find $n = 0.953 \pm 0.016$ for a flat, power-law ΛCDM cosmology; WMAP on its own actually gives similarly tight constraints. The constraints change if n is not assumed to be a constant (giving a 'running' spectral index) and become less tight. Clustering measurements on smaller scales than the CMB, such as the galaxy power spectrum and the Lyman alpha forest power spectrum (Croft et al., 1998; Seljak et al., 2006), then become more important. These measurements do not as yet require a running spectral index. In their joint analysis of WMAP, the SDSS power spectrum, supernova data and the Lyα forest power spectrum, Seljak et al. (2006) find $\alpha = -0.015 \pm 0.012$ (1σ errors) where $\alpha \equiv \mathrm{d}n/\mathrm{d}\ln k$. In the Ly$\alpha$ forest technique, very small-scale fluctuations are measured by studying absorption fea-

tures caused by intervening clumps of neutral hydrogen in the spectra of distant quasars.

Some inflationary models also predict tensor fluctuations, which are as yet unobserved (Tegmark et al. 2006 only place a 95 per cent upper limit of 0.33 on the ratio of the power in tensor modes to that in scalar modes at $k = 0.002$ Mpc^{-1}), but may be detectable in future CMB polarization measurements or by gravitational wave detectors. Usually it is assumed that density fluctuations affect all the matter and radiation components of the Universe equally: adiabatic perturbations. There is no evidence that there are perturbations which affect the relative densities of different components, keeping the overall density constant — isocurvature perturbations — though they are not completely ruled out. For example, Seljak et al. (2006) quote 1σ limits on the ratio of the amplitude of correlated isocurvature modes to adiabatic modes in the baryons and dark matter respectively as $A_{\rm iso,bar} = -0.06 \pm 0.18$ and $A_{\rm iso,CDM} = -0.007^{+0.034}_{-0.035}$.

The primordial perturbations do not remain untouched for long. They grow via gravity, in a manner well described by linear perturbation theory until well after the CMB is generated. Fluctuations at different scales grow at different rates; for example, the growth of matter perturbations at scales smaller than the horizon is suppressed before matter-radiation equality (Mészáros, 1974), making the horizon size at this epoch a characteristic scale imprinted on the power spectrum by the physics of the early Universe. Baryons, amongst their other effects (Peacock & Dodds, 1994; Sugiyama, 1995), impart a series of acoustic peaks at a scale depending on the time at which protons and electrons recombine into atoms, as described above. The overall effect is that by the time the CMB is generated, the power spectrum of density fluctuations has been processed to give a spectrum $P(k) = Ak^n|T(k)|^2$ where $T(k)$ is the CDM transfer function and A is a constant. Fully modelling this transfer function involves a great deal of physics (Seljak & Zaldarriaga, 1996, and references therein), and various functional forms have been proposed to fit $T(k)$ (e.g., Bardeen et al., 1986; Bond & Efstathiou, 1987; Eisenstein & Hu, 1999). The normalization, A, is usually fixed by matching the amplitude of fluctuations in spheres of radius 8 h^{-1} Mpc extrapolated by linear theory to $z = 0$, σ_8. We merely note that given a CDM model with a specified primordial power spectrum and composition, there are well-defined methods of evolving the perturbations in the linear regime, through matter-radiation equality and through recombination. It is the subsequent processes after this epoch has been reached which will concern us for the remainder of this thesis.

Once we reach this stage, because we assume that the matter density is dominated by the cold, collisionless CDM particles, the formation of structure is also dominated by

these particles. Conveniently, we therefore need consider only gravitational physics when modelling the matter distribution in CDM. Gravity continues to amplify the perturbations, and eventually the clustering becomes nonlinear on small scales. The dark matter collapses into relatively dense, virialized clumps: dark matter haloes. It is only within the dense environment of a halo that we expect gas to be able to cool and form galaxies. It then seems as though the problem of understanding the properties and clustering of galaxies can be split naturally into two parts in ΛCDM: understanding the distribution of the dark matter haloes themselves, and understanding the processes involving the dark matter and the baryonic components inside the haloes. This is clearly simplified if the two parts of the problem can be considered independently, and this is precisely what is done in the so-called halo model of (dark matter or galaxy) clustering (Benson et al., 2000; Seljak, 2000; Berlind & Weinberg, 2002; Cooray & Sheth, 2002; Smith et al., 2003). We elaborate on this model in Section 1.2.3.

Many tools, both theoretical and computational, have been developed to study the growth of structure and the formation of galaxies in CDM universes. In the next section we outline the key techniques we use in this thesis.

1.2 Modelling techniques

1.2.1 Dark matter simulations

As should be clear from the previous section, much of the dark matter structure we wish to study is nonlinear. Detailed analysis therefore requires the use of simulations, for example as in the pioneering work of Davis et al. (1985). For a review see, e.g., Bertschinger (1998) and references therein.

To calculate the evolution of the dark matter distribution we must solve the collisionless Boltzmann equation for the phase space density $f(\boldsymbol{r}, \boldsymbol{u}, t)$ of dark matter,

$$\frac{\mathrm{d}f}{\mathrm{d}t} \equiv \frac{\partial f}{\partial t} + \boldsymbol{u}.\nabla_r f + \boldsymbol{F}.\nabla_u f = 0 \quad , \tag{1.6}$$

where $\boldsymbol{F} \equiv -\nabla_r \Phi$ is determined from the Poisson equation for Newtonian gravity (sufficient here),

$$\nabla_r^2 \Phi = 4\pi G(\rho - \rho_0) \quad , \tag{1.7}$$

where ρ can be expressed in terms of the phase space density as

$$\rho(\boldsymbol{r}, t) = \int f(\boldsymbol{r}, \boldsymbol{u}, t)\mathrm{d}\boldsymbol{u} \quad , \tag{1.8}$$

ρ_0 is the mean density and Φ is the peculiar potential. $\boldsymbol{F}$ is then the extra, Newtonian force felt by particles due to fluctuations in the potential. Note that otherwise attempting to solve Poisson's equation with a non-zero mean density added to the right-hand side introduces extra, unphysical forces: the evolution of the scale factor due to the mean, background density is treated relativistically and separated out (see, e.g., Peebles, 1980). These are physical equations given in terms of physical distances $\boldsymbol{r}$ and velocities $\boldsymbol{u} \equiv \dot{\boldsymbol{r}}$; a cosmological code needs to be able to translate to comoving distances, $\boldsymbol{x} \equiv \boldsymbol{r}/a$, and peculiar velocities $\boldsymbol{v} \equiv \dot{\boldsymbol{r}} - H\boldsymbol{r} = a\dot{\boldsymbol{x}}$.

The equations must be discretized to be solved on a computer. One possibility is to discretize space, solving the equations on a mesh. For dark matter simulations, however, it has been found much more effective to discretize mass, sampling the dark matter distribution with particles: the N-body method. Some of the attractive numerical properties of the method are described by Springel (2005). That paper describes the code, GADGET2 (see also Springel et al., 2001b), used to run all the N-body simulations employed in this thesis, and gives a fuller description than possible here of the development of simulation codes. For our large-scale structure studies, the most salient advantage is the great dynamic range afforded by the N-body method. We wish to analyse cosmological volumes, and yet resolve the formation history of individual galaxies. Modern N-body algorithms running on current computer hardware are up to this task. We note that these methods may also be used to simulate gas and the gas physics involved in star formation (the smoothed particle hydrodynamics (SPH) technique), though mesh codes are also far more competitive in this area and have some distinct (and often complementary) advantages, such as the ability to properly resolve shocks (see, e.g., Norman & Bryan, 1999). Results from direct simulations of galaxy formation, such as those using SPH, are often compared and contrasted to results from the semi-analytic models we cover in the following section (e.g., Helly et al., 2003b).

The problem now is to solve for the dynamics of a large number of particles, each of which exerts a gravitational force on every other particle. There are a few subtleties. Cosmological simulations are usually carried out with periodic boundary conditions; that is, the simulation volume is a cube, and if a particle leaves through one face of the cube it re-enters through the opposite face. The force on a particle from particles in other periodic copies of the box must therefore be accounted for. A true particle would also have a density distribution given by a Dirac delta function. We are not, however, simulating true particles. A simulation particle may represent of order 10^{70} dark matter particles;

treating it as a delta function leads to spurious scattering effects (e.g., Aarseth, 1963), and the code can devote many small timesteps accurately evolving the orbits of two close 'particles' with steep potentials which are not, physically, particles (e.g., Efstathiou & Eastwood, 1981). The N-body particle's density distribution is therefore represented by a δ-function convolved with a softening kernel that has some characteristic length scale, limiting the effective resolution of the simulation.

Given the density distribution, $\tilde{\delta}(\boldsymbol{x})$ of a particle (labelled $\tilde{\delta}$ by analogy with the Dirac delta function, not to be confused with the overdensity field), we can then define an interaction potential for a simulation box with sides of length L as the solution of

$$\nabla_r^2 \varphi(\boldsymbol{x}) = 4\pi G \left[-\frac{1}{L^3} + \sum_{\boldsymbol{n}} \tilde{\delta}(\boldsymbol{x} - \boldsymbol{n}L) \right] \quad , \tag{1.9}$$

where we sum over all integer triples $\boldsymbol{n} = (n_1, n_2, n_3)$. The peculiar potential given by Equation 1.7 can be recovered at any point via a sum over particles, as

$$\Phi(\boldsymbol{x}) = \sum_i m_i \varphi(\boldsymbol{x} - \boldsymbol{x}_i) \quad . \tag{1.10}$$

The formidable nature of the calculation can be seen by defining canonical momenta $\boldsymbol{p}_i = a^2 m_i \dot{\boldsymbol{x}}_i$ and writing down the Hamiltonian $H(\boldsymbol{p}_1, \ldots, \boldsymbol{p}_n, \boldsymbol{x}_1, \ldots, \boldsymbol{x}_n, t)$ of the system:

$$H = \sum_i \frac{\boldsymbol{p}_i^2}{2 m_i a(t)^2} + \frac{1}{2} \sum_{i,j} \frac{m_i m_j \varphi(\boldsymbol{x}_i - \boldsymbol{x}_j)}{a(t)} \tag{1.11}$$

(the previous three equations being equations 2, 3 and 1 respectively of Springel 2005). This involves a double sum over all particles — every particle in the box feels a force from every other particle in each periodic copy of the whole box — so a straightforward method of computing the dynamics seems to scale as N^2. Indeed, this is the case in some codes designed to calculate stellar dynamics to high accuracy (Makino et al., 2003).

For a cosmological code, we can sacrifice a small amount of accuracy in return for speed. It is more important for us to know, say, the position and mass profile of a halo than to know the orbits of all the particles within it to exquisite precision. The Poisson equation can be solved using efficient Fourier methods on a mesh, for example, with particles being assigned to mesh cells, and the time for the potential calculation scaling as $\log N_{\mathrm{m}}$ where N_{m} is the number of mesh cells. There are some problems with this, mainly that the mesh has a certain size, limiting the dynamic range. An alternative approach is the 'tree' code. The forces due to very nearby particles on any given particle are accumulated individually, affording the highest possible accuracy. Particles slightly further away (on different twigs on the tree, perhaps) have their contribution to the force

aggregated together before being added to the shorter-range forces. This saves CPU cycles because the potential due to the whole twig needs to be calculated only once and is reused for each leaf on adjacent twigs. Particles even further away are aggregated hierarchically into even larger groups (branches, perhaps). Because the structure is hierarchical, it can have sufficient layers such that the largest 'branch' incorporates the whole simulation box, and yet the series of branches terminates in an individual leaf (simulation particle). Since there is no intrinsic scale imposed (other than that already set by the particle mass) this method does not further limit the dynamic range of the simulation, and can be coded to be highly efficient. GADGET2 is primarily a tree code, though a mesh can optionally be used to calculate the large-scale potential.

Many other features of the code are used to improve its speed. For example, it can be run on an arbitrary number of processors. To do so requires an intelligent way to distribute parts of the simulation between processors and to allow each CPU to communicate with the others where necessary. Processors are able to output to disk in parallel. Some particles, for example those in more clustered regions, require smaller integration timesteps than others to achieve comparable accuracy in their orbits; the particles' timestep length can therefore be assigned adaptively.

Naturally, a method to integrate the equations of motion of the particles is useless unless one can specify the initial conditions. The problem is to take a statistic such as the power spectrum, which describes the properties of a density distribution, and turn this into a distribution of particles which can be input to the N-body code. While there are various methods, and refinements to these methods (see, e.g., Sirko, 2005, and references therein) most are based on the Zel'dovich (1970) approximation, which evolves an initial density perturbation using Lagrangian perturbation theory. It is usually more efficient to push this approximation for as far as one is confident in its results before switching over to the N-body calculation, since it is quicker, but one must clearly start the N-body calculation well before the first resolved objects are expected to form.

Associated methods

It is important to develop appropriate tools to extract the most from the results of N-body simulations. We often work with the power spectrum of fluctuations, or its Fourier counterpart the correlation function $\xi(\boldsymbol{r}) \equiv \langle \delta(\boldsymbol{x})\delta(\boldsymbol{x}+\boldsymbol{r}) \rangle$. There are standard methods for calculating this for a set of points, where those points may represent either dark matter particles or galaxies. The sheer number of N-body particles in a large simulation

represents an obstacle, though in fact the dark matter correlation function and power spectrum are calculated on the fly by GADGET2. When we calculate galaxy correlation functions in this work, we will always be concerned with galaxies in a volume with simple geometry (a periodic box) and so we use a straightforward estimator of the correlation function. For each bin in distance we wish to consider — with inner radius r_1 and outer radius r_2, say — we sum the number of galaxies lying at this distance from each galaxy in the sample. We then divide by the expected number of galaxies in this bin, $4\pi\bar{n}N(r_2^3 - r_1^3)/3$ where $\bar{n}$ is the mean number density of the sample and N is the total number of galaxies in the sample, to obtain $1 + \xi$ for the bin. This estimator does not necessitate the generation of random catalogues, as do more complicated estimators used for analysing surveys which have more complex geometry and for which the true mean density is unknown (see, e.g., Landy & Szalay, 1993). In practice our code is made more efficient by, for example, ensuring we do not count each pair of galaxies twice, and by subdividing the box into cells with length not much greater than the maximum distance at which we wish to measure ξ. The latter ensures that the code only has to examine galaxies in the same cell or in cells adjacent to the galaxy under consideration to test whether the separation of the two galaxies lies in one of the radial bins being measured.

We are often concerned with the distribution and properties of dark matter haloes. The definition of a halo is usually motivated by the spherical collapse model (see, e.g., Eke et al., 1996, for the $\Omega_\mathrm{m} + \Omega_\Lambda = 1$ case) where we expect collapsed structures to have overdensities compared to the cosmological background of ~ 200. There are various ways to look for regions of this overdensity. A popular method is the friends-of-friends (FOF) algorithm (Davis et al., 1985) where a value for the overdensity is translated into an inter-particle separation for particles in regions of this density. Then, given a particle, we search through nearby particles to see if any are within this 'linking length', $bn^{-1/3}$ where n is the number density of particles. If we do find such particles, we link them to the first one and then check if they, in turn, have any sufficiently close neighours to be linked. A maximal set of particles which can be linked together in this way is identified as a halo (groups of small numbers of particles — fewer than 10, say — are rejected as possibly spurious). Another reasonable method is to look for particles which are candidate halo centres, and then find the largest sphere around them such that the enclosed mass has a density greater than the threshold overdensity. If this sphere encloses sufficiently many particles then it is identified as a halo. Cole & Lacey (1996) compare the properties of haloes found using these two methods, and their sensitivity to the thresholds discussed

above. Haloes turn out to be reasonably well defined objects (having gone nonlinear and broken away from the Hubble flow) and one finds similar objects using either method. They are in general triaxial, though, motivating treatments of collapse which do not assume spherical symmetry. We discuss halo formation in more detail in Section 1.3.1.

It is also useful to study subtructures of haloes. When we use substructure information in our simulations, it is found with the SUBFIND algorithm of Springel et al. (2001a). The general idea here is to look for saddle points in the density field, since if there are two local maxima then there must be a saddle point somewhere between them. The particles associated with a density maximum are considered to be part of a subhalo candidate centred on this maximum, and the algorithm ensures that each particle can be associated with at most one subhalo. It also checks if the particles are actually bound to the structure, using the velocity information associated with the particles. Only bound particles can be considered parts of a subhalo. The subhalo information is integral to the construction of the N-body merger trees described in Chapter 2.

1.2.2 Semi-analytic modelling

Recall that our general picture of galaxy formation in ΛCDM involves gas collecting and cooling in dark matter haloes, leading eventually to star formation (White & Rees, 1978). This picture developed into one where it was appreciated that galaxy formation is a rather more dynamic process: haloes merge and constantly accrete mass, affecting the galaxies within them and providing further fuel for star formation (Cole, 1991; Lacey & Silk, 1991; White & Frenk, 1991). This in turn led to more complete models where the hierarchical buildup of dark matter structures was integrated with the gas physics taking place in each halo (Kauffmann et al., 1993; Cole et al., 1994a). The gas physics is described by comparatively simple analytic approximations, often assuming a degree of symmetry, that can be calculated relatively fast. This allows a large space of different parameters governing the cosmology and the gas physics to be quickly traversed; being able to explore galaxy formation in many cosmologies is key to the study we undertake in Chapter 4, where we explain the features of our semi-analytic model more thoroughly. The modelling of the 'merger tree' which describes the mass aggregation history of a halo is, meanwhile, described more fully in Section 1.3.1 (its construction from an N-body simulation is described in Chapter 2). We note in passing that the merger trees and the physics in semi-analytic models can also be run to extremely high mass resolution; a great advantage compared to SPH simulations of galaxy formation.

The flexibility of having parametrized physics in which the parameters can be altered to match the results of simulations or observational constraints, or to see the effects of a certain piece of physics on the galaxy properties from the model, could be regarded as a strength of the semi-analytic approach. It is only fair to say that it can instead be viewed as a weakness; a model gives no unique prediction of the properties of the galaxy population, and sometimes very different pieces of physics can be used to achieve the same ends with a suitable choice of parameters. For this work, we are in fact more interested in whether we can reproduce the observed properties of the galaxy population — whether the model output *looks* realistic — than whether or not every piece of physics makes a contribution of precisely the correct weight to the final properties. Semi-analytic models have become steadily more sophisticated and can match several classes of observations of galaxies (Kauffmann et al., 1999; Somerville & Primack, 1999; Cole et al., 2000). We, naturally, focus on the Durham semi-analytic model, GALFORM (Cole et al., 2000), enhanced in Chapter 4 by the addition of physics described by Benson et al. (2003) (and a model designed to fit high redshift data by Baugh et al. 2005) and in Chapter 3 by the improvements described by Bower et al. (2006).

1.2.3 Halo models

We remark above that in modelling galaxy formation and galaxy clustering, it has been found helpful to separate the problem into two parts: modelling the distribution and properties of haloes, and modelling the processes that take place within haloes. This split may be quite well defined because haloes themselves are quite well defined objects, their internal dynamics being quite distinct from the dynamics of the surrounding large-scale structure. The separation of the modelling effort is known as the halo model (Benson et al. 2000; Seljak 2000; Berlind & Weinberg 2002; for a comprehensive review see Cooray & Sheth 2002). Semi-analytic galaxy formation may be considered to be a method rooted in the halo model: each halo is considered case-by-case, only being influenced by other haloes if they happen to merge onto it. With the galaxy population of each halo given, knowing the halo mass function (the space density of haloes as a function of mass) gives us quantities such as the galaxy luminosity function. If we know the distribution of haloes, for example from N-body simulations or from theory, we therefore know, up to uncertainties about where galaxies are placed within haloes, the way galaxies cluster. The halo model is not applicable only to galaxies; Smith et al. (2003) develop a highly accurate model of dark matter clustering by applying halo model principles. We, though,

do concentrate mainly on galaxies. The connection between haloes and galaxies is made a little more formal in the halo occupation distribution, described below.

The halo occupation distribution

As we remark above, the most basic prediction of a semi-analytic model is how many galaxies of a given type reside in a given dark matter halo. We may attempt to simplify this: the prediction is how many galaxies of a given type reside in a dark matter halo of given *mass*. This assumes the halo mass is the only factor which determines the probability distribution for the number of galaxies in the halo. More formally, for any given subset of galaxies (typically, for all galaxies brighter than some threshold luminosity), the model gives us $P(N|M)$, the probability that a halo of mass M contains N such galaxies. We can decompose this into two parts:

- $\langle N(M) \rangle$, the mean number of galaxies in a halo of mass M, and
- $P(N|\langle N \rangle)$, the probability distribution for the number of galaxies in any one halo given the mean number expected for that halo.

These may each be further decomposed into a term for central galaxies and a term for satellite galaxies. A halo's central galaxy is treated differently from the other galaxies in the halo in semi-analytic models: for example, it is able to feed off the halo's reservoir of hot gas, which cools onto the central galaxy (satellites may, by contrast, be stripped of their gas as they fall into a larger halo). This special treatment is motivated by the fact that, for example, clusters often contain a central galaxy the luminosity of which dominates all the surrounding galaxies, and which appears to have formed by cannibalizing smaller, infalling galaxies. More recently, Skibba et al. (2006) have shown that they can model galaxy clustering in the SDSS better if they treat central galaxies specially.

$P(N|M)$ is one component of the halo occupation distribution, or HOD (Berlind & Weinberg, 2002; Berlind et al., 2003). The other component specifies how the galaxies are distributed (in relation to the dark matter) within a halo. Berlind & Weinberg (2002) parametrize this as a shift in the logarithmic slope of the density profile of galaxies compared to the dark matter, and a scaling of the velocity dispersion of the satellite galaxies compared to the dark matter (the central galaxy being assumed to lie at the centre of the halo with zero velocity offset). In any case, once these two components are specified in any given cosmology, they provide a complete description of the clustering of galaxies, subject to the restriction alluded to above: we assume that knowing the mass

of a halo is enough to completely specify the probability distribution for the number and location of its galaxies. If this assumption is incorrect, it throws the validity of this formalism (or of any straightforward analytic implementation of the halo model) into doubt. The question of whether or not this assumption is accurate, and what steps can be taken to rectify our models if it is not, occupies our attention for the bulk of Chapters 2 and 3.

A fuller discussion of how galaxy clustering statistics are related to these halo occupation numbers and may be derived from them is given by, for example, Zheng (2004) or Tinker et al. (2005). The correlation function is decomposed into two terms, one coming from pairs of galaxies in the same halo (the one-halo term) and the other coming from pairs of galaxies in different haloes (the two-halo term). While the two-halo term scales as the number of galaxies per halo, then, and is more important at large separations, the one-halo term scales as the number of galaxy pairs per halo and is more important at small separations.

The HOD approach has been used to study the abundance of substructures in dissipationless simulations (Kravtsov et al., 2004). It has been used to try to improve the constraints that galaxy clustering statistics provide on cosmological parameters by Abazajian et al. (2005), who simultaneously obtain an observational constraint on the HOD that may provide an interesting test for galaxy formation models. Zheng et al. (2005) explore some more sophisticated parametrizations of the HOD, focusing on the split between central and satellite galaxies. A consistent outcome of this work seems to be that well-fitting HODs have the following features:

- $\langle N_{\rm cen}(M)\rangle$, the mean number of central galaxies in a halo of mass M, is close to being a step function going from 0 to 1 at some mass $M_{\rm min}$ (note that $0 \leq \langle N_{\rm cen}(M)\rangle \leq 1$ by construction).

- $P(N_{\rm cen}|\langle N_{\rm cen}\rangle)$, follows a 'nearest integer' distribution: if $0 < \langle N_{\rm cen}(M)\rangle < 1$ then $P(N_{\rm cen} = 1) = \langle N_{\rm cen}\rangle$ and $P(N_{\rm cen} = 0) = 1 - \langle N_{\rm cen}\rangle$.

- $\langle N_{\rm sat}(M)\rangle$ is close to a power-law, with high mass slope close to 1, and possibly with a cutoff (sharp or smooth) near $M_{\rm min}$.

- $P(N_{\rm sat}|\langle N_{\rm sat}\rangle)$ is close to a Poisson distribution with mean $\langle N_{\rm sat}\rangle$.

This is also borne out by our semi-analytic results, as we shall see.

1.3 Halo formation and environment

1.3.1 Press-Schechter theory and its extensions

Consider an overdense region in the initial density field. Assuming it is uniform and spherical, it can be treated as a mini-universe subject to the Friedmann equation in its own right. If it is above the critical density it can, therefore, recollapse. The time at which it starts to recollapse (or, on the other hand, the density threshold above which a perturbation must lie to have collapsed by the present day), and other aspects of the evolution of the perturbation, have been given by, for example, Weinberg (1972) and Gunn & Gott (1972). Spherical accretion may also add to its mass. The perturbation does not collapse to a point; it undergoes violent relaxation (Lynden-Bell, 1967), reaching an equilibrium with potential energy twice the kinetic energy. Press & Schechter (1974) incorporated these results into a model of halo formation by 'self-similar condensation'. In this picture, small objects form by spherical collapse, then combine and grow into larger objects, their numbers being replenished by the growth of still smaller objects. Their model allowed them to predict a halo mass function that has been confirmed by simulations to be reasonably accurate for a fair range in halo mass. It was not without problems, however. Half the mass in bound objects was accounted for by noting that half the Universe's mass starts out in underdense regions and that this mass can accrete onto haloes. Some consider this has an element of 'fudge'. It also fails to deal satisfactorily with the cloud-in-cloud problem (Bardeen et al., 1986); that is, the problem of whether to assign a particle to an object corresponding to a small region of high overdensity, or to an object corresponding to a larger region of lower density encompassing the first.

Bower (1991) extended this theory by deriving conditional multiplicity functions; that is, the mass function of the progenitors of a halo of given mass at some earlier epoch. Bond et al. (1991, hereafter BCEK) developed the rather elegant excursion set formalism for the growth of structures, solving the cloud-in-cloud problem and also allowing the calculation of conditional mass functions and halo merger rates (Lacey & Cole, 1993). In the excursion set model, we consider the density at each point in a smoothed density field as the smoothing scale is changed (in fact, we consider the initial density field extrapolated to the present by linear theory). The smoothing scale is normally expressed in terms of the mass enclosed in the smoothing window for a region at the mean density. That is, at each point we have a function $\delta(M)$ describing how the overdensity changes as a function of mass scale. Often, the variance in the density of the enclosed region (denoted Λ by

BCEK) is used as an alternative mass variable. This is possible because as we consider larger and larger regions of the Universe, the density variance between different such regions will grow smaller and smaller, approaching zero for very large regions (since the Universe is homogeneous on large scales).

BCEK showed that $\delta(\Lambda)$ for any given point in the density field takes the form of a Brownian random walk (starting at zero for $\Lambda = 0$), so long as the filter with which the density field is smoothed is a spherical top hat in k-space. In other words, the change in smoothed density as we step from $\delta(\Lambda)$ to $\delta(\Lambda + \Delta\Lambda)$ is independent of any previous steps and of the current value of $\delta(\Lambda)$ — a Markov process. This is convenient because Chandrasekhar (1943) derived the rate at which these Brownian trajectories first cross above a given threshold value, δ_c.

Consider a point in the density field at $z = 0$. The spherical collapse model tells us that if it lies in a region with overdensity greater than some threshold — or, rather, a region that would have an overdensity greater than this threshold if the density field grew by linear theory up to $z = 0$ — then it in fact lies in a region that has turned around and collapsed into a nonlinear object (a halo) by the present day. This threshold is given by $\delta_c = 1.686$ for an $\Omega_m = 1$ universe, for example. In the excursion set model, the value of Λ for which the Brownian random walk makes its first upcrossing of this threshold tells us the mass of the halo (if any) in which a particle starting at this point lies at $z = 0$.

The same procedure works at higher redshift, but of course the density threshold is correspondingly higher, given by $\delta_c(z = 0)/D(z)$ (denser regions collapse earlier). The Press-Schechter mass function takes on a universal form when expressed in terms of $\delta_c(z)$ and $\sigma^2(M, z)$, the variance of the linear density field at mass scale M extrapolated to the redshift z at which the haloes are identified. We first define a function $f(\sigma, z)$ by

$$f(\sigma, z) \equiv \frac{M}{\rho_0} \frac{\mathrm{d}n(M, z)}{\mathrm{d}\ln \sigma^{-1}} \quad , \tag{1.12}$$

where $n(M, z)$ is the number density of haloes with mass less than M at redshift z and $\rho_0(z)$ is the mean density of the Universe. Then we have

$$f(\sigma) = \sqrt{\frac{2}{\pi}} \frac{\delta_c}{\sigma} \exp\left(-\frac{\delta_c^2}{2\sigma^2}\right) \quad . \tag{1.13}$$

The mass function therefore takes the form of the Schechter (1976) function popularly used to model the galaxy luminosity function and has the property that all the mass in the Universe is in bound objects of some mass, both of which facts may account for the acceptance of the original fudged argument of Press & Schechter (1974).

The power of the excursion set model is seen by the fact that once a point's trajectory $\delta(\Lambda)$ upcrosses a threshold, it continues its Brownian random walk; the fact it is starting from a new, higher position makes no difference. Therefore the same machinery can be used to find the probability that it later upcrosses a higher threshold: we can find the probability that a point in a halo of mass M_1 at redshift z_1 lies in a halo of mass $M_2 < M_1$ at redshift $z_2 > z_1$. That is, the calculation of conditional mass functions and halo merger rates is dealt with quite naturally by this formalism. The Monte Carlo merger trees used in the GALFORM models in Chapter 4 are constructed by a method based on this formalism (in fact, on extensions to it by Lacey & Cole 1993 who also focus on the distribution of halo formation times). This method is explained by Cole et al. (2000); see, e.g., Sheth & Lemson (1999) or Somerville & Kolatt (1999) for alternative approaches.

We see the flexibility of this approach by noting it has been used to model sheets and filaments (Shen et al., 2006), and even voids (Sheth & van de Weygaert, 2004; Furlanetto & Piran, 2006). It can be used to study how the mass function changes with local density (e.g., Sheth & Tormen, 2002, and references therein). There have been attempts to extend it to non-Markov processes, i.e. to more general smoothing filters (Amosov & Schuecker, 2004) and, perhaps most successfully, to apply the technique to more general models of collapse than the usual spherical model. Sheth et al. (2001) employ the ellipsoidal collapse model and derive halo mass functions which agree much better than the Press-Schechter mass function with those derived from N-body simulations (e.g., Jenkins et al., 2001). Both Sheth et al. (2001) and Jenkins et al. (2001) still express their mass functions in a universal form, modifying $f(\sigma)$ but retaining its definition through Equation 1.12. In ellipsoidal collapse, however, the overdensity threshold for collapse is a function of mass — the so-called 'moving barrier' — complicating the analysis so that there is not at present a satisfactory method of deriving merger trees in the ellipsoidal collapse model, despite further theoretical work on moving barriers in excursion set theory (Del Popolo, 2006; Zhang & Hui, 2006).

The approach is not without some niggling problems. For example, Benson et al. (2005) point out the algorithm for generating merger trees is not entirely consistent (though this is not necessarily a problem with the underlying extended Press-Schechter theory): if we ask the merger rate between haloes of two different masses, the answer depends upon whether we consider the smaller halo to have merged onto the larger one, or vice versa. In a self-consistent model, applying the merger algorithm to haloes satisfying the Press-Schechter mass function at redshift z should result in a halo population still

satisfying the appropriate Press-Schechter mass function at redshift $z + \Delta z$, and this is not the case, though Benson et al. (2005) have shown how to achieve this by inverting the Smoluchowski (1916) coagulation equation for power-law power spectra. In this thesis, we also show that some of the predictions of the formalism itself appear not to be correct when tested against N-body simulations. One area where it falls down is in its treatment of the environmental dependence of halo properties, which we introduce below.

1.3.2 Environmental dependence

Recall that in our semi-analytic models, the evolution of galaxies in haloes is driven by the merger histories of those haloes. We expect to be able to treat haloes independently of the large-scale structure if their merger histories are independent of the large scale environment, as assumed by HOD models. This assumption is supported by extended Press-Schechter theory: it predicts that the distribution of halo formation times is a function of halo mass but not of halo environment. Our Monte Carlo merger trees therefore also have this property by construction. To reach this conclusion in Press-Schechter theory, however, three simplifying assumptions are made, which if relaxed may result in an environmental dependence. Firstly, only the sharp k-space filter allows the trajectories $\delta(M)$ in overdensity versus mass scale to be Brownian random walks. For more natural top hat or Gaussian filters the trajectories exhibit correlations between different mass scales, which induce correlations between environment and small-scale behaviour. Secondly, the theory deals only with individual mass points in the density field. When it predicts that a mass point is part of a halo of mass M there is no constraint that the whole of a neighbouring volume of mass M is also assigned to the same halo. The accuracy to which this assumption holds may depend on environment. Thirdly, in determining when a region collapses to form a halo, a global collapse threshold given by the spherical collapse model is assumed. If tidal fields modify this threshold, as argued by Sheth et al. (2001) in their ellipsoidal collapse model mentioned above, then these fields could also depend on environment.

Thus there is no compelling reason to believe that the lack of environmental dependence predicted by the Press-Schechter theory should carry over to a full treatment which relaxes these assumptions. It has been supported by N-body calculations, however, e.g. by Lemson & Kauffmann (1999) who used the GIF simulations (Jenkins et al., 1998; Kauffmann et al., 1999). Provided such simulations have sufficiently many outputs at different times, merger trees can be extracted and their environmental dependence stud-

ied. This approach has been limited by the dynamic range of the simulations. Either galaxy-sized haloes have not been well resolved, leaving their merger histories uncertain, or the volume has not been cosmologically representative.

Galaxy properties, however, do depend on environment. Galaxies in denser regions tend, for example, to be more bulge-dominated and to have older stellar populations (e.g., Dressler, 1980; Postman & Geller, 1984; Gómez et al., 2003; Balogh et al., 2004). In models in which the merger histories of haloes are only a function of halo mass, and in the absence of non-local gas processes (e.g. ionization by QSOs), this can only be accounted for by the variation of the halo mass function with environment, or, in other words, by the fact that high mass haloes are more clustered than low mass haloes (Kaiser, 1984; Cole & Kaiser, 1989; Mo & White, 1996; Mo et al., 1999; Sheth & Lemson, 1999; Abbas & Sheth, 2005). Models which attempt to reproduce environmental dependence can then do so only by populating more massive haloes with a greater fraction of 'early-type' galaxies. This method has been recently supported by the observational results of Blanton et al. (2006).

None the less, Sheth & Tormen (2004b) argue that one of the results of Lemson & Kauffmann (1999) suggests, rather indirectly, an environmental dependence of halo formation times and, therefore of halo merger trees. We revisit this argument in Section 2.3, noting that it also predicts the sign of the dependence, and predicts it correctly in the light of our results. The range of assumptions required for analytic theory to predict environmental independence also suggests that detection of some signal should be possible. To make progress on this matter using N-body simulations seems, then, to require one of two things. Firstly, we may try to pin down the environmental dependence of halo formation times suggested by the above results by using more sensitive tests. Sheth & Tormen (2004b) claimed to have found such a test — the marked correlation function — and found a signal of environmental dependence despite using the same GIF simulations as Lemson & Kauffmann (1999). Marked statistics (Peebles, 1980; Boerner et al., 1989; Stoyan & Stoyan, 1994) have recently proved useful in the analysis of both simulations (Faltenbacher et al., 2002; Gottlöber et al., 2002; Sheth et al., 2005) and surveys (Beisbart & Kerscher, 2000; Szapudi et al., 2000; Skibba et al., 2006), offering both sensitivity and information complementary to that provided by other statistics. A more general discussion of marked statistics and their interpretation is given by Sheth (2005). Secondly, we may use larger simulations, so that even a subset of the haloes spanning a small range in mass provides adequate statistical power to see significant evidence of environmental

dependence, if this dependence exists and is sufficiently large to be interesting. Higher resolution would also allow us to study haloes which host only a single bright galaxy, so that we may hope for a more direct link between the halo properties and the galaxy properties than one would expect when studying more massive haloes. An environmental dependence of the merger histories of galaxy-sized haloes may provide a more direct explanation for the variation in galaxy properties with environment, and would suggest that the systematic change in the halo mass function with environment is not the only driving force behind the systematic change in galaxy properties with environment.

In Chapter 2 we attempt to combine both the above techniques. That is, we calculate the marked correlation function as suggested by Sheth & Tormen (2004b), and later go on to discuss some other statistics closely related to the marked correlation function. We apply these calculations to the "Millennium Simulation" (Springel et al., 2005), which resolves the merger histories of haloes small enough that we expect them to host a single galaxy of luminosity $0.1L_*$ (where L_* is the characteristic luminosity corresponding to the break in the galaxy luminosity function), but that probes a cosmologically representative volume. This is the simulation used by Gao et al. (2005) to study the age-dependence of halo clustering, using an approach which is complementary to that taken here. Other simulations have recently been used to study the environmental dependence of halo properties by, e.g., Avila-Reese et al. (2005); Maulbetsch et al. (2006) and Reed et al. (2006). The latter paper, in particular, complements our results by aggregating together galaxy-sized haloes and galaxy-sized subhaloes, and considering the environmental dependence of their formation times (or, rather, the age-dependence of their clustering), which perhaps correspond more closely to galaxy properties.

It is clearly of interest to know how these environmentally dependent halo properties translate into galaxy properties, and therefore how they affect galaxy clustering statistics. Croton et al. (2006a) approach the problem in a similar way to us, studying how 'halo assembly bias' affects the clustering of their semi-analytic galaxies, using the semi-analytic model of Croton et al. (2006b). Cooray (2006) suggests that an approach to clustering based on a generalization of the conditional luminosity function (the space density of galaxies as a function of halo mass *and* luminosity; see Yang et al. 2003) to other conditional functions deals with these issues more flexibly and could be used to construct an analytic model of galaxy clustering given this age dependence. Meanwhile, Yang et al. (2006) have tried to find observational evidence of an age dependence of halo bias by studying the star formation rate of galaxies in groups of a given, measured mass

in the 2dFGRS. This is perhaps related to the discovery by Weinmann et al. (2006) of 'galactic conformity' in the SDSS: the type of satellite galaxies found in a halo of given mass depends on the type of central galaxy found in the halo. Tinker et al. (2006a) pay particular attention to modelling the void probability function (VPF) of SDSS galaxies, using a modified HOD formalism incorporating environmental dependence. Since we are particularly interested in constraining cosmology using catalogues generated by a combination of N-body simulations and semi-analytic models, we aim in Chapter 3 to test directly the effect of assembly bias in our models. Our shuffling procedure is different to that used by Croton et al. (2006a) and we use the semi-analytic model of Bower et al. (2006). Given that we will later use simulations in which we must run the semi-analytics using Monte Carlo trees, we focus on what sort of corrections may need to be applied to the HODs from the Monte Carlo approach (or, perhaps, what sort of corrections could be made directly to the clustering results) for them to reproduce the results given by trees which automatically incorporate environmental effects. Following Tinker et al. (2006a), we also consider whether the VPF provides any additional information or can be modelled better using an environmentally dependent HOD. It seems plausible that the VPF could provide interesting and unique constraints, not least because a remarkable result due to White (1979) expresses the VPF in terms of N-point correlation functions, with N running from 1 to infinity.

1.4 Constraining cosmological parameters

We have already discussed some of the observations which have been used to establish the ΛCDM model. Often, these same observations can be used to constrain the parameters of the model, sometimes to high precision. A rather comprehensive list of the parameters we might wish to measure is given by, for example, Tegmark et al. (2006). To test whether or not a model with given parameters is a good fit to the data, we need to be able to generate synthetic datasets, or, in other words, to generate robust theoretical predictions.

For a given ΛCDM cosmology, we can predict very accurately the clustering statistics of the dark matter, since these are well modelled by N-body simulations, or, for that matter, by analytic models calibrated to simulations (Smith et al., 2003). We do not usually observe the clustering of dark matter directly, though weak lensing shear-shear correlations can provide (at present noisy) estimates. Redshift surveys may furnish us with galaxy clustering statistics, while weak lensing measurements, for example, normally

probe the cross-correlation between galaxies and dark matter.

As we mention above, galaxy clustering statistics derive a great deal of their power to constrain cosmological parameters by constraining the scale at which the power spectrum 'turns over' on large scales, which complements the high-redshift CMB constraint on this scale rather well. The baryonic features in the correlation function or power spectrum add to the effectiveness of the constraint (Cole et al., 2005; Eisenstein et al., 2005). The scales used in these joint constraints tend to be large scales, where the evolution of clustering is still in the linear regime or where deviations from linearity can be more readily modelled. Moreover, in this regime the galaxy correlation function is expected, in the absence of non-local effects, to have the same shape as the mass correlation function, though offset by a constant factor (see, e.g., Coles, 1993). That is, we may define a bias factor, b, linking the galaxy and mass autocorrelation functions,

$$\xi_{\rm gg} = b^2 \xi_{\rm mm} \tag{1.14}$$

This bias factor depends on the galaxy population under consideration; it depends, for example, on the threshold luminosity of the sample. Because of this uncertainty, when the galaxy correlation function is used to constrain cosmology, information on its overall normalization is not normally used, and the constraints come entirely from its shape.

In Chapter 4 we generate synthetic galaxy clustering statistics by painting galaxies from a semi-analytic model onto dark matter distributions given by N-body simulations. We can see the possibility for two benefits. Firstly, because we attempt to generate realistic catalogues with full galaxy properties, we can make a *prediction* for the bias factor of a given galaxy sample and hence use the overall normalization of the correlation function in our cosmological constraints. In particular, we may be able to constrain σ_8, the overall normalization factor for the dark matter power spectrum, which is not possible for normal techniques employing galaxy clustering. Secondly, because we populate the simulation on a halo-by-halo basis rather than just assuming that galaxies approximately trace mass on large scales, we generate a theoretical prediction for the small-scale, nonlinear clustering. We can therefore attempt to use this information in our cosmological constraints too.

Our constraints are largely independent from CMB constraints, and involve different assumptions (though in general we consider only flat models, which one could consider is implicitly using CMB results). Because dark energy has an effect on structure formation, and different forms of dark energy might affect it in different ways at late times, it is useful to have an independent, low-redshift constraint on σ_8 that does not rely on a joint

analysis with high-redshift data (Bartelmann et al., 2006). A joint analysis would tend to be more model-dependent as one must be able to model what happens in the gap between observed snapshots of the Universe.

1.5 Structure of this thesis

In Chapter 2 we describe work on the environmental dependence of halo formation times. In Section 2.1 we describe the Millennium Simulation, and the merger trees used to calculate the formation times used in this work. This simulation and its data products are used throughout Chapters 2 and 3. We describe the marked correlation function in Section 2.2. We also discuss here the choice of mark used for the majority of our marked correlation function results. Then in Section 2.3 we go on to describe our results, including tests to justify our choice of mark. These motivate the definition of a marked cross-correlation function, which we calculate for various halo samples. We also present results of a test of the effect of environment on halo formation which corresponds more directly to earlier calculations using smaller simulations.

We go further in Chapter 3, employing a shuffling algorithm, detailed in Section 3.1.2, to study the effect of these environmental dependencies on galaxy clustering statistics, in particular the correlation function (Section 3.2.1) and the void probability function (Section 3.2.2), in a semi-analytic model. These can be understood in terms of the effect of changes in local density on the HOD, studied in Section 3.2.3. In Section 3.2.4 we discuss ways to model the environmental effects and to overcome problems caused by the fact that halo occupation depends on environment as well as halo mass.

Some aspects of the semi-analytic model are discussed in Section 3.1.1, but in Chapter 4 we go into slightly more detail, and explain the three GALFORM variants used in this chapter in Section 4.1.1. These are the models with which we attempt to constrain cosmological parameters using a combination of N-body simulations, semi-analytics, and the observed two-point correlation function from the SDSS, bearing in mind the results of the previous two chapters. Our simulations are described in Section 4.1.2. Each simulation is used to represent several different cosmologies, by employing a relabelling and rescaling technique based in part on the work of Zheng et al. (2002). This technique is described in more detail in Appendix A. We also comment on the usefulness of clustering statistics in inverting the approach described above, i.e. taking the cosmology as known and considering what constraints may be applied to models of galaxy formation given our

knowledge of galaxy clustering. Finally, we present some conclusions in Chapter 5.

Chapter 2

Environmental dependence of halo formation times

2.1 The Millennium Simulation

For our work on the environmental dependence of halo formation times we use the Millennium Simulation (Springel et al., 2005) carried out by the Virgo Consortium using a modified version of the TREE-PM N-body code GADGET2 (Springel et al., 2001b; Springel, 2005). The cosmology is a flat, ΛCDM model, with $\Omega_{\rm m} = 0.25$ (so $\Omega_\Lambda = 0.75$) and $h = 0.73$. The initial power spectrum was calculated using CMBFAST (Seljak & Zaldarriaga, 1996), and is such that the primordial power spectrum has power-law index $n = 1$, the *rms* linear mass fluctuation in spheres of radius 8 h^{-1} Mpc extrapolated to $z = 0$ is $\sigma_8 = 0.9$, and the baryon density is $\Omega_{\rm b} = 0.045$. This leaves a dark matter density, $\Omega_{\rm dm} = 0.205$. The simulation follows the evolution under gravity of 2160^3 dark matter particles in a periodic box with sides of comoving length 500 h^{-1} Mpc from $z = 127$ to the present day. Each particle has mass $8.61 \times 10^8\ h^{-1}\ {\rm M}_\odot$, and the gravitational force is softened (see Section 1.2.1) with the SPH spline kernel of Monaghan & Lattanzio (1985) such that the gravitational potential at the position of an isolated particle in a non-periodic box is the same as that of a Plummer (1911) sphere of comoving size 5 h^{-1} kpc. The particle data were output and stored at 64 times, 60 of which are spaced regularly in the logarithm of the expansion factor between $z = 20$ and $z = 0$, allowing the construction of trees detailing how each dark matter halo at $z = 0$ was built up through mergers and accretion.

2.1.1 Merger trees

At each of the output times of the simulation we have a catalogue of friends-of-friends (FOF) groups (Davis et al., 1985) calculated using a linking length of $b = 0.2$ times the mean inter-particle separation. Locally overdense, self-bound substructures of these groups are found using the SUBFIND algorithm (Springel et al., 2001a). Each friends-of-friends halo is therefore decomposed into a collection of subhaloes, plus a fuzz of unbound particles. Of the subhaloes, one is typically much larger than the others and contains most of the mass of the halo. This can be thought of as the background mass distribution of the halo, while the smaller subhaloes are substructures.

Sometimes, however, the friends-of-friends algorithm links together structures which one might prefer to consider as separate haloes for the purpose of constructing the merger trees. Visually, these haloes often appear to consist of two distinct structures joined by a tenuous bridge of particles. They may also be only temporarily joined, in the sense that following the evolution of the system would see the structures move apart and become distinct friends-of-friends haloes again. Having run SUBFIND, we identify these spuriously linked haloes as follows. We split a subgroup from its friends-of-friends halo before calculating the merger trees if either of the following conditions is satisfied: the centre of the subhalo is outside twice the half-mass radius of the main halo; or the subhalo has retained more than 75 per cent of the mass it had at the last output time at which it was an independent halo. The latter condition is imposed because we expect a less massive halo to be stripped of its outer layers as it merges with a more massive halo, while if it has been artificially linked by the friends-of-friends algorithm it will have retained most of its mass. Treating the subgroups which have been split off as separate haloes has also been found to lead to a better match between galaxy properties in SPH simulations and in semi-analytic models which use the resulting merger trees (Helly et al., 2003b).

The splitting algorithm above results in a halo catalogue containing more haloes than in the original friends-of-friends catalogue. We refer to a member of this new, larger catalogue as a 'merger tree halo' below. A merger tree halo, as before, is a collection of SUBFIND subhaloes including one background subhalo. Each halo in the catalogue at the final time has its own merger tree built from these catalogues. It has become conventional in studying the properties of the merger trees themselves, however, to calculate one merger tree per friends-of-friends halo, i.e. to define a halo as a friends-of-friends object. To

provide contact with earlier work, therefore, if the splitting algorithm above results in a friends-of-friends halo being associated with two or more merger tree haloes at the final time, we consider only the merger tree of the most massive component, and discard the other trees from the same halo in our analysis. The merger tree of this remaining component is unaffected by discarding the less massive components, since each subhalo at each redshift may appear in only one merger tree (in other words, if a halo or subhalo at some time has a descendant at a later time, as almost all haloes do, then this descendant is unique). Approximately 15 per cent of friends-of-friends haloes are split in this way, and usually the mass of the discarded part is only a small fraction of the mass of the halo. The proportion of split haloes decreases with increasing halo mass, dropping to only a few per cent for haloes with mass close to the characteristic mass, $M_* = 6.21 \times 10^{12}\ h^{-1}\ \mathrm{M}_\odot$. Fig. 2.1 shows schematically a situation we have in mind, where despite the fact that we may consider two FOF haloes to have merged to become one halo, we may still regard them as separate haloes in the merger trees. This ambiguity in whether or not something has merged is not really a problem since by choosing a definition of a halo we remove the ambiguity. It is, however, a genuine choice which affects our results.

The merger trees are constructed from the group catalogues by following subhaloes from early times to late times, identifying in which halo a subhalo resides at the later time (Helly et al., in prep.). This means that given a subhalo in one snapshot, we must be able to find the corresponding object (the descendant subhalo) in a later snapshot. This is usually the next snapshot, though we check for a descendant in the next five outputs since occasionally friends-of-friends or SUBFIND is unable to identify the subhalo in the intervening snapshots. This may happen when, for example, a halo loses particles and drops below the resolution limit, or passes through a dense region in which it is not identified as a distinct object. The identity of the descendant is usually clear and unambiguous, but the formal procedure which clears up the rare problem cases is that the descendant of a subhalo is found by following the most bound 10 per cent of its mass or the 10 most bound particles, whichever is the greater mass. The descendant is the subhalo which contains the largest number of these particles. Conversely, given a parent halo in the final snapshot, we call all haloes in earlier snapshots whose descendants are within the halo its progenitors. We identify the descendant of an entire halo as being the halo which contains the descendant of its most massive subhalo. Haloes therefore do not split: a halo at redshift z_1 has at most one descendant at redshift $z_2 < z_1$. If the particles of a halo do become distributed between two haloes at a later time, only one of these two

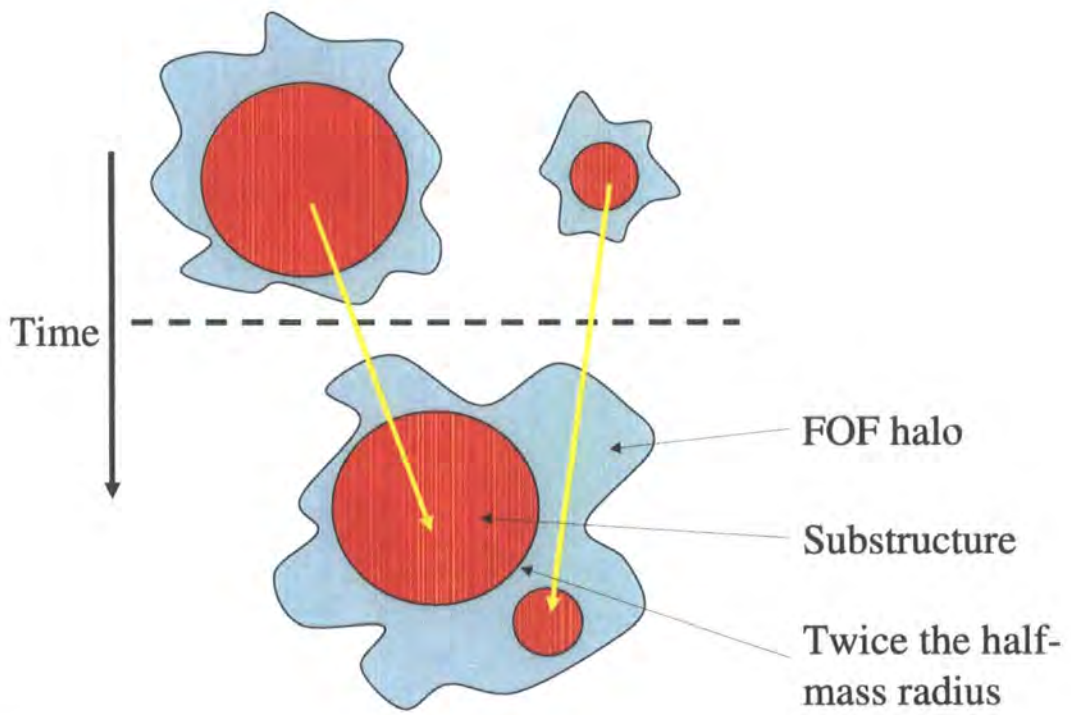

Figure 2.1: A schematic representation of a merger of friends-of-friends haloes which would not be considered a merger between 'merger tree haloes'. The blue, irregular shapes represent friends-of-friends haloes, while the red circles represent twice the half-mass radius of the main substructure of these haloes. When the top two FOF haloes merge into one halo in the lower half of the diagram, the main substructure of the smaller halo still lies outside twice the half-mass radius of the main substructure of the larger halo. The two structures are not therefore considered to have merged in our scheme. If the situation in the lower half of the diagram is present at the final time, we do however ignore the less massive of the two 'merger tree haloes' in this FOF halo in our analysis, so that we analyse precisely one merger tree for each FOF halo.

haloes may have the original halo as a progenitor. De-merger events may therefore lead to 'orphan' haloes with no progenitors. This physical splitting or de-merger of haloes as the simulation evolves is unrelated to the algorithm we use to split friends-of-friends haloes above. Clearly, though, our definition of a halo affects whether or not we consider two haloes to have de-merged, and we comment briefly below on the impact of de-mergers on our results.

Consider again a parent halo in the final snapshot. At each of the earlier snapshots, one of the progenitor haloes is designated the 'main' progenitor of the parent halo. This main progenitor is defined recursively as we move up in redshift one snapshot at a time as the most massive progenitor of the main progenitor in the previous snapshot. We then define the formation time of a halo as the redshift at which the main progenitor had half the mass of the final halo, linearly interpolating between the two redshifts at which its mass was greater than and less than half the final mass. This definition of formation redshift – the redshift at which the mass of the main progenitor falls below half the mass of the final halo – provides contact with analytic approaches to this problem and with earlier work on the formation time of N-body haloes (Lacey & Cole, 1993, 1994; Sheth & Tormen, 2004a,b).

With these definitions in place, consider Fig. 2.2, which illustrates three different situations which might be considered de-mergers, and demonstrates why de-mergers cause a problem in the definition of our trees. Note that whether we construct trees using our merger tree haloes or the original friends-of-friends haloes, the demergers we now consider are quite rare, and when they do occur they are often transients. In Case 1 in Fig. 2.2, a FOF halo splits in two. Since we considered it to consist of two merger tree haloes before the split, however, this is not a demerger in our trees and causes no significant problem. In Case 2, not only does the FOF halo split but the associated merger tree halo also splits, since what was once considered a substructure of the halo moves outside twice the half-mass radius of its parent halo and is deemed a separate object. This orphan halo has no identified progenitor (since the parent halo in the previous timestep must have a unique descendant, which turns out to be the larger of the two de-merged haloes). Therefore it will be deemed to have formed between the two timesteps, or in other words it will be assigned an artificially low formation redshift. Springel et al. (2005) follow the history of this object differently, tracing its mass since before it became a substructure of a larger halo and hence assigning it a higher formation redshift. This may introduce problems of its own in terms of the way its gas content is treated by the semi-analytic

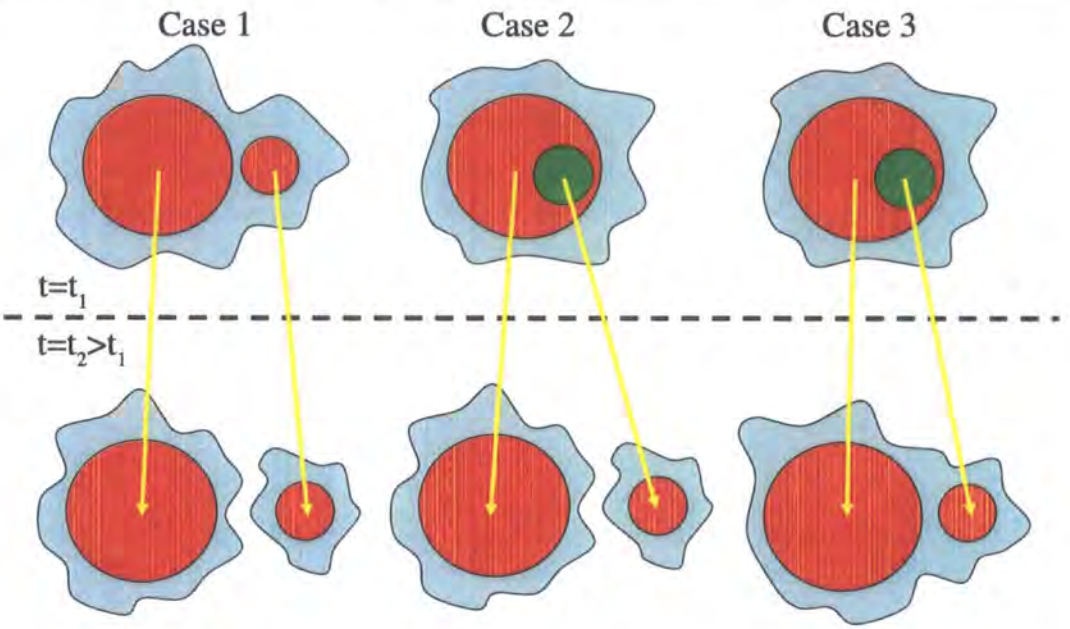

Figure 2.2: Three situations which might be considered halo de-mergers. As in Fig. 2.1, friends-of-friends haloes are shown as irregular blue shapes, and the main substructure of a halo in the earlier timestep is shown as a red circle. We also show genuine substructures (which are within twice the half-mass radius of the main substructure) of these haloes in green. In Case 1, we start with one FOF halo but two merger tree haloes, and end up with two FOF haloes each containing one merger tree halo. In Case 2 we have one FOF halo containing one merger tree halo, and end up with two FOF haloes each containing one merger tree halo. In Case 3 we again have one FOF halo containing one merger tree halo, and end up with one FOF halo that contains two merger tree haloes. Each type of de-merger presents different problems, discussed in the text.

model or how the halo properties change as it passes through a larger halo, but we do not discuss them in detail here. Instead we observe that this situation is rare (though the frequency of occurrence may be a function of local environment and hence bias our results in principle) and that we have checked that trying to weed out such awkward cases does not impact our conclusions. If such a split occurs before the final output and the substructure later merges back on to its old halo, the substructure is deemed to have been incorporated into the tree for all the intervening timesteps. If it merges on to a different halo then there is indeed a problem in precisely defining our trees since one structure cannot appear in two trees. This does not cause a problem in defining the formation redshift of an object in the final output, however. Finally, in Case 3 of Fig. 2.2, a merger tree halo splits without its parent FOF halo splitting. If this occurs in the final output we

eliminate the less massive tree from our analysis and so it does not present a significant problem. If it occurs in an earlier timestep, the haloes usually re-merge later and hence, again, do not cause a problem since the substructure can be incorporated into the tree for the intervening timesteps. The only way the haloes cannot remerge is if the situation persists until the final output (again, no problem) or if the split turns into the rarer Case 2 de-merger, which we have already discussed.

To calculate a marked correlation function of haloes we need to know the distance between any two haloes. We define this as the distance between their centres, and take the centre to be the position of the particle with the minimum gravitational potential energy, which is output by SUBFIND.

Finally, note that the trees used in this work were constructed by John Helly independently of the Millennium Simulation merger trees discussed by Springel et al. (2005) and Gao et al. (2005). The two sets of trees differ both in the criteria for identifying independent haloes and in the treatment and identification of the descendant haloes themselves. In this respect, and in respect of the methods we use to analyse our halo catalogues, the work in this chapter complements the study of the environmental dependence of halo formation by Gao et al. (2005). A discussion of the issues involved in constructing suitable merger trees (especially in the context of semi-analytic models of galaxy formation) may be found in Helly et al. (2003a).

2.2 The marked correlation function

Studying the dependence of halo formation time on halo environment requires, of course, a definition of halo environment. When using a dark matter simulation, a natural definition is the local overdensity in dark matter, measured on some chosen scale. This immediately highlights the problem of choosing an appropriate scale. It is not clear, for example, whether the choice of scale should depend on the mass of the halo under consideration. Then there are subsidiary choices such as whether to excise the region containing most of the mass of the halo from the region used to define the local overdensity.

Lemson & Kauffmann (1999) studied halo formation time as a function of the overdensity of dark matter in a spherical shell of inner radius 2 h^{-1} Mpc and outer radius 5 h^{-1} Mpc centred on the halo. There was no significant detection of a dependence of formation time on environment defined in this way. Sheth & Tormen (2004b), however, proposed a test which they considered more sensitive, and which does not require a similar

choice of scale. Their 'marked correlation function' is defined as follows.

Consider a set of N objects, taken in this case to be dark matter haloes. To each one assign a 'mark' $\{m_i\ ,\ i = 1, \ldots, N\}$, where in this study we take the mark to be formation redshift, or some proxy for formation redshift. Let the pair $\{i, j\}$ have separation r_{ij}. Then the marked correlation function $\xi_{\rm marked}(r)$, a function of separation r, is defined by

$$\xi_{\rm marked}(r) = \sum_{\{i,j \mid r_{ij}=r\}} \frac{m_i m_j}{n(r)\bar{m}^2} \quad , \tag{2.1}$$

where $n(r)$ is the number of pairs of objects with separation $r_{ij} = r$ and where the mean mark $\bar{m}$ is calculated over all objects (of all separations) in the sample.

In other words, if $\xi_{\rm marked}(r) > 1$ for some r then this implies that pairs of objects with separation r have a greater value of the mark than average. In the case of dark matter haloes, we expect that haloes in overdense environments have more close neighbours than haloes in underdense environments (some caveats to this interpretation are discussed in Section 2.3). Therefore the contribution of haloes in overdense environments dominates $\xi_{\rm marked}(r)$ on small scales. On large scales, meanwhile, we expect to recover the global average, $\xi_{\rm marked}(r) = 1$. If we see that $\xi_{\rm marked}(r)$ deviates from 1 on some scale we may interpret this as an environmental dependence of the mark.

Notice we do not have to choose a scale on which to study this dependence; the marked correlation function tells us the scale. This is clearly desirable, but comes at the cost that there is no straightforward correspondence between environment as defined by the marked correlation function and environment as defined by the overdensity in some region near the halo. We do note, however, that Sheth (2005) has developed a halo model interpretation of marked statistics, which we do not pursue in detail here.

2.2.1 Choice of mark

In principle one could choose to measure the marked correlation function using any of a whole range of halo properties as the mark, in order to investigate the environmental dependence of those properties. Here, although we wish to study the environmental dependence of halo formation redshift, it may not be best to use this as the mark. Instead, for the majority of our results we follow Sheth & Tormen (2004b) and use a 'scaled formation redshift' for our mark. The definition of scaled formation redshift, used here and by Sheth & Tormen (2004b), is the $\tilde{\omega}_{\rm f}$ parameter defined in equation 2.31 of Lacey & Cole (1993). Suppose we measure formation redshift relative to some final time z_0 (here, we always take $z_0 = 0$), and consider a halo with mass M_0 at z_0 and which formed at a

redshift z_f. Then $\tilde{\omega}_f$ is given by

$$\tilde{\omega}_f = \frac{\delta_c(z_f) - \delta_c(z_0)}{\sqrt{\sigma^2(M_0/2) - \sigma^2(M_0)}} \quad , \tag{2.2}$$

where $\delta_c(z)$ is the critical density threshold for collapse and $\sigma^2(M)$ is the linear theory variance of density fluctuations at mass scale M.

The motivation for using $\tilde{\omega}_f$ rather than z_f as the mark comes from the following predictions of extended Press-Schechter theory: firstly, that the distribution of $\tilde{\omega}_f$ depends very weakly on the initial power spectrum of fluctuations; and secondly, that for a power-law initial power spectrum, the distribution of $\tilde{\omega}_f$ is independent of halo mass. The latter prediction still holds to very high accuracy for more general power spectra with slowly varying slope. Moreover, the prediction is largely confirmed by measurement of the distribution in our simulation. This is demonstrated in Fig. 2.3, where the mean formation redshift of haloes in the Millennium simulation is plotted as a function of mass. For comparison, we plot the mean value of $\tilde{\omega}_f$ as a function of mass on the same scale. Clearly $\tilde{\omega}_f$ scales out much of the dependence of halo formation redshift on halo mass.

This can be seen in more detail by comparing Fig. 2.4a, which shows the distribution of formation redshift for haloes in different mass bins in the simulation, with Fig. 2.4b, which shows the distribution of $\tilde{\omega}_f$ for the corresponding haloes. In Fig. 2.4a we can easily see that haloes of different masses have very different distributions of formation redshift, and that there is a clear trend of larger mass haloes having a more strongly peaked distribution with a peak at smaller redshift. In Fig. 2.4b, however, we see that the distribution of $\tilde{\omega}_f$ is quite similar for haloes of different mass, and that there is no such clear trend. Fig. 2.4b also shows the analytic prediction for this distribution, which can be seen to be a reasonable approximation. The analytic form captures the shape of the distribution well, though it appears to predict a distribution peaking at smaller $\tilde{\omega}_f$. We show both the analytic distribution calculated using the actual input power spectrum of the Millennium Simulation, and the closed form for a power-law initial power spectrum with index $n = 0$ (Lacey & Cole, 1993). Note the very weak dependence of the distribution on power spectrum.

The main benefit of defining our mark in this way is that we may now be justified in calculating the marked correlation function for a set of haloes which span a broad range in mass, thereby utilizing the full statistical power of our simulation. Such a function would not have been easy to interpret using z_f as the mark, since it is well established that the halo mass function depends on local density: in high-density regions, it becomes

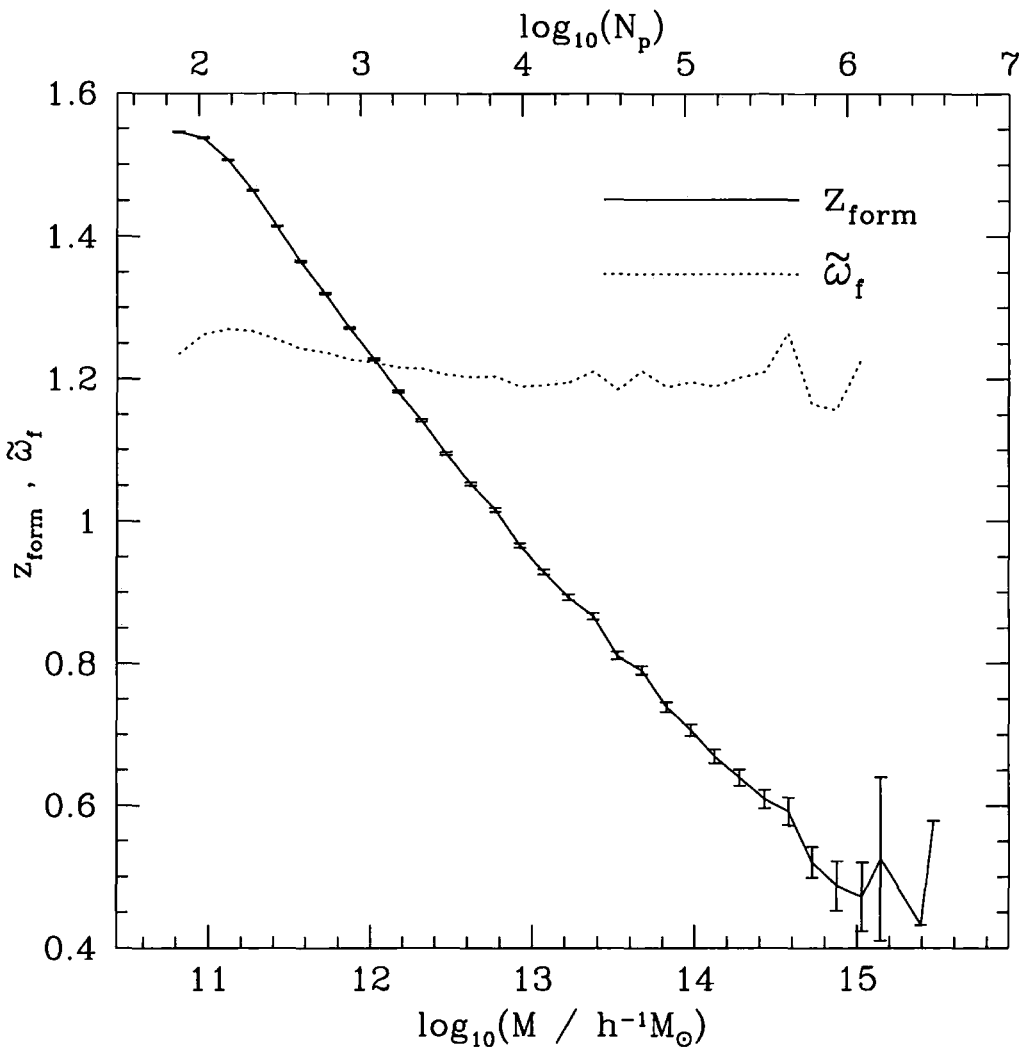

Figure 2.3: The solid line with error bars gives the mean formation redshift of haloes in the Millennium Simulation as a function of the mass of the halo (lower horizontal axis) or, equivalently, the number of particles in the halo (upper horizontal axis). The error bars come simply from the Poisson error on the number of haloes in each bin of mass in the simulation. The dotted line, which exhibits a much weaker mass dependence, shows on the same scale the mean value of the scaled formation redshift, $\tilde{\omega}_f$ (see Equation 2.2 for a definition), of haloes as a function of halo mass.

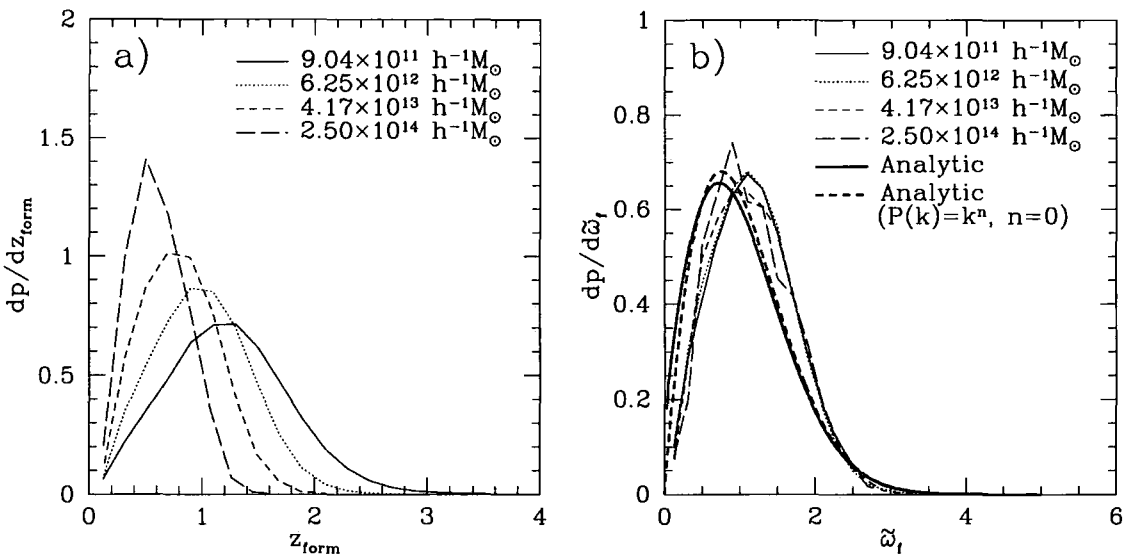

Figure 2.4: The distribution of halo formation redshift (left-hand panel) and of scaled formation redshift $\tilde{\omega}_f$ (right-hand panel). The distribution is shown for haloes in four different mass bins spaced equally in log(halo mass) and centred on the mass given in the legend. The trend in the left-hand panel is such that haloes of larger mass have a more strongly peaked distribution, with the peak at smaller redshift. In the right-hand panel, we show in addition the analytic prediction for the distribution of $\tilde{\omega}_f$ (which is very nearly independent of mass) with thicker, smoother lines. The thick, solid line shows the prediction using the input power spectrum for the Millennium Simulation, while the thick, dashed line shows the prediction using a power-law initial power spectrum with index $n = 0$.

skewed towards more massive haloes (Frenk et al., 1988; Cole & Kaiser, 1989; Lemson & Kauffmann, 1999; Gottlöber et al., 2003; Mo et al., 2004). Because these more massive haloes tend to have formed more recently, we could not have been sure that any signal in the marked correlation function was not due merely to the environmental dependence of the mass function, rather than of mean halo formation redshift for haloes of a given mass. This effect could also have swamped any genuine signal from an environmental dependence of formation time.

2.3 Results and extensions

A calculation of the marked correlation function of haloes with mass between 3.11×10^{12} and 3.11×10^{14} h^{-1} $M_\odot$ at $z = 0$ is given in Fig. 2.5a (our results will be for $z = 0$ throughout). We write the halo mass in terms of the characteristic mass M_*, where M_* is defined in the usual way such that $\sigma(M_*) = \delta_c$, and where $\delta_c(z = 0) = 1.674$ for the cosmology

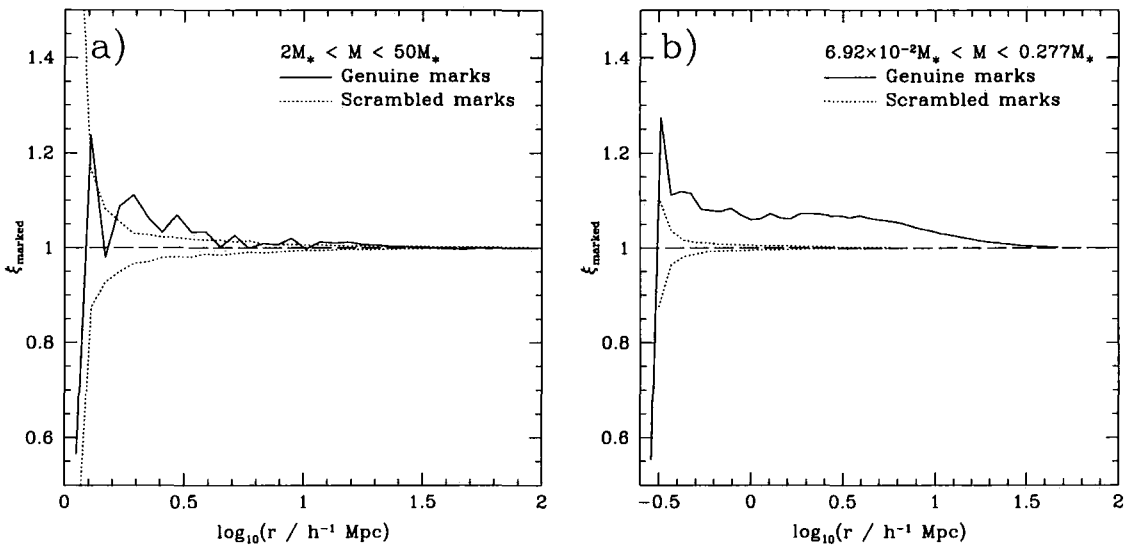

Figure 2.5: The marked correlation function (using $\tilde{\omega}_f$ as the mark) of haloes with mass, M, in the range shown (solid line). In the top panel, this corresponds to haloes with a number of particles, N_p, such that $14\,441 \leq N_p \leq 361\,036$ (there are 7221 particles in an M_* halo). There are 34 241 haloes in this mass range in the Millennium Simulation. In the right-hand panel, the haloes have between 500 and 2000 particles. These haloes have a mass such that we typically expect them to host a single bright galaxy.

assumed here. M_* haloes are both well resolved and numerous, containing 7221 particles and having a mass of $6.21 \times 10^{12}\ h^{-1}\ \mathrm{M}_\odot$ at $z = 0$ in the Millennium Simulation. The peak in the function at intermediate scales indicates that haloes in pairs with these separations have a mean formation redshift which is higher than the global average for haloes of this mass. The function tends to 1 at large scales, as expected. At smaller scales than those plotted, i.e. less than approximately 1 h^{-1} Mpc, the marked correlation function is not defined for haloes of this mass, since there are no pairs of haloes in this mass range at such small separations. Clumps of mass closer than this will tend to be identified as part of the same structure by the group-finder.

The sense of the dependence (higher formation redshifts in denser regions) is that predicted by Sheth & Tormen (2004b) from the results of Lemson & Kauffmann (1999). They noted that when the distribution of formation times (averaged over haloes of all mass) was plotted for haloes residing in regions of different overdensity (measured in a spherical shell between 2 and 5 h^{-1} Mpc centred on the halo), the curves were very similar, i.e. the distribution of halo formation redshifts was independent of local density. This seems inconsistent with the fact that denser regions tend to host more massive

haloes, which have, on average, more recent formation times (see Fig. 2.3). One might expect that because the distribution is calculated by averaging over all haloes for each bin in overdensity, the distribution should shift to lower formation redshifts in more dense regions, but this was not observed. This could be explained if haloes of a given mass tend to have higher formation redshifts in more dense regions. No such signal was observed in the GIF simulations, which motivates the use of a more sensitive test of environmental dependence. It also suggests using simulations of larger volume, since while the volume of the GIF simulations may have been sufficient to detect a variation in the distribution of formation times when averaging over haloes of all masses, it was not sufficient for Lemson & Kauffmann (1999) to detect a variation in the mean formation redshift as a function of local overdensity for haloes in some narrow range in mass. The Millennium Simulation offers the opportunity to do this (and to extend the study to haloes of lower mass) and we do so below.

Rather than plot error bars on the (correlated) points of Fig. 2.5a, we attempt to assess the significance of any signal similarly to Sheth & Tormen (2004b). That is, we take the population of haloes used to calculate the marked correlation function, then shuffle their marks randomly and recalculate the marked correlation function 100 times. For each radial bin, we calculate the mean of these 100 realizations of the marked correlation function and the standard deviation between realizations. The mean plus or minus one standard deviation is shown by the dotted lines in Fig. 2.5.

We have also tried to quantify the systematic error induced by including haloes over such a large mass range. We repeat the procedure used to obtain the dotted lines of Fig. 2.5a, but instead of shuffling marks over our entire sample of haloes, we sort the haloes into eight mass bins. Then we only shuffle the marks within each bin in mass. Therefore, although a halo receives the mark of a random halo in the sample, it is only permitted to receive the mark of a halo with a very similar mass. We then take the mean and standard deviation in each radial bin of the realizations of the marked correlation function as before. This binning procedure makes very little difference, in fact, and gives us confidence that the $\tilde{\omega}_f$ parameter scales out the mass dependence of halo formation redshifts sufficiently well for the purposes of this test.

To give a numerical indication of the strength of the signal, we calculated the marked correlation function in one large bin between 1 and 5 h^{-1} Mpc and estimated the error using the same shuffling procedure as before. This indicated that the value of $\xi_{\rm marked}$ was inconsistent with unity at the 5σ level. It is the large volume of our simulation which

enables us to see a signal in the marked correlation function of such massive haloes, but we find that the behaviour of samples of haloes of lower mass is similar. Moreover, the dynamic range of the simulation is such that we can study relatively small haloes, robustly determining formation times of haloes down to a mass of $5.5 \times 10^{10}\ h^{-1}\ \mathrm{M}_{\odot}$. For galaxy-sized haloes with between 500 and 2000 particles, for example, we see a larger environmental dependence. The marked correlation function for haloes of this mass is given in Fig. 2.5b. The abundance of haloes of this mass means that the error in the determination of the marked correlation function is negligible at most scales of interest. The excess at small separations is more significant than for the more massive haloes, and the size of the effect is also larger. This is qualitatively consistent with Gao et al. (2005) since the effect for which they tested (a variation in clustering amplitude with halo formation redshift) was larger for haloes of lower mass.

Splitting the mass range used in Fig. 2.5a into four parts gives the result shown in the lower four panels of Fig. 2.6. Firstly, it is clear that the estimates of ξ_{marked} in Fig. 2.6 are far more noisy; while the mass range covered in Fig. 2.5a contains 34 241 haloes in the Millennium Simulation, the lower four panels of Fig. 2.6 cover mass ranges containing, in order of increasing mass, 18 384, 9172, 4298 and 2387 haloes respectively. Since the quality of the statistics is governed by the number of halo *pairs*, the effect is noticeable even given the large volume of the simulation. This highlights the importance of properly scaling out the mass dependence of halo formation redshift, so that we may average over large ranges in halo mass.

For similar reasons, (i.e. the effect of cross-correlations between bins) the marked correlation function for the whole mass range of Fig. 2.5a is not simply the average of the marked correlation function of each of the four sub-ranges. For example, if we perform the test described above of calculating the marked correlation function for one large bin between 1 and 5 h^{-1} Mpc, we see that the function for the range $2M_* < M < 4M_*$ is greater than unity only at the 1σ level. In the highest mass range, the function in this radial bin is less than unity, by approximately 1.5σ. One would normally dismiss this apparent change in the sign of the environmental dependence as insignificant, especially given our free choice of bin size and the freedom in the definition of the halo catalogue and merger trees, but it is qualitatively consistent with fig. 4 of Sheth & Tormen (2004b). In the amalgamated sample, of course, most of the halo pairs which include a member in the highest mass bin have one member of the pair from a lower mass bin. It may therefore still be the case that the product of the marks of the haloes in such a pair with

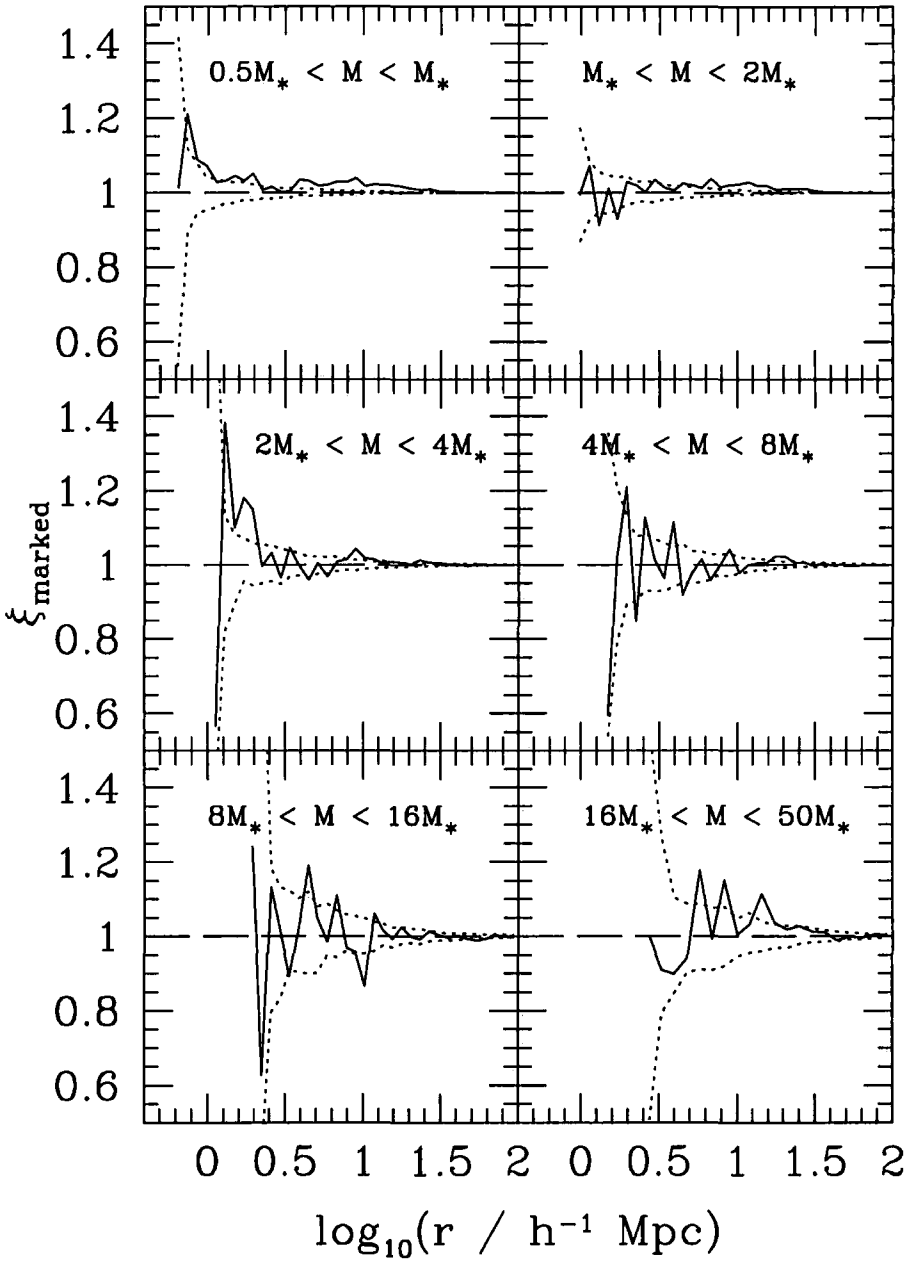

Figure 2.6: The marked correlation function of haloes with mass in the ranges shown (solid lines), with $\tilde{\omega}_{\rm f}$ as the mark. Dotted lines are calculated as in Fig. 2.5a. The top four panels may be compared with fig. 4 of Sheth & Tormen (2004b) since the value of M_* in their simulation is approximately twice ours. Note, though, the difference in axis scale, and the fact that in their figure formation redshift is used for the mark, whereas here $\tilde{\omega}_{\rm f}$ is used (see Fig. 2.7 which shows this does not affect our conclusions). The lower four panels cover the same mass range as Fig. 2.5a.

separation r is usually greater than $\bar{m}^2$, and yet a halo pair of separation r in which both members are from the highest mass bin usually gives a product of marks less than $\bar{m}^2$. This is a barrier to the clean interpretation of these results, since when measuring the environmental dependence of haloes in some mass range, the environment can only be defined in terms of haloes in the same mass range. We address this problem by explicitly separating the 'tracer' population from the 'marked' population in Section 2.3.1 below.

Recall that the small-scale cutoff in the marked correlation function occurs because there are no haloes in the given mass range which occur at such small separations in the simulation: an exclusion effect. The radius at which this occurs depends on mass, and certainly this effect is noticeable when comparing the top-left panel of Fig. 2.6 to the bottom-right panel.

This dependence on halo mass of the scale upon which we can measure environment again suggests separating the tracer and marked populations, as we do when calculating a marked cross-correlation function below. Of course, some dependence is inevitable since more massive haloes tend to have larger radii. This reinforces the point that a method in which we choose beforehand a fixed scale on which to measure environment – looking at scales at which there is a peak in the marked correlation function for low mass haloes, say – may be flawed, since the outer regions of more massive haloes will contribute to the definition of their own environment.

We emphasized earlier the importance of being able to calculate a marked correlation function for a sample of haloes which spans a large range in mass, and suggested a scheme for scaling out the mass dependence of halo formation times based on the analytic work of Lacey & Cole (1993). One can easily imagine other ways to scale out this dependence, however, and we attempt to show the difference between various methods in Fig. 2.7. For the solid line we make no attempt to correct for the mass dependence of halo formation redshift and simply use z_f as the mark, while for the other three lines some kind of scaling is applied. The short-dashed line is the result for our fiducial mark, $\tilde{\omega}_f$. The dot-dashed line uses the simulation itself to determine the scaling: we simply divide the formation redshift for each halo by the mean formation redshift for haloes of that mass. This does not take into account changes in the shape of the distribution of formation redshift as a function of mass. For the dotted line we first calculate $\tilde{\omega}_f$ for each halo, as above. Then we rank the haloes in order of $\tilde{\omega}_f$ and reassign each one a mark, preserving the ranking, such that the final distribution of marks is precisely the analytic distribution given by the thick, solid line of Fig. 2.4b. This explicitly enforces near-mass independence,

hopefully without distorting the shape of $\xi_{\rm marked}$ too much since the shape of the analytic distribution matches the measured distribution quite well. It seems from Fig. 2.7 that any reasonable method for scaling out the mass dependence of the distribution of halo formation redshift gives similar results.

The errors in the marked correlation functions measured with these four different marks are very similar, and the effect of shuffling only within narrow mass bins remains small in each case. Indeed, when we force the marks to follow the analytic distribution for $\tilde{\omega}_{\rm f}$ we might expect it to make no difference whether we shuffle between haloes of all masses or only between haloes of similar mass, and we have checked that this is indeed the case. Fig. 2.7 gives us confidence that our conclusions about the environmental dependence of halo formation redshift are robust to changes in the precise definition of the mark, so long as the mark remains a reasonable proxy for the halo formation redshift as defined in Section 2.1.1, and so long as the width of the distribution of marks remains similar. We conclude, therefore, that we have significant evidence that halo formation redshift does depend on environment, and we explore this in more detail in what follows.

2.3.1 A marked cross-correlation function

Even the marked correlation functions we calculate above which include haloes in a wide range of mass (up to a factor of about 25 between the lowest and highest mass) utilise only a fraction of the dynamic range available in the Millennium Simulation. We are more limited by the fact that the wider the range of mass studied, the harder the marked correlation functions are to interpret. If we include very small haloes, then because low mass haloes are more abundant, the function will be dominated at all scales by contributions from low mass haloes. The contribution from haloes of any given mass only cuts in above some scale determined by the exclusion effect from the non-zero size of the halo. On the other hand, if we wish to study the environmental dependence of the formation times of only very massive haloes, we will have poor statistics even when simulating enormous volumes, and it will not be clear in any case that such massive haloes are good tracers of environment. We have attempted to address some of these problems by defining a marked cross-correlation function.

Consider two populations of haloes, which we denote the 'tracer' population and the 'marked' population. We then define the marked cross-correlation function, $\xi^{\rm cross}_{\rm marked}(r)$,

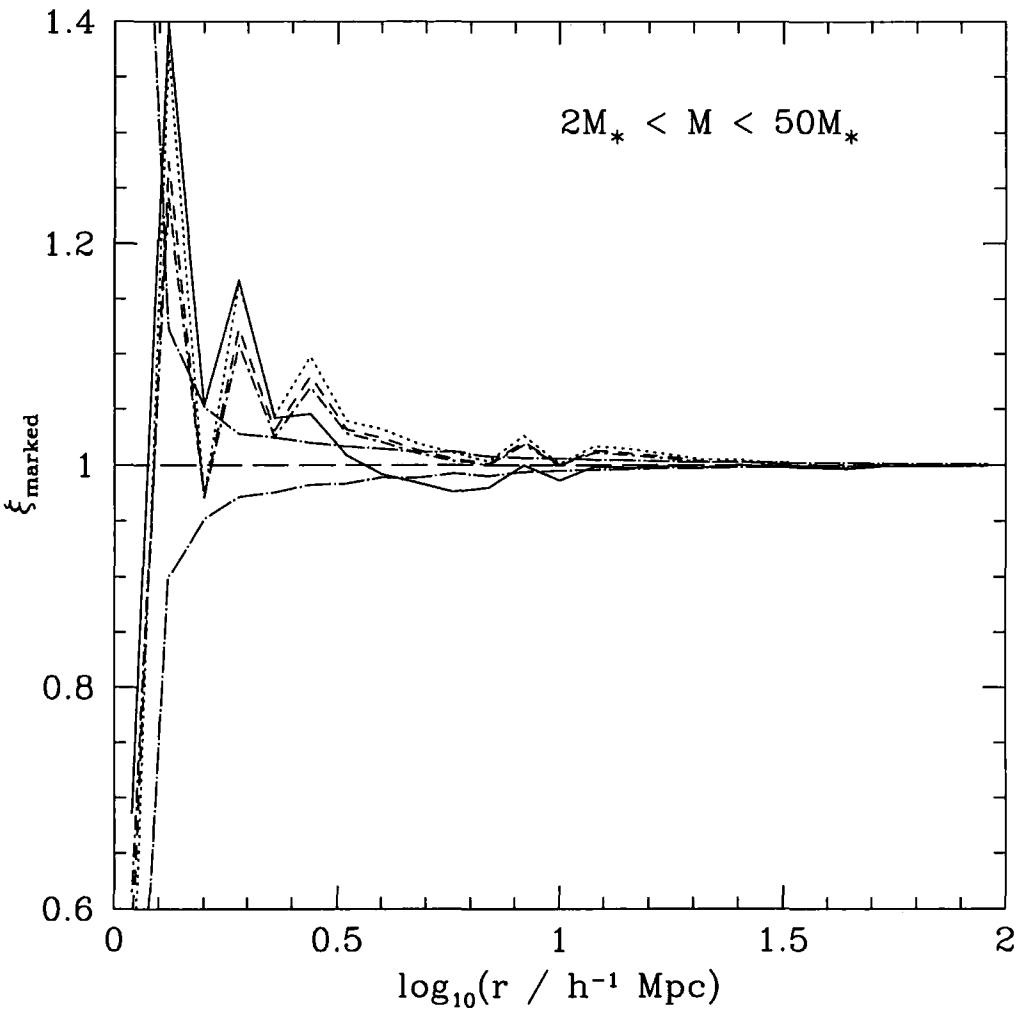

Figure 2.7: The marked correlation function with several different choices of mark. In each case the population of haloes used is the same as in Fig. 2.5a, but we vary the choice of mark as follows: solid line — formation redshift; short-dashed line — $\tilde{\omega}_f$; dot-dashed line — formation redshift divided by the mean formation redshift for haloes of that mass (determined from the simulation); dotted line — haloes are ranked by $\tilde{\omega}_f$ then reassigned a mark (preserving this ranking) such that the marks follow the analytic distribution for $\tilde{\omega}_f$ given by the thick, solid line in Fig. 2.4b. The long-dashed line through $\xi_{marked} = 1$ is shown to guide the eye. The dispersion in ξ_{marked} in the scrambled catalogues is shown only for a mark of $\tilde{\omega}_f$ (dot-long-dashed lines), since it is very similar in each case.

by

$$\xi^{\rm cross}_{\rm marked}(r) = \sum_{\{i,j \mid r_{ij}=r\}} \frac{m_j}{n(r)\bar{m}} \quad , \tag{2.3}$$

where the sum is now taken over pairs $\{i, j\}$ such that halo i is from the tracer population and halo j is from the marked population, $n(r)$ is the number of such pairs of separation r and $\bar{m}$ is the mean mark of the haloes in the marked population. This tells us about the environmental dependence of the mark in the marked population, with environment defined in terms of the tracer population. It retains the property that a deviation of the function from unity indicates environmental dependence. Note, however, that it does not have some of the properties of a normal cross-correlation function: it will be different if we exchange the marked and tracer populations, and the marked cross-correlation function of a population with itself is not equivalent to the marked autocorrelation function.

Fig. 2.8 gives six examples of marked cross-correlation functions with $\tilde{\omega}_{\rm f}$ as the mark. We estimate the dispersion among realizations of the functions by recalculating the function 100 times with the marks shuffled, as before. The tracer population is the same in each panel, but the mass of the marked population increases from left to right and from top to bottom. For the higher mass populations there seems to be a trend that as the mass of the marked population increases, the positive signal from the marked cross-correlation function becomes weaker, perhaps even changing sign when the mass of the marked haloes becomes greater than that of the tracer haloes. Since we expect individual L_* galaxies to occupy haloes containing approximately 1000 particles in this simulation (a halo with 1000 particles has a mass of $0.138M_* = 8.61 \times 10^{11}\ h^{-1}\ {\rm M}_\odot$), the results for lower mass populations suggest we have significant evidence that galaxy-sized haloes near $6 \times 10^{13}\ h^{-1}\ {\rm M}_\odot$ haloes have earlier formation times than the mean.

Comparing to the marked autocorrelation function, then, the most puzzling panels of Fig. 2.8 are the lower right panel and, to a lesser extent, the lower left panel. The trend in the marked cross-correlation function in the lower right panel is in the opposite sense to that which one may expect having seen the earlier results (less than unity at $\sim 2.5\sigma$ for one bin between 5 and 30 h^{-1} Mpc), while we see no signal in the lower left panel. Recall that we expect more close pairs in more dense regions. This means the marked correlation function at small scales is representative of dense regions, so that we expect to see earlier formation times. This expectation may not hold in the situation represented by the lower right panel of Fig. 2.8, however. While the tracer population consists of haloes with mass near $6 \times 10^{13}\ h^{-1}\ {\rm M}_\odot$, the marked population in this panel consists of very massive

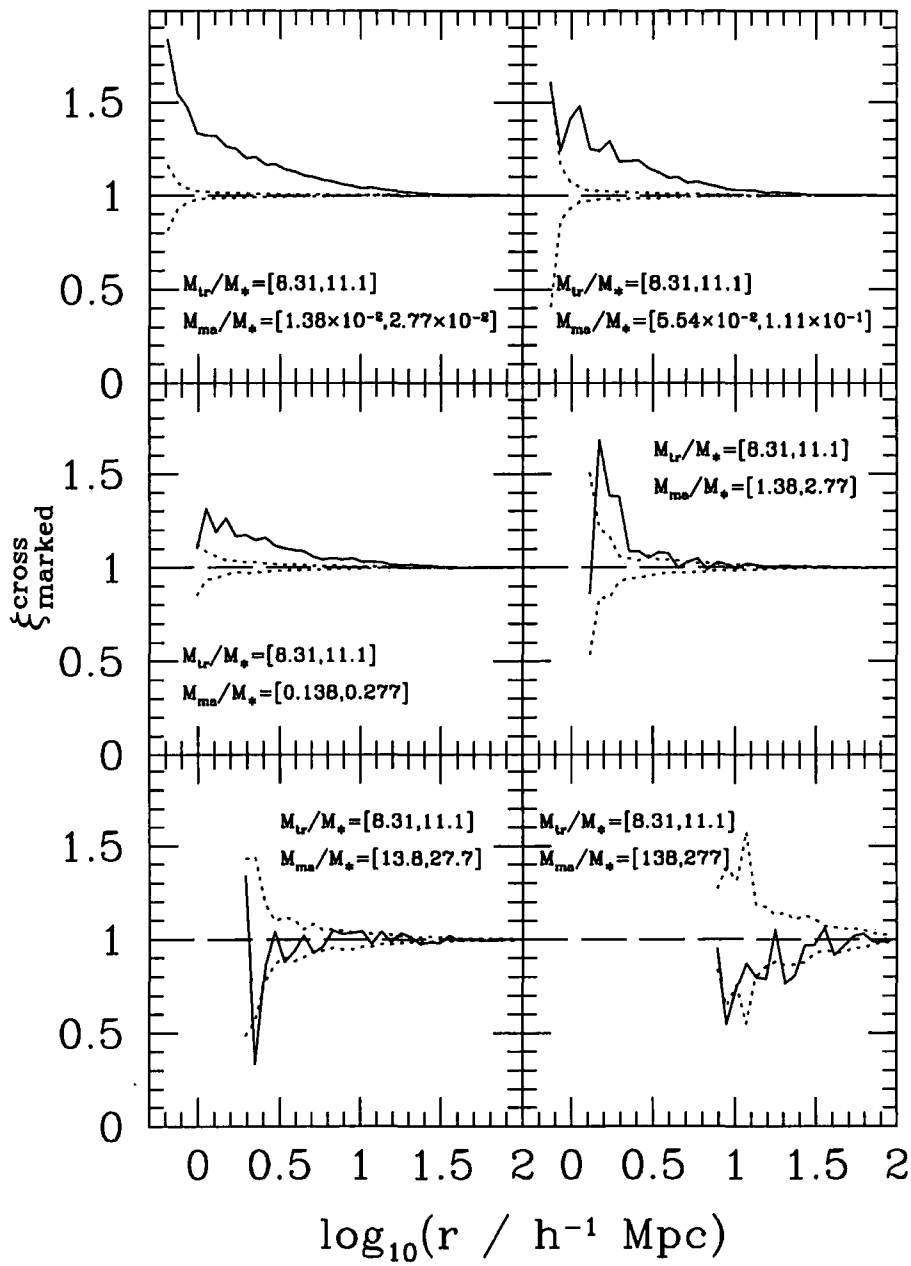

Figure 2.8: Solid lines show the marked cross-correlation function of haloes with the same tracer population ($6 \times 10^{13}\ h^{-1}\ \mathrm{M}_\odot$ haloes) each time, but with a marked population of different mass in each panel. The mark is $\tilde{\omega}_f$. The haloes in the tracer population have mass $M_{\rm tr}$ in the range shown, while those in the marked population have mass $M_{\rm ma}$ in the range shown (recall an M_* halo contains 7221 particles, and a galaxy-sized, 1000 particle halo has mass $0.138M_*$). We again show the dispersion in 100 calculations of the marked cross-correlation function (dotted lines), shuffling the marks at random between haloes each time.

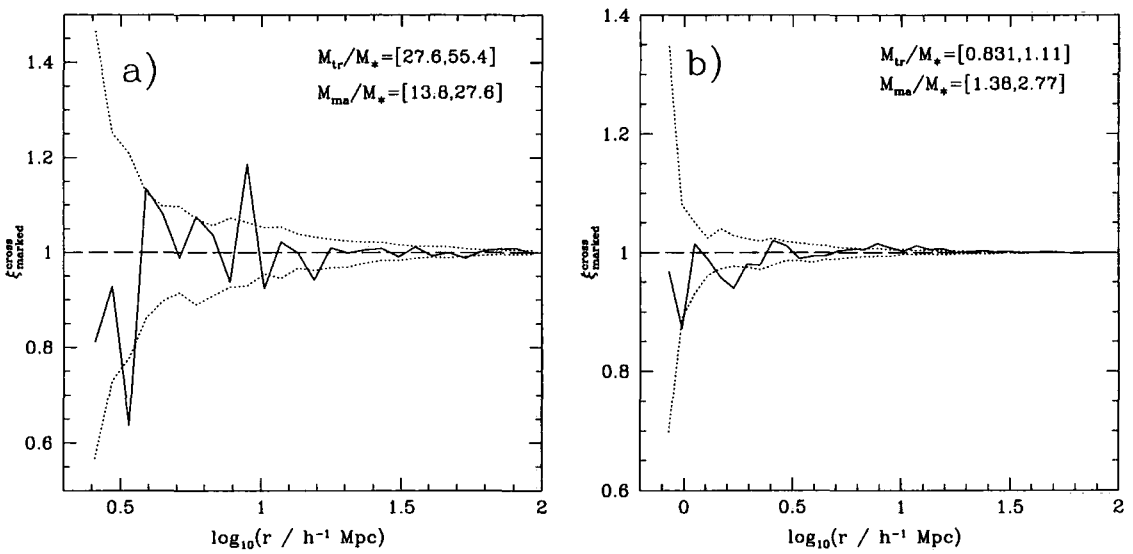

Figure 2.9: The left-hand panel shows the marked cross-correlation function using the same marked population as the lower-left panel of Fig. 2.8. Here, though, we choose the tracer population to be more massive than in Fig. 2.8, and, importantly, more massive than the marked population. The dotted lines are as in Fig. 2.8. The right-hand panel uses the same marked population as the middle-right panel of Fig. 2.8 but with a lighter tracer population.

haloes, of around $10^{15}\ h^{-1}\ \mathrm{M}_\odot$. These large haloes will be found only in regions which are at least moderately dense, and many will be found in the very densest parts of the simulation: in the core of the filaments making up the cosmic web, or at the intersection of the filaments. In these highly dense regions, we expect nearby haloes to also be very massive, whereas it is in the moderately dense regions that $6 \times 10^{13}\ h^{-1}\ \mathrm{M}_\odot$ haloes are most abundant. It may be that by choosing this tracer population, the close pair counts are dominated by haloes in only moderately dense regions, since it is here that our tracer population is most abundant. The large-scale pair counts are more representative of the average environment of $10^{15}\ h^{-1}\ \mathrm{M}_\odot$ haloes, which is even more dense. If this interpretation is correct, we might anticipate that using a more massive tracer population would reverse the trend, so that $\xi^{\mathrm{cross}}_{\mathrm{marked}}(r)$ was once again larger on small scales. We test this prediction in Fig. 2.9a. In this figure the marked population is the same as in the lower-left panel of Fig. 2.8, since this allows us to choose a sufficiently abundant tracer population that is nevertheless more massive than the marked population.

While the signal we see in Fig. 2.9a is weak and more noisy (with only 872 haloes in the tracer population and 2189 haloes in the marked population) there is no repetition of the unexpected trend seen in the lower panels of Fig. 2.8. We have also performed

the converse test, in Fig. 2.9b. That is, we take the marked population that produces a positive signal in the middle right panel of Fig. 2.8, and find the marked cross-correlation function of these haloes with a less massive tracer population. Using lower mass haloes also improves our statistics: there are 26 417 and 20 968 haloes in the tracer and marked population respectively. The positive signal seen in Fig. 2.8 at small scales is wiped out, and if anything there is a weak negative signal. This suggests that a definition of environment using some tracer population only really corresponds with our intuition of what environment should mean (close pairs representing a dense environment) if the tracer population is at least as strongly clustered as the marked population.

2.3.2 A simpler test of environment

Having seen evidence of environmental dependence of halo formation times in the marked correlation function, it is interesting to see whether the volume and dynamic range offered by the Millennium Simulation allow us to see a signal in other measures of environment. For Fig. 2.10 our measure is simply the overdensity in dark matter in a spherical shell between 2 and 5 h^{-1} Mpc from the centre of the halo (where the centre is defined, as before, as the position of the particle in the main substructure of the halo having the least gravitational potential energy). This is the same measure as used in fig. 3 of Lemson & Kauffmann (1999) in which no signal is apparent, despite the simulation being the same as the one which showed evidence of environmental dependence in the marked correlation function analysis of Sheth & Tormen (2004b): both studies used the GIF simulations (Jenkins et al., 1998; Kauffmann et al., 1999). The range in halo mass used for each panel of our plot is the same as in fig. 3 of Lemson & Kauffmann (1999). A clear trend is visible; for the top three panels especially, there is evidence that haloes in regions with overdensities greater than about 1 or 2 have higher formation redshifts. We can follow this trend over a very wide range in overdensity.

Because of the high resolution of our simulation, we may extend this technique to lower mass haloes. Haloes which are expected to host a single, bright galaxy (and — importantly for this analysis — the progenitors of these haloes) are well resolved, containing roughly 1000 particles. Fig. 2.11 is similar to a single panel of Fig. 2.10, but using haloes with between 500 and 2000 particles, corresponding to masses of between 4.30×10^{11} and $1.72 \times 10^{12}\ h^{-1}\ \mathrm{M}_{\odot}$. It is clear we have very significant evidence that haloes in denser regions have higher formation redshifts than the mean, and conversely that haloes in less dense regions have lower formation redshifts than the mean. The size of the effect is

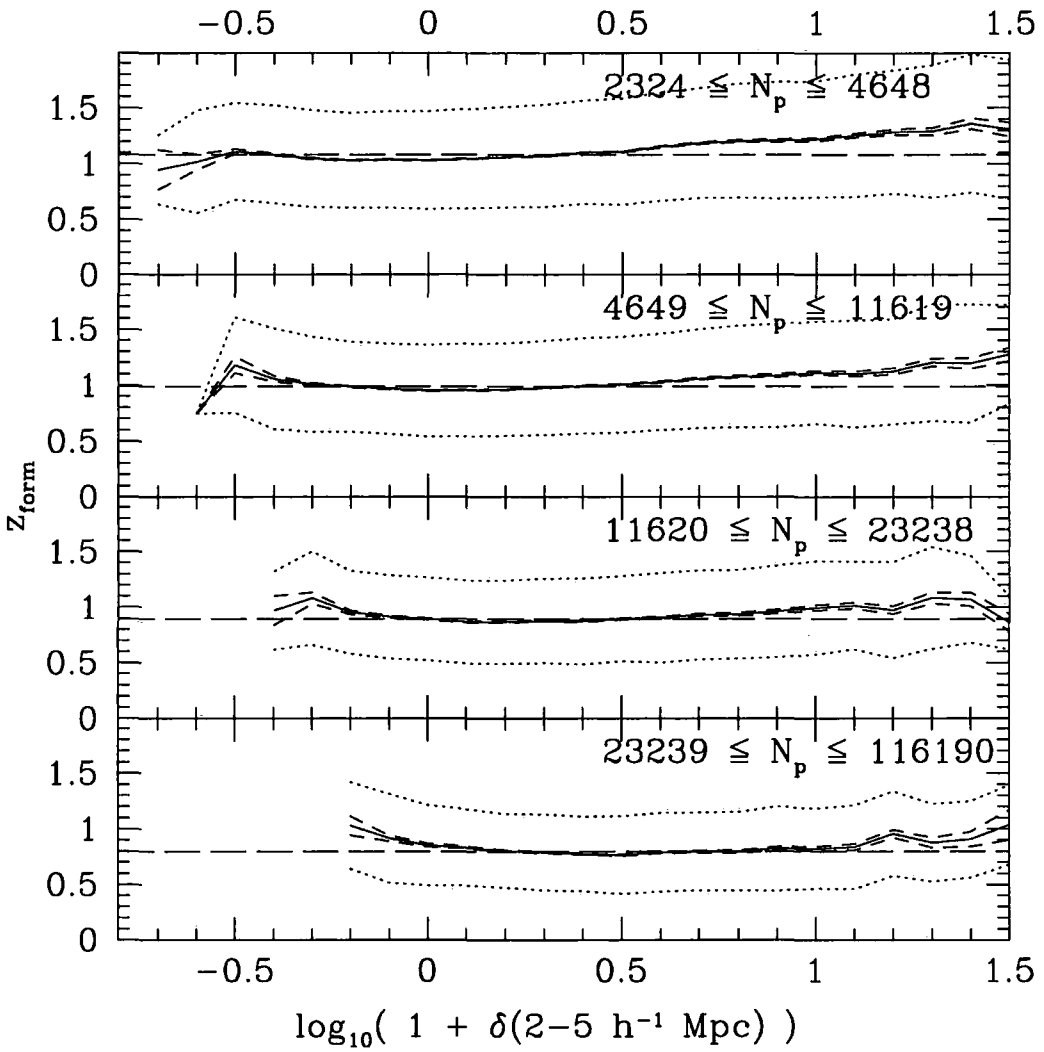

Figure 2.10: The formation redshift of haloes as a function of overdensity in a spherical shell of inner radius 2 h^{-1} Mpc and outer radius 5 h^{-1} Mpc centred on the halo (solid lines). The range of particle numbers for the haloes in each panel is shown; these are chosen so that haloes have the same mass as those in the corresponding panel of fig. 3 of Lemson & Kauffmann (1999). Note the difference in the scale of the horizontal axis between the linear scale of fig. 3 of Lemson & Kauffmann (1999) and the logarithmic scale of this figure which extends to higher densities. Short-dashed lines show the error on the determination of the mean formation redshift in each bin in overdensity. Dotted lines show the 1-σ dispersion in halo formation times. The flat, long-dashed line is at the mean formation redshift for all haloes in that bin in mass, and is shown only to guide the eye.

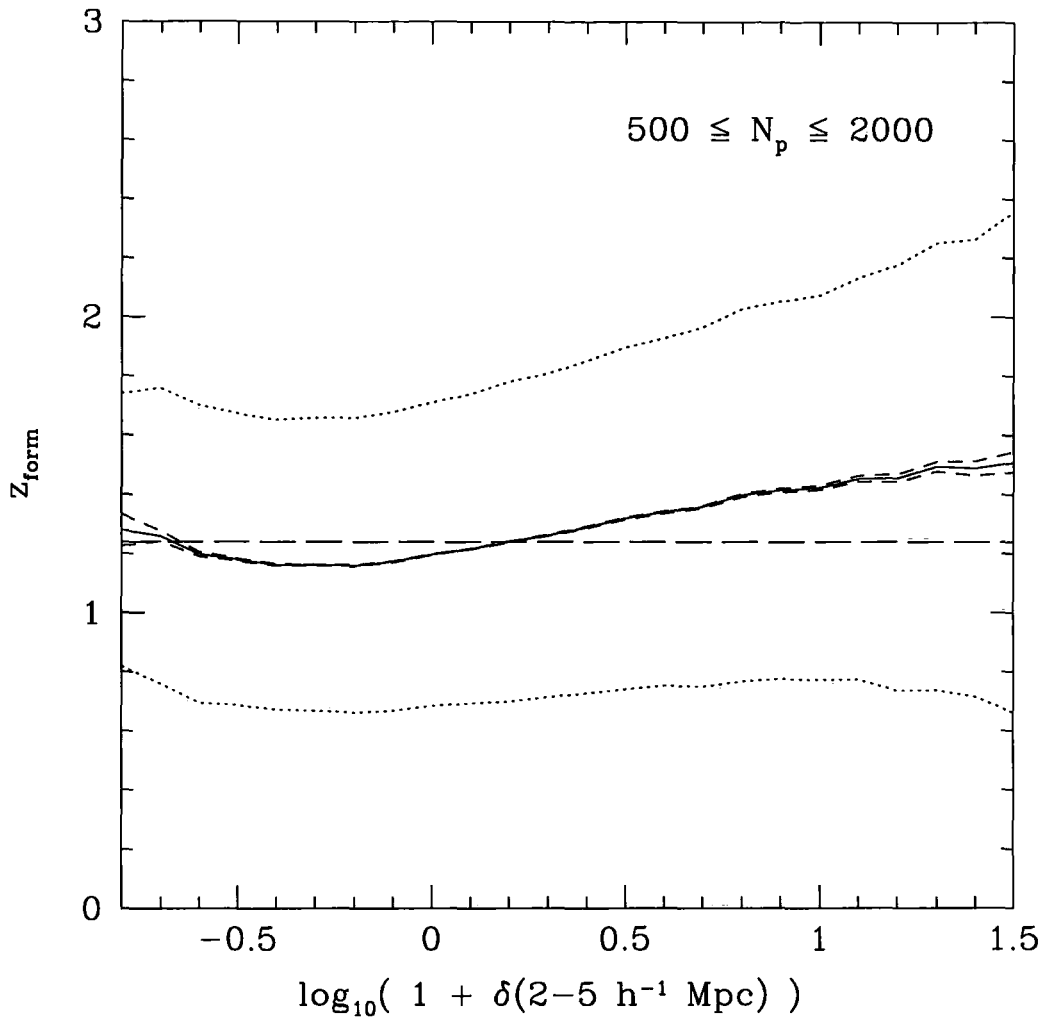

Figure 2.11: As Fig. 2.10, but for haloes with mass such that we may expect them to host a single bright galaxy. The halo sample is the same as for Fig. 2.5b.

similar to that for the more massive haloes (larger, if anything – consistent with Gao et al. 2005), but is detected more cleanly due to the large sample size. Reproducing Figs 2.10 and 2.11 using $\tilde{\omega}_f$ as a proxy for formation redshift gives extremely similar results. The mean is slightly offset, as one would expect from Fig. 2.3, but the trends are identical.

The dispersion in formation times at a given overdensity is larger than the systematic variation between different overdensities. Therefore it is unclear from these data what the effect of this variation will be on, for example, the properties of the central galaxies hosted by these haloes. Gao et al. (2005) use the Millennium Simulation to address the question of how the clustering of haloes of a given mass depends on their formation time, and find a clear difference between the clustering of the oldest and youngest haloes (demonstrated in

our catalogues in Fig. 2.12). It is hard to predict the effect of this difference on observables such as the galaxy correlation function (split by colour or galaxy environment), especially in the light of the fact that galaxies of a given luminosity reside in haloes with a range of mass, with most galaxy light expected to come not from single-occupation haloes such as these, but from group-sized haloes (Eke et al., 2005). Many alternative definitions of halo formation time are possible (see e.g. Li et al., 2005), and some may be more closely related to the properties of the galaxies within the halo (Neistein et al., 2006). We choose the definition used here because it is straightforward and well-studied theoretically. By measuring an environmental dependence we hope to demonstrate that the merger trees show an environmental dependence. We would expect this to be reflected in other properties of the merger trees, including other definitions of halo formation time.

The most sophisticated method we have of predicting the likely galaxy population of a halo given the properties of the halo merger tree is semi-analytic modelling. Semi-analytic galaxy catalogues which use the halo catalogues and merger trees from the Millennium simulation, and which therefore incorporate the full environmental dependence of the halo properties, have been constructed by Bower et al. (2006), De Lucia et al. (2006) and Croton et al. (2006b). The latter catalogues were used by Croton et al. (2006a) to study the effect of the so-called halo assembly bias on galaxy clustering. We adopt a related approach in Chapter 3 to study the environmental dependence of galaxy properties in the catalogues of Bower et al. (2006). Meanwhile, Zhu et al. (2006) have found similar results using a smaller simulation. We defer further discussion of galaxy properties to Chapter 3.

In Fig. 2.11, the mean formation redshift crosses from being being below the global mean for haloes in this mass range (long-dashed line) to above it at an overdensity $\delta \approx 0.6$. It appears this crossing point moves to higher overdensity for more massive haloes: in the bottom panel of Fig. 2.10 the crossing point is at $\delta \approx 5$. We have repeated these calculations and our marked correlation function calculations using different halo catalogues and merger trees, including those of Gao et al. (2005). While the position of this crossing point and the precise shape of the curve are sensitive to the detailed definition of the halo catalogues and the merger trees, the general trends are robust.

Performing the calculations of Gao et al. (2005) using our trees, or our marked correlation function analysis using their trees, gives qualitatively consistent results (our reproduction of the effect demonstrated by Gao et al. 2005 for one particular mass range is given in Fig. 2.12). This is encouraging since the two sets of trees are constructed quite differently, though using the same SUBFIND catalogue. For example, they define the

formation time using the mass within r_{200} (the radius at which the enclosed density falls below 200 times the critical density), whereas we use the mass of the friends-of-friends halo. Also, to find the merger tree of a friends-of-friends halo they follow only the merger history of its main substructure, while we follow the combined histories of each of the substructures which make up the halo. This allows Gao et al. (2005) to track more easily the history of a halo which was temporarily the substructure of a larger halo, but which has since de-merged to become a separate halo in its own right. It is important to deal with these de-mergers well, since they lead to close pairs in dense environments in which one member of the pair is likely to be unusual in some way: for example, it may be assigned an artificially low formation redshift. We note in Section 2.1.1 that we take precisely one merger tree per friends-of-friends halo, discarding the lower mass trees which were split off having been deemed to have been spuriously connected. Including these trees causes de-merger problems since merger tree haloes can split despite remaining in the same friends-of-friends halo (Fig. 2.2 Case 3). On the other hand, using merger trees constructed purely from friends-of-friends catalogues without identifying substructure causes even greater problems, since haloes are often spuriously attached and subsequently split. So long as we take these de-mergers into account, all our results remain robust to the precise definition of the halo catalogue or the merger trees.

We conclude that we have significant evidence that the formation redshift of dark matter haloes is a function of halo environment as well as halo mass. Although we confirm that Press-Schechter theory does a reasonable job of predicting the distribution of halo formation redshifts when averaging over haloes in all environments, we can also see that its prediction that halo formation history is independent of environment must be false. Since we later use semi-analytic models run with Monte Carlo merger trees in order to try to constrain cosmology (Chapter 4) this seems to be a cause for some concern. In fact, the environmental dependence we find violates a basic assumption of any straightforward version of the halo occupation distribution formalism, and calls into question any results based on HOD methods. In the following chapter, therefore, we address these concerns and look for ways to account for environmental dependence when a simulation with sufficient resolution in a cosmologically representative volume is not available.

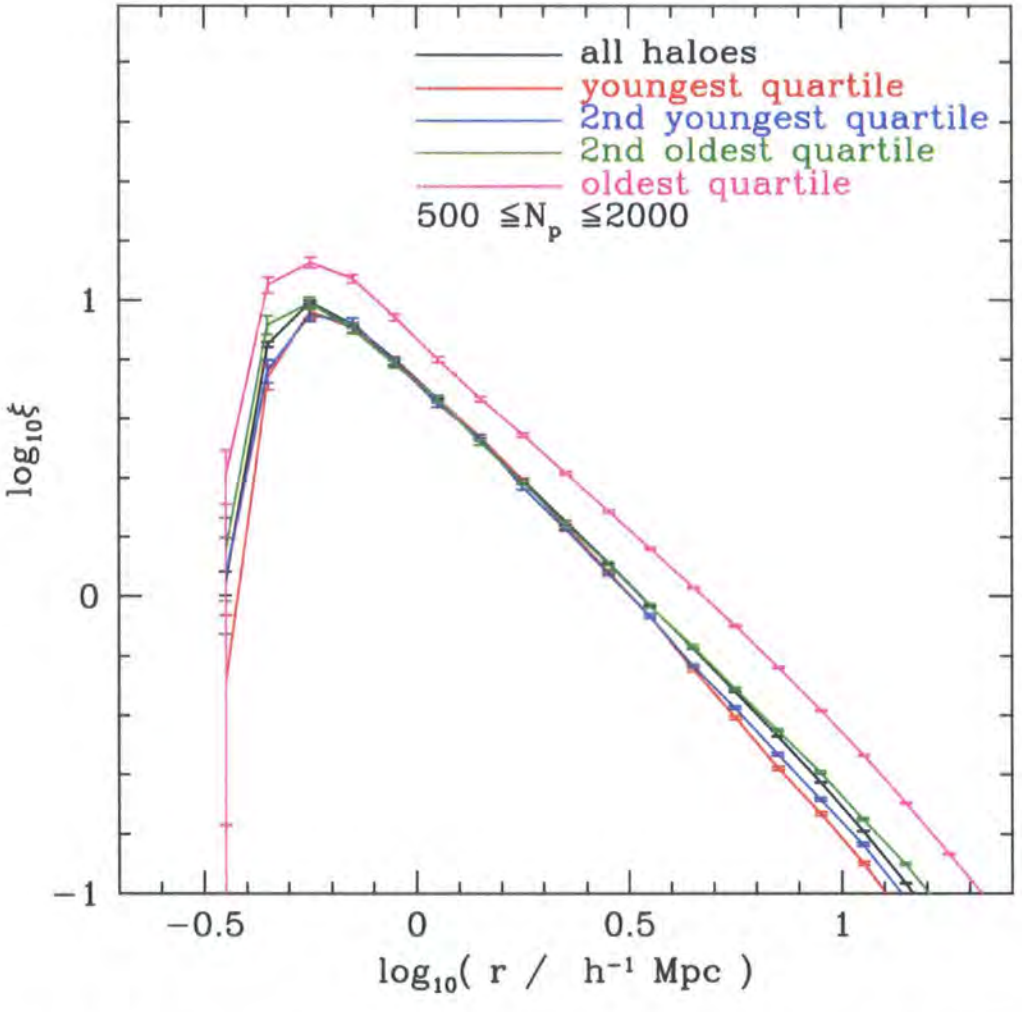

Figure 2.12: The correlation function of haloes with between 500 and 2000 particles as a function of age. The different colours show $\xi(r)$ for the four age quartiles, while the black line shows the correlation function of the whole sample. We reproduce the effect studied by Gao et al. (2005), older haloes of a given mass being more strongly clustered than younger haloes of the same mass, so long as $M \lesssim 10^{13}\ h^{-1}\ \mathrm{M}_{\odot}$. The effect is stronger for lower mass haloes (not shown here).

Chapter 3

The effect of environmental dependence on clustering statistics

3.1 Methods

3.1.1 Semi-analytic model

Our starting galaxy catalogue is produced using the merger trees and particle data from the Millennium Simulation, described in more detail in Section 2.1. The semi-analytic galaxy formation code is the version of GALFORM described by Bower et al. (2006). The developments from earlier versions of the code (Cole et al., 2000; Benson et al., 2003), such as we use to generate the catalogues in Chapter 4, include a more complete treatment of gas ejected from galaxies by stellar feedback. Mainly, though, the addition of feedback from active galactic nuclei in haloes with hydrostatically supported hot gas helps prevent excessive cooling of gas in massive haloes at late times. A suitable choice of the other model parameters then enables the code to produce a galaxy population with the correct luminosity function and galaxy colour distribution. It also correctly predicts the evolution of the stellar mass function and star formation rate to redshift $z = 4.5$ (Bower et al., 2006).

For our purposes, the crucial feature of the model is that it provides a plausible mechanism for linking the merger history of a dark matter halo to the galaxy population of the halo, and therefore hopefully provides a reasonable estimate of the effect of a variation in halo merger history on its galaxy content. Since a more detailed description of the physics is more relevant to our attempts to constrain parameters of cosmological models and semi-analytic codes using clustering measurements in Chapter 4, we defer further discussion of GALFORM to there. Note, though, that the semi-analytic code used

here is independent of that used by Croton et al. (2006a), and implements some of the physical processes involved in modelling galaxy formation differently. As we describe below, our procedure to generate catalogues in which, by construction, the effects of environmentally dependent halo formation are removed is also different from theirs.

3.1.2 Shuffling procedure

In the Millennium Simulation, we have sufficient resolution such that semi-analytic galaxies may be associated with individual dark matter substructures (though there are subtleties to be encountered when dark matter substructures, which are less robust to disruption than their baryonic contents, are destroyed as they fall in to larger haloes). The properties of a dark matter substructure's associated galaxy are linked to the mass aggregation history of the substructure. In most cases to date where a semi-analytic model has been used to populate an N-body simulation with galaxies, however, this has not been the case, especially for simulations of a cosmologically representative volume suitable for comparison to the current generation of galaxy redshift surveys. Insufficient resolution means that merger trees extracted from the simulation provide an inadequate representation of the merger history of a halo, and so Monte Carlo trees based on extended Press-Schechter theory (see Section 1.3.1) have been used instead. The galaxies generated with these Monte Carlo trees do not, therefore, have an associated dark matter substructure in the simulation and so there is some freedom as to how to position the galaxies within haloes. A popular scheme is to assign the position of the halo's central galaxy to the position of the centre of mass of the halo or (our choice) to the position of the particle in the halo with the least gravitational potential energy. A satellite galaxy is assigned the position of a random particle within the halo, so that these galaxies trace the mass within haloes.

The feature of Monte Carlo trees on which we focus in this chapter is that, by construction, their statistical properties depend only upon the mass of the halo for which the tree is generated. That is, they do not include any effect of large-scale environment on halo formation history. Because we wish to focus on this property and not on other differences between using N-body trees and using Monte Carlo trees, we aim to reflect, in our tests using trees which *do* include environmental effects, the way in which Monte Carlo trees are often used. In addition to the catalogue produced directly from the semi-analytic model, then, we generate a catalogue which is analogous to a catalogue which would be produced using Monte Carlo trees (in particular, the galaxy positions are assigned in a way one might assign them when no N-body trees are available). We take the predicted

galaxy population of each friends-of-friends halo and redistribute the galaxies within the halo. The central galaxy remains at the position of the particle with least gravitational potential energy, but the satellite galaxies are reassigned the position of random particles within the halo. As discussed in detail in Section 2.1.1, the algorithm used to generate the merger trees sometimes splits a friends-of-friends halo into two or more pieces and calculates a merger tree for each piece, treating them as separate haloes. In this case a friends-of-friends halo may contain two or more galaxies which have been treated as central galaxies by GALFORM. We label the central galaxy of the most massive part as the central galaxy of the friends-of-friends halo, and treat the other central galaxies as satellites thenceforth. In figures using this catalogue, we denote it the catalogue for which satellite galaxies trace the mass. It is intended to be compared to the shuffled catalogues we describe below, so one might think of it as an 'unshuffled' catalogue.

To generate shuffled catalogues, we assign haloes to bins in mass. We then shuffle which galaxy populations reside in which haloes within mass bins. That is, each halo is given the galaxy population of another halo in the same bin in mass, where the sampling is done without replacement (so that the shuffled catalogues contain all the same galaxies as the unshuffled ones, but in different positions). We then compute the position of galaxies within a halo in the same way as before. By construction, the small-scale clustering should be the same in the shuffled and unshuffled catalogues, since in each case for haloes in which there are satellite galaxies these galaxies trace the halo mass. We expect, however, that the large-scale clustering in the shuffled and unshuffled catalogues will be different due to the assembly bias demonstrated in Chapter 2.

3.2 Results

3.2.1 Effects on the correlation function

The correlation function of a fairly bright galaxy sample from our catalogue is given in Fig. 3.1. Here and in subsequent figures, when we quote a magnitude limit we take $h = 1$ so that $5 \log_{10} h = 0$. We also show the result for an unshuffled catalogue where satellite galaxies are forced to trace the mass in the halo, and for a shuffled catalogue generated as described above. $\xi(r)$ is also given for a 'HOD catalogue'. This catalogue we produce by first computing the mean occupation function, $\langle N(M) \rangle$, of galaxies brighter than the given threshold in our original catalogue. Then for each halo in the simulation, we look up $\langle N \rangle$ for haloes of that mass. If $\langle N \rangle \leq 1$ we assign the halo either 0 or 1 galaxies according

to the nearest integer distribution described in Section 1.2.3 (if there is a galaxy in the halo it is treated as the central galaxy in our placement scheme). If $\langle N \rangle > 1$ then the halo is given a central galaxy, and the number of satellite galaxies is drawn from a Poisson distribution with mean $\langle N \rangle - 1$. This is motivated by the parametrizations described in Section 1.2.3 and justified in our models in Section 4.2.2. The galaxies are placed as for the shuffled catalogues. We also show the correlation function of the dark matter, and perhaps the first observation one could make from the figure is that it shows any of our methods are successful in producing a roughly power-law galaxy correlation function from the curvier dark matter correlation function. More complex features are clearly visible, however, as for the latest redshift surveys (Zehavi et al., 2004). An approximately constant large-scale bias, with galaxies being more clustered than dark matter, is also clearly seen.

The second notable feature is that all the catalogues for which satellite galaxies trace mass give a lower correlation function on small scales than the default catalogue. This suggests that the N-body GALFORM placement scheme tends to give more close pairs in the centre of haloes, and makes it clear why the shuffled catalogues must be compared to an appropriately populated unshuffled catalogue where satellites trace mass, rather than to the default catalogue (Croton et al. 2006a get around this problem by producing shuffled catalogues by translating haloes wholesale rather than repopulating dark matter haloes *in situ*). Further detail is not easy to see in this figure, which is why we go on to plot $r^2\xi(r)$ in Fig. 3.2. The factor of r^2 scales out most of the power-law dependence, and allows us to see the relative shape and amplitude of the correlation function in the different galaxy catalogues more clearly. We did not plot error bars in Fig. 3.1 since they were too small to be visible. The scale of Fig. 3.2 allows us to see them, but they are still rather small because of the large simulation volume. The error bars are visible on the largest scales only because in calculating the large-scale correlation function we randomly sample the galaxy population to speed up the computation.

There are several interesting features in Fig. 3.2. The small scale differences are seen more clearly: $\xi(r)$ in the default catalogue has a slope steeper than r^{-2} on the smallest scales (between 0.01 and 0.1 h^{-1} Mpc), while the other catalogues have a slope shallower than r^{-2}. The small-scale behaviour of the catalogue where satellite galaxies trace the mass and the fully shuffled catalogue is very similar, as one would expect by construction. Straightforward expansion or contraction of the galaxy number density profile within haloes cannot account for the difference between the default and shuffled catalogues on

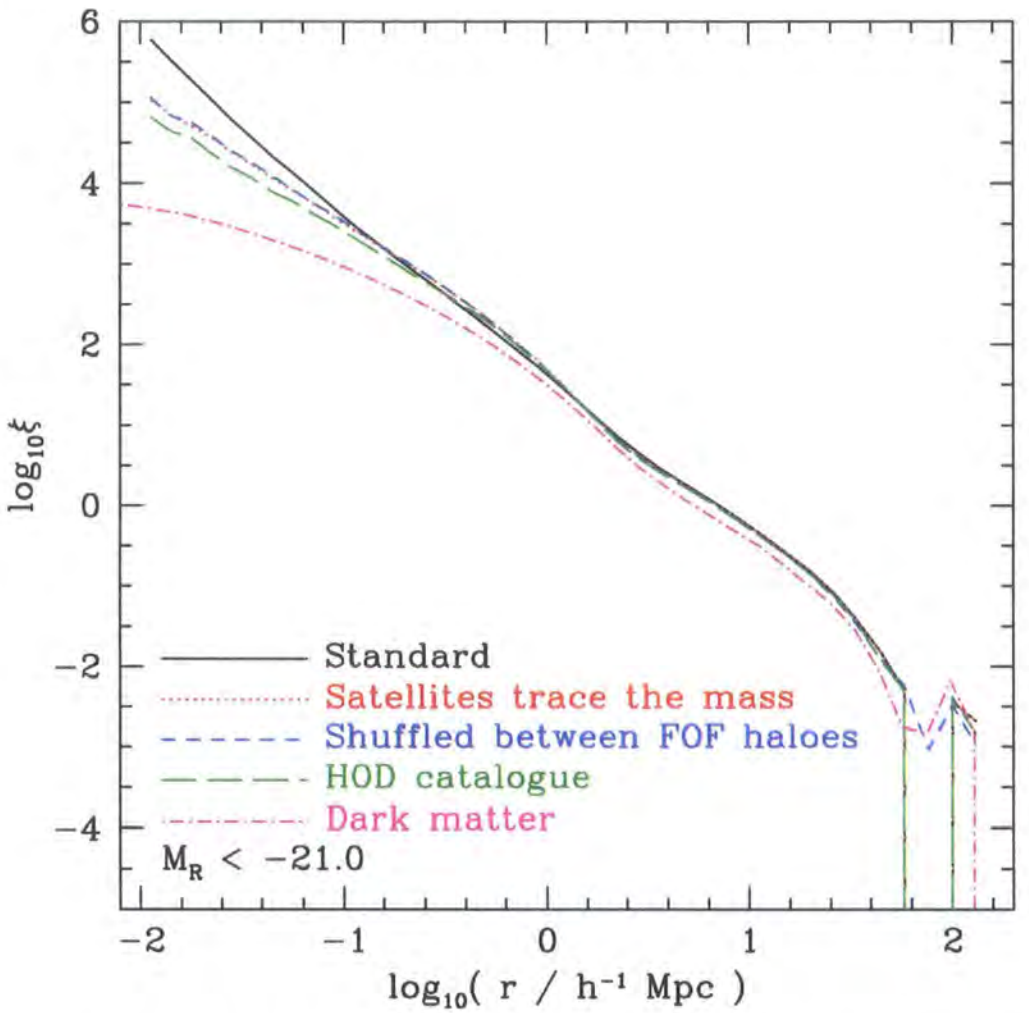

Figure 3.1: The effect on the correlation function of different ways of assigning galaxies to haloes. The solid, black line shows the correlation function of galaxies with the magnitude shown in the default semi-analytic catalogue, with positions determined by the semi-analytic code. The dotted, red line shows the same catalogue, but with galaxies redistributed within haloes, such that while the central galaxy remains on the particle with least gravitational potential energy, the satellite galaxies are placed on random dark matter particles in the halo. The blue, short-dashed line is for the shuffled catalogue, in which a halo's galaxy population is reassigned to a random halo of the same mass, and galaxies are placed within haloes as for the dotted line. The green, long-dashed line is for the HOD catalogue, which we construct by finding the HOD of galaxies of this magnitude in the semi-analytic model and populating the simulation using the resulting $\langle N(M) \rangle$, adopting a reasonable prescription for the scatter about the mean relation. For comparison, the correlation function of the dark matter is given by the magenta, dot-dashed line.

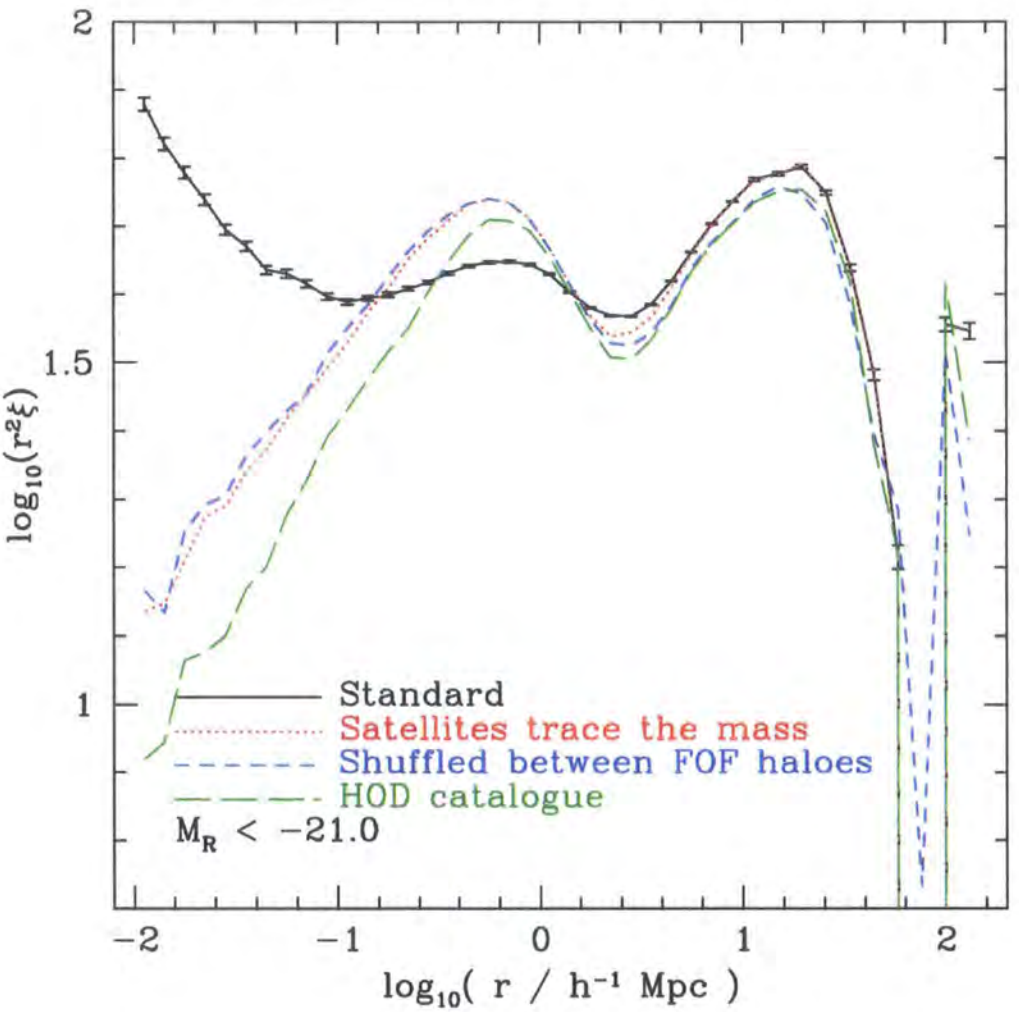

Figure 3.2: The effect on the correlation function of different ways of assigning galaxies to haloes. We plot $r^2\xi(r)$ to show the differences more clearly. Line styles are as for Fig. 3.2, though we do not show the dark matter here. We have added Poisson error bars to the line for the original catalogue; they are too small to be worth plotting for the case where we do not multiply by r^2, but are visible at the smallest and largest scales in this plot.

small scales, since the effect is to decrease or increase uniformly the amplitude of the entire one-halo term (up to $\sim 2\ h^{-1}$ Mpc). It does not seem that the difference between the density profile of halo substructures and the dark matter (e.g., Reed et al., 2005) can account for this difference either. The difference must concern the placement scheme in N-body GALFORM, which involves dealing with galaxies on dissolved substructures amongst other complications. We do not intend to explore it further here, since the most important comparisons will be to the catalogue in which the satellites trace the halo mass. The final point to make concerning the small scales is that the correlation function of the galaxies in the simulation populated with a HOD is again different from the other catalogues. Since the mean occupation function and the placement scheme are the same as for the shuffled catalogue, this can only because we have modelled the scatter in occupation number in haloes of a given mass incorrectly. To give a shift in clustering in the sense we see in Fig. 3.2 probably requires that the GALFORM catalogues have somewhat more scatter than assumed in the HOD catalogue. Since we introduce the HOD catalogues here intending to fix large-scale clustering with modified HODs later, and since the profile on small scales is clearly rather uncertain anyway, this discrepancy is not of too much concern.

On large scales, there is a visible difference between the standard catalogue and the one in which satellites trace the mass on the one hand, and the shuffled and HOD catalogues on the other. We expect identical behaviour in the first two, since the galaxies of the first are merely rearranged within haloes to produce the second, which cannot alter the large-scale clustering. The agreement of the shuffled and HOD catalogues is less trivial, since it could be affected by incorrect scatter about the mean occupation function as on small scales, but it is still expected. The difference between the two unshuffled catalogues, and the two (effectively) shuffled catalogues, demonstrates the effect of the assembly bias detected in Chapter 2 on the galaxy population. The effect is rather small — too small, for example, to affect significantly the cosmological constraints from clustering statistics in Chapter 4. It is very cleanly detected, though. The size of the effect on the correlation function depends on the semi-analytic model parameters for the Munich catalogues subjected to a similar analysis by Croton et al. (2006b), generally being of order 5–20 per cent (D. Croton, private communication), so it could simply be that this GALFORM model is rather less sensitive to the effects of halo assembly bias than the semi-analytic model used by Croton et al. (2006a).

We find that the effect of assembly bias is not strongly luminosity-dependent. An

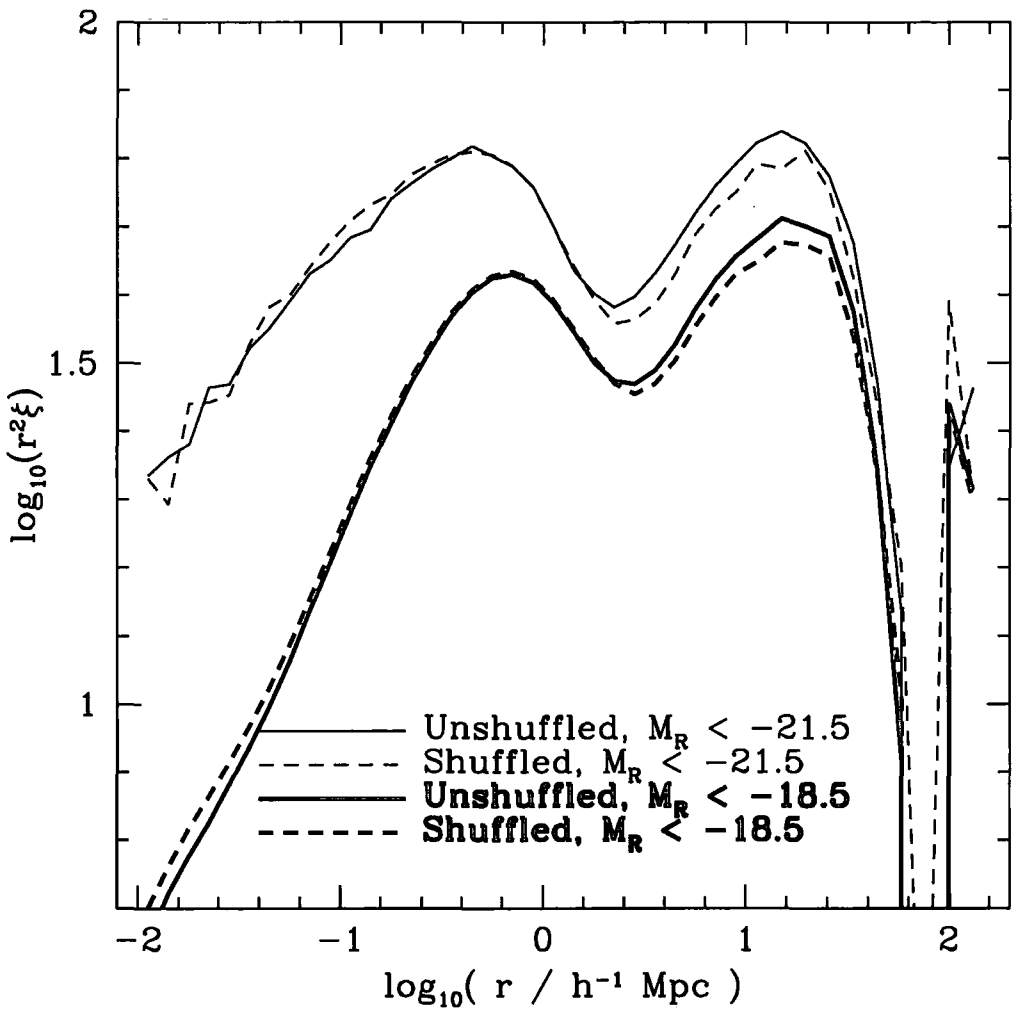

Figure 3.3: The effect of shuffling on $r^2\xi(r)$ for galaxy samples with different luminosity thresholds. Solid lines show the results for the unshuffled samples while dashed lines show the results for the shuffled samples. The thicker (lower) lines are for a faint sample while the thinner (higher) lines are for a bright sample.

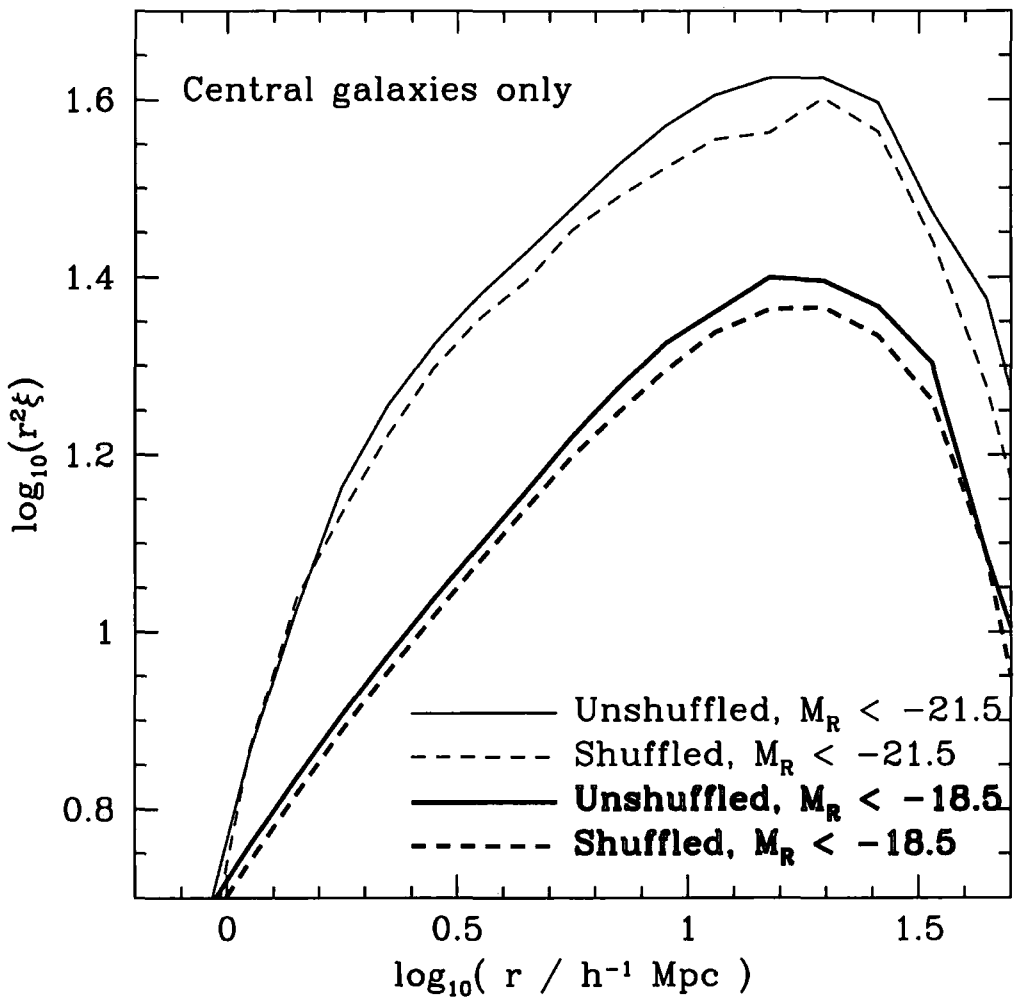

Figure 3.4: As Fig. 3.3, but for central galaxies only. Note we have changed the axis scales since eliminating the satellite galaxies naturally changes the clustering considerably.

example of this is shown in Fig. 3.3, which compares the correlation function of the shuffled and unshuffled catalogues for a bright and a faint sample. Similarly, the effect persists and is of similar size if we restrict the sample to contain only central galaxies, as shown by Fig. 3.4.

The bias also appears not to be strongly colour-dependent. Fig. 3.5 shows $r^2\xi(r)$ for a red sample and a blue sample at two different magnitude thresholds. The red sample is more clustered and its correlation function has a different shape: the difference in amplitude between the red and blue galaxies is larger on small scales than on large scales, possibly because the most massive haloes tend to have a population of mainly red galaxies. Despite these differences, though, the effect of shuffling on large scales is quite

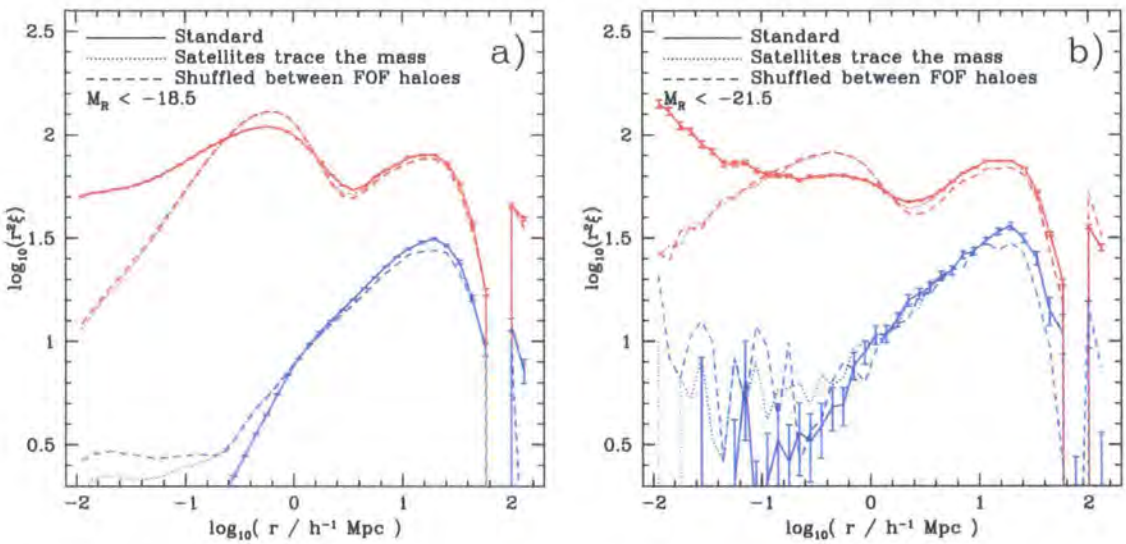

Figure 3.5: The effect of shuffling on $r^2\xi(r)$ for red and blue galaxies. We divide the sample into red and blue along the line $M_B - 0.96M_V = -0.12$, which seems to correspond to a natural divide between the red sequence and the blue population in the colour-magnitude diagram for our galaxies. The result for the red galaxies is shown by the red lines at higher amplitude, and for the blue galaxies by the blue lines at lower amplitude. The left-hand panel is for a faint sample and the right-hand panel for a bright sample.

similar and is of a similar size. This differs from the findings of Croton et al. (2006a), who found that the blue galaxies showed a weaker dependence than the red galaxies, with the sense of the dependence even changing sign. They also differ in their measurement of luminosity dependence: while we always see that clustering is suppressed at large scales in the shuffled catalogue, their fig. 2 implies that this trend is reversed at bright magnitudes. Our result provides us with some encouragement that a relatively simple scheme to correct the clustering of galaxies grown using Monte Carlo trees may work.

3.2.2 The void probability function

The void probability function, $P_0(r)$, is the probability that a sphere of radius r thrown down randomly on the galaxy distribution contains no galaxies. As suggested by Berlind & Weinberg (2002), one might hope for it to be useful in probing the single-occupancy regime of the mean occupation function, since the small haloes in voids will, if they host a galaxy at all, be in this regime. Tinker et al. (2006a) show, however, that once the (environmentally independent) mean occupation function is constrained to produce a given correlation function and to generate a catalogue of a given space density, the void

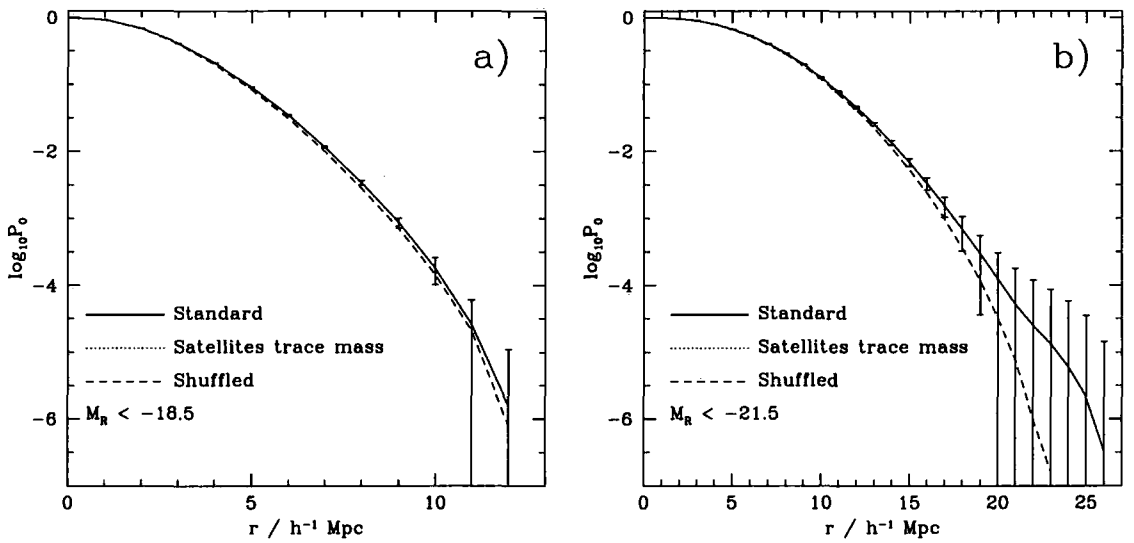

Figure 3.6: The void probability function, P_0, for a faint sample (left-hand panel) and a bright sample (right-hand panel) of galaxies. The three lines in each plot correspond to the same catalogues as the respective lines in Fig. 3.3, though in fact the dotted line overplots the solid line in both panels. The error bars are calculated using the formula of Hoyle & Vogeley (2004). Note that for clarity the horizontal axis scale is quite different in the two panels.

probability function provides little extra information.

This does not necessarily imply that the void probability function cannot provide a useful constraint on an environmentally dependent mean occupation function. If, say, the efficiency of galaxy formation is lower in haloes in underdense regions this may produce larger voids by eliminating galaxies that would otherwise form in the small haloes found in voids. The effect of shuffling on the void probability function is shown for a bright and a faint sample in Fig. 3.6. The error bars are calculated using the formula of Hoyle & Vogeley (2004), which gives the error on the mean of the void counts expected if these follow a binomial distribution, accounting for the fact that there are only a finite number of independent volumes in the simulation:

$$\sigma(P_0) = \frac{\left(P_0 - P_0^2\right)^{1/2}}{N_{\text{ind.}}^{1/2}} \quad , \tag{3.1}$$

where $N_{\text{ind.}} = 3L_{\text{box}}^3 / \left(4\pi r^3\right)$. Tinker et al. (2006a) find that compared to jackknife errors, Equation 3.1 is an overestimate at large radii and an underestimate at small radii, being similar where $P_0 \approx 0.01$.

According to these error estimates, the shuffling produces a significant effect in the void probability function (though note that as we are comparing two catalogues in the

same simulation volume we would not have to produce a shift larger than the error bars to cleanly detect the effect of shuffling), and it is in the sense expected from the above argument. Disappointingly, though, we find that the void probability function is not an especially sensitive test for this environmental dependence compared to the correlation function. The difference between shuffled and unshuffled catalogues at large scales in Fig. 3.2, for example, is clearly more statistically significant than the difference seen in Fig. 3.6. Tinker et al. (2006a) found that there was a regime where the void probability function was able to distinguish between different HODs with different prescriptions for their environmental dependence that produced the same projected correlation function. Our methodology here is not the same — we have not constrained our shuffled and unshuffled catalogues to have the same correlation function — and so the results are not directly comparable. None the less, it is probably fair to conclude that the environmental dependence produced by our models does not lie in the category of dependence that can be distinguished by the void probability function but not by the correlation function.

The line for the catalogue where satellites trace the mass but where galaxies are not shuffled between haloes overplots the line for the standard catalogue in Fig. 3.6. This is as expected, because rearranging galaxies within haloes cannot appreciable change the size of voids, and certainly cannot create or destroy large voids.

In Chapter 4 we attempt to constrain cosmology only with the correlation function. The void probability function for the SDSS is not available, and if it were, the results of Tinker et al. (2006a) suggest it would not strengthen our constraints. We note again, though, that in their methodology the mean occupation function can be freely chosen (within some parametrization) to fit the correlation function in any given cosmology. Our approach generates a *prediction* for the mean occupation function in a given cosmology, from which we can generate predictions for the correlation function, void probability function, and so on. In any case, our attempts to model the environmental dependence will concentrate on the effects on the correlation function. Environmental dependence of the mean occupation function of haloes is what drives changes in the correlation function, and therefore we examine the HOD as a function of density in the next section.

3.2.3 The halo occupation distribution

To study the environmental dependence of the halo occupation distribution, we have found the density in dark matter in an annulus between 1 and 10 h^{-1} Mpc centred on the particle with least gravitational potential energy of every halo in the simulation. These

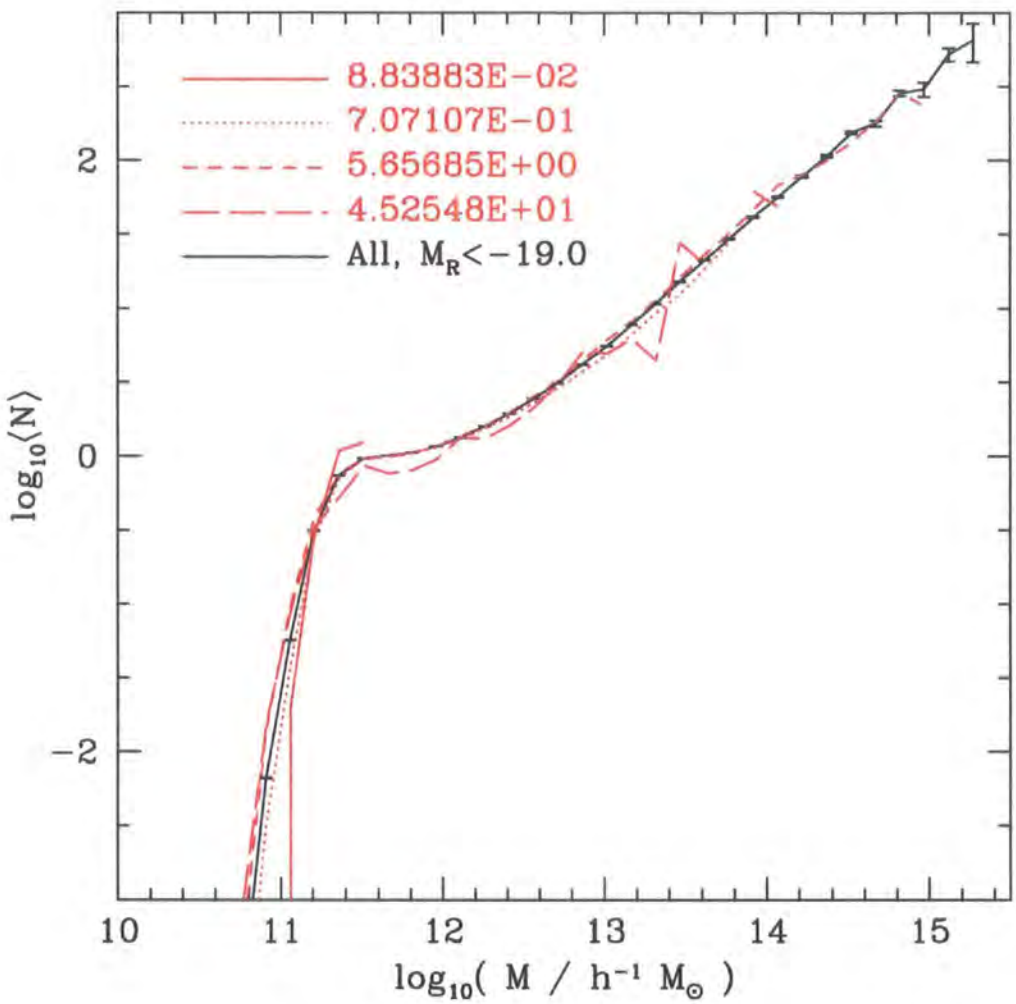

Figure 3.7: An illustration of the environmental dependence of the HOD. The black line with error bars shows the mean occupation function of galaxies with absolute magnitude $M_R < -19.0$ in our catalogues. The red lines show the mean occupation function for galaxies which lie in regions of different density. We show $\langle N(M) \rangle$ for galaxies in four different density bins, centred on the densities shown in the legend (in units of the mean density). The bins are not contiguous.

are the data used to make Figs. 2.10 and 2.11 in Chapter 2. We have binned the haloes into 12 logarithmic bins of density (in units of the mean density) and calculated the HOD separately for the haloes lying in each of these bins. An illustration of the results of this procedure is given in Fig. 3.7.

Different line styles in the figure show the mean occupation function in different density bins. The function is not defined at high mass in some density bins, simply because there are no sufficiently massive haloes in those bins. Passing over the high mass end of the

function where the data are more noisy, we see that differences between the bins persist at low mass, where the occupation function is well determined: there are a great many low mass haloes in the simulation, so even within one density bin the errors on the mean occupation function near the step in the function are small. The differences are subtle since the environmental effects are subtle, but in fact there is a visible trend. The position of the cutoff in the function, where the haloes move from having no galaxies to having one galaxy, appears to move to lower mass in the high density bins. That is, galaxy formation is suppressed in underdense regions in our model.

We have tried to quantify the size of this suppression by fitting the HOD with a function of the form suggested by Zheng et al. (2005). That is,

$$\langle N(M)\rangle = \begin{cases} \frac{1}{2}\left[1+\mathrm{erf}\left(\frac{\lg M-\lg M_{\rm min}}{\sigma_M}\right)\right] & \text{if } M \le M_0 \\ \frac{1}{2}\left[1+\mathrm{erf}\left(\frac{\lg M-\lg M_{\rm min}}{\sigma_M}\right)\right] + \left(\frac{M-M_0}{M_1}\right)^{\alpha} & \text{if } M > M_0 \end{cases} \tag{3.2}$$

where 'lg' indicates $\log_{10}$. This has the form of a step function (representing central galaxies) which is zero for $M < M_{\rm min}$ and unity for $M > M_{\rm min}$ smoothed over a width σ_M, plus a power-law (representing satellite galaxies) with slope α which cuts in for $M > M_0$. The five parameters which we fit, with a Levenberg-Marquardt algorithm (Marquardt, 1963; Press et al., 1992), are $M_{\rm min}$, σ_M, M_0, M_1 and α. We find this provides a good, stable fit for the mean occupation functions used here and in Chapter 4, without requiring the smooth cut-off in the power-law used by some authors (e.g., Kravtsov et al., 2004; Abazajian et al., 2005). It seems to be necessary to allow the power-law to cut in at $M_0 \neq M_{\rm min}$ and to smooth the cutoff in the step function with an error function to obtain good fits.

Fitting the parameters for a galaxy sample with a given threshold luminosity gives us a functional form, $N_{\rm par}(M)$, for the mean occupation function. For each bin in density, we then fit the mean occupation function for galaxies in that bin with $N_{\rm par}(qM)$, where the five parameters above remain fixed but where q is a free parameter which we find. That is, we change the mass scale of the functional form we found previously until we obtain the best fit. In general, this best fit is still rather good in a χ^2 sense, indicating that changing the mass scale this way captures the environmental dependence of the HOD reasonably well. If $q(\rho) > 1$ this corresponds to an increase in the efficiency of galaxy formation in haloes in environments of density ρ.

We show $q(\rho)$ for samples with different luminosity thresholds in Fig. 3.8. The different black lines correspond to the different thresholds, so each uses different values of the five

$\langle N(M) \rangle$ parameters listed above. For the sparser, higher luminosity samples we obtain rather noisy fits when we bin the data by density, leading to the outlying lines on the diagram. For most of the samples, however (i.e. for M_R between -18.5 and -21.0), we obtain a reasonably consistent form for q, though note that the samples are not independent since they are defined by thresholds rather than bins in luminosity. For those models which occupy a reasonably tight locus on the plot, we have calculated the mean value of q for the different luminosity thresholds, and this is shown by the red line. For $\rho \lesssim 3\bar{\rho}$ we have $q < 1$, and hence a reduced efficiency for galaxy formation compared to the average. For $3 \lesssim \rho/\bar{\rho} \lesssim 30$, $q > 1$ and increases with density. In the highest couple of density bins, q drops again. This figure is rather reminiscent of Fig. 2.11, which shows halo formation redshift as a function of local overdensity in dark matter, suggesting that our model tends to have more bright galaxies at $z = 0$ in haloes which formed earlier, according to the definition of formation redshift adopted in Chapter 2.

3.2.4 Modelling the correlation function

Measuring our scaling parameter, q, allows us to populate the simulation with a modulated HOD that incorporates environmental dependence. For each halo, we look up its mass and local density, then interpolate between points on the red line of Fig. 3.8 to find the appropriate value of q for that density. We then look up $\langle N(qM) \rangle$, where $\langle N(M) \rangle$ is the measured mean occupation function for galaxies with the luminosity threshold in use, not the parametrized version. The number of galaxies assigned to the halo is then generated from $\langle N \rangle$ by the same procedure we used for the unmodulated HOD catalogues described in Section 3.2.1. The effect of following this procedure on the resulting correlation function for galaxies with $M_R < -21.0$ is given in Fig. 3.9. The idea of modulating the local galaxy formation efficiency according to the larger-scale density field is not new; for example, it was tried by Bower et al. (1993) in the 'high peaks' model, in which the sites of galaxy formation are associated with the peaks of a suitably smoothed version of the linear density field.

The line styles Fig. 3.9 are the same as in Fig. 3.2, but we have added a magenta, dot-dashed line to show the correlation function for the catalogue generated with a modulated HOD. In a sense, the modulation has worked, reversing the suppression of the clustering amplitude seen in the shuffled catalogues or the catalogues generated using the unmodified HOD. It seems that our modulation overcompensates, however: the amplitude of clustering in the modulated catalogue is higher than for the catalogue where satellites are

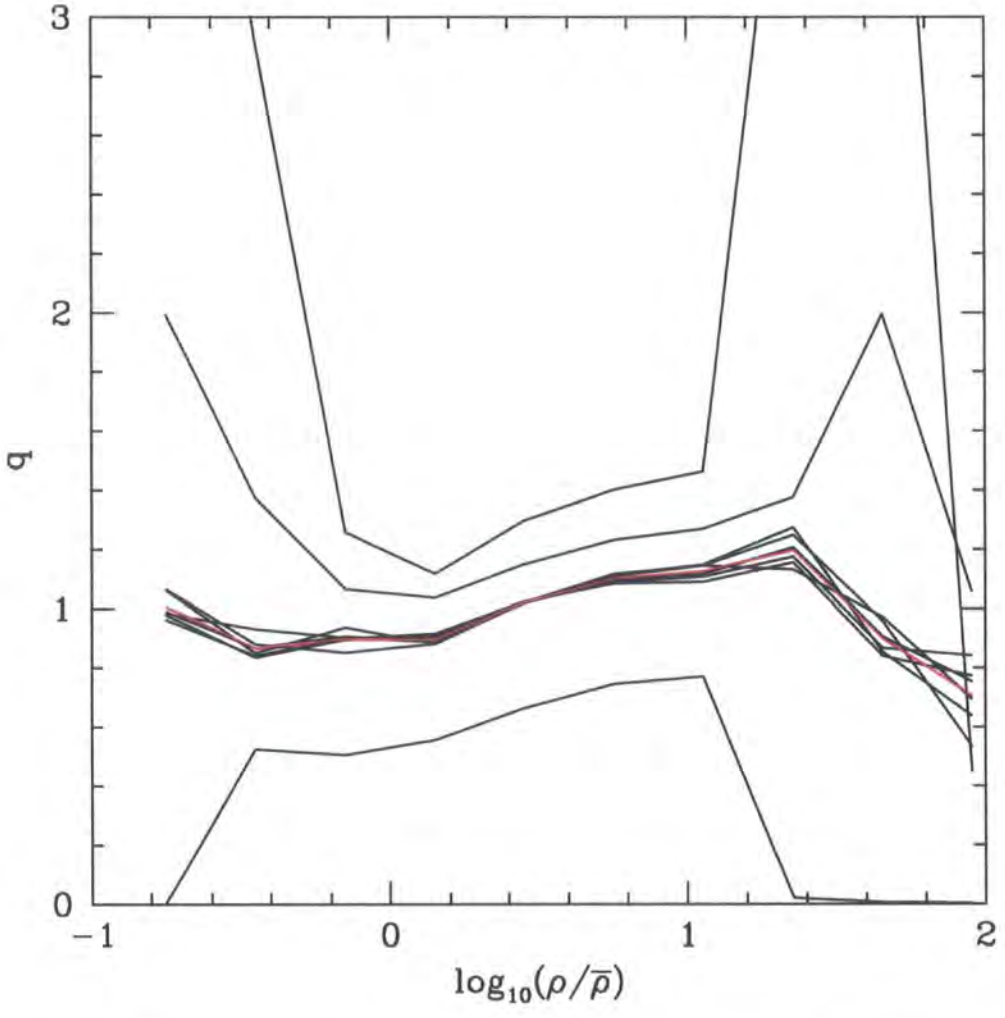

Figure 3.8: The variation of our scaling parameter, q, as a function of local density. The different black lines are for samples with different luminosity thresholds (between $M_R < -18.0$ and $M_R < -22.0$ in steps of 0.5). The three extreme lines are probably caused by low quality fits because of noise. The red line shows the average for all the samples excluding those three.

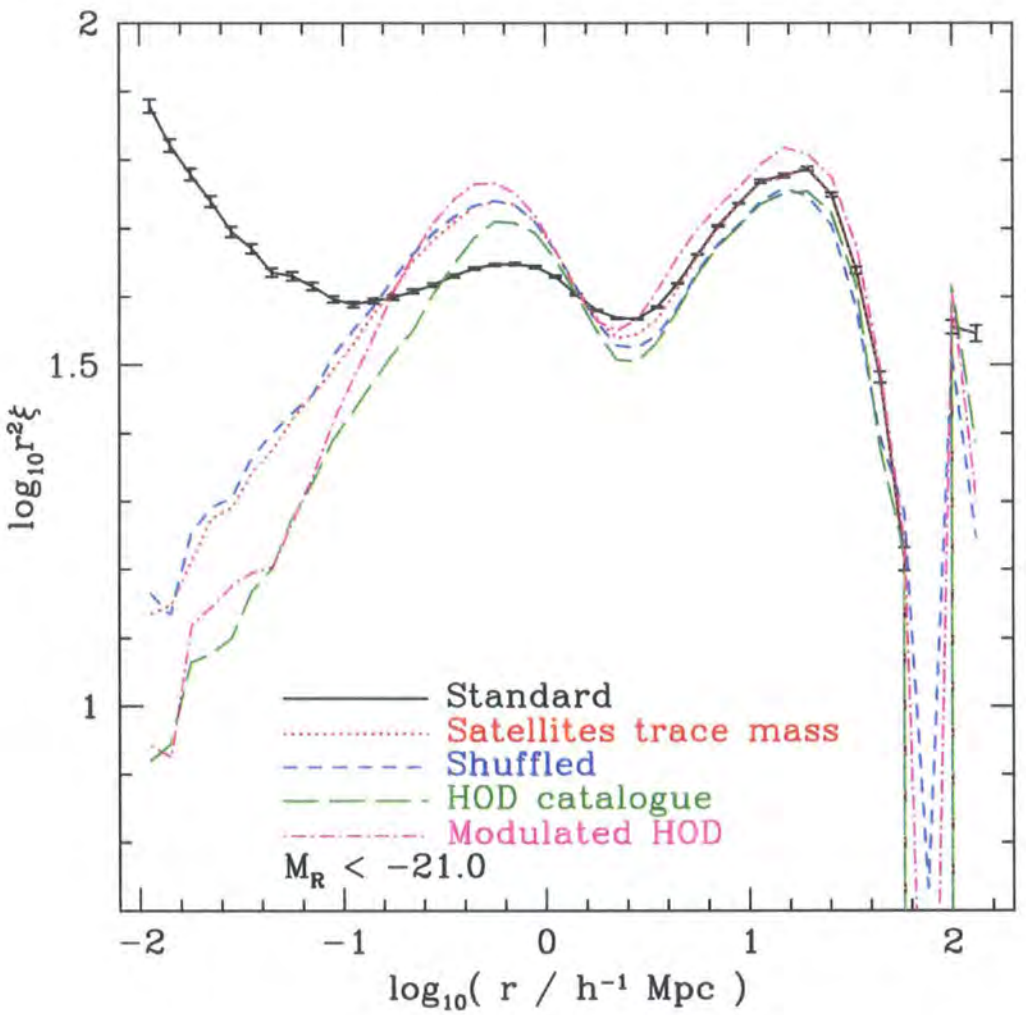

Figure 3.9: The effect on galaxy clustering of introducing a density-dependent correction to the mass scale of the HOD (see main text). This modulated HOD is given by the magenta, dot-dashed line; other lines are as in Fig. 3.2.

rearranged within haloes to trace mass, except on the smallest scales where it joins the unmodulated HOD catalogue in being less clustered than the others. The effect is very similar for other magnitude thresholds, except for those bright thresholds where the data are more noisy and the fits become less meaningful. For moderate magnitude thresholds, the effects are also very similar if we use the q value determined for that particular threshold (i.e. the corresponding black line in Fig. 3.8) rather then the average $q(\rho)$ given by the red line in Fig. 3.8. It is possible the overcompensation could come about because the changes in the mean occupation function are not fully captured by our q parameter, or because other features of the HOD, for example the scatter $P(N|\langle N\rangle)$, also change with density.

Because the shift at least has the correct sense, we have looked at the effect of applying the same procedure but with a different value of q. Fig. 3.10 is generated in the same way as Fig. 3.9, except that instead of using a mean occupation function $\langle N(qM)\rangle$ we use $\langle N(\sqrt{q}M)\rangle$. If we define $q \equiv 1 + \epsilon_q$ then for $\epsilon_q \ll 1$ this is equivalent to using $\langle N([1 + \epsilon_q/2]M)\rangle$.

The agreement on scales greater than approximately 2 h^{-1} Mpc is improved by using $\sqrt{q}$. Agreement at ~0.1–0.8 h^{-1} Mpc is also improved, though this is in the regime where the uncertainty as to how to place galaxies within haloes appears to play a more important rôle. In a narrow range of intermediate scales the agreement actually becomes slightly worse, perhaps again suggesting that there are features in the environmental dependence of the HOD not described by our simple scaling. It is quite encouraging, though, that the large-scale environmental effects — the effects of 'halo assembly bias' described by Croton et al. (2006a) (bias not being a helpful concept on small scales) — are corrected for by such a simple scheme. We show that this modulation also improves the agreement of the void probability function in Fig. 3.11. For the faint sample (Fig. 3.11a) the agreement between the original catalogue and the catalogue produced using a modulated HOD is excellent. For the bright sample (Fig. 3.11b), even this reduced modulation still overcompensates for the shuffling effects, but does improve agreement. We note that the sample used in (Fig. 3.11b) is one for which we could not obtain a good measurement of q; such a bright sample might not adhere so well to the measurement of q as a function of density given by the red line in Fig. 3.8.

The results using modulated HODs seem to suggest that a semi-analytic catalogue generated using Monte Carlo trees rather than N-body trees could be corrected given knowledge of the local density for each halo in the simulation. Given a halo of mass M,

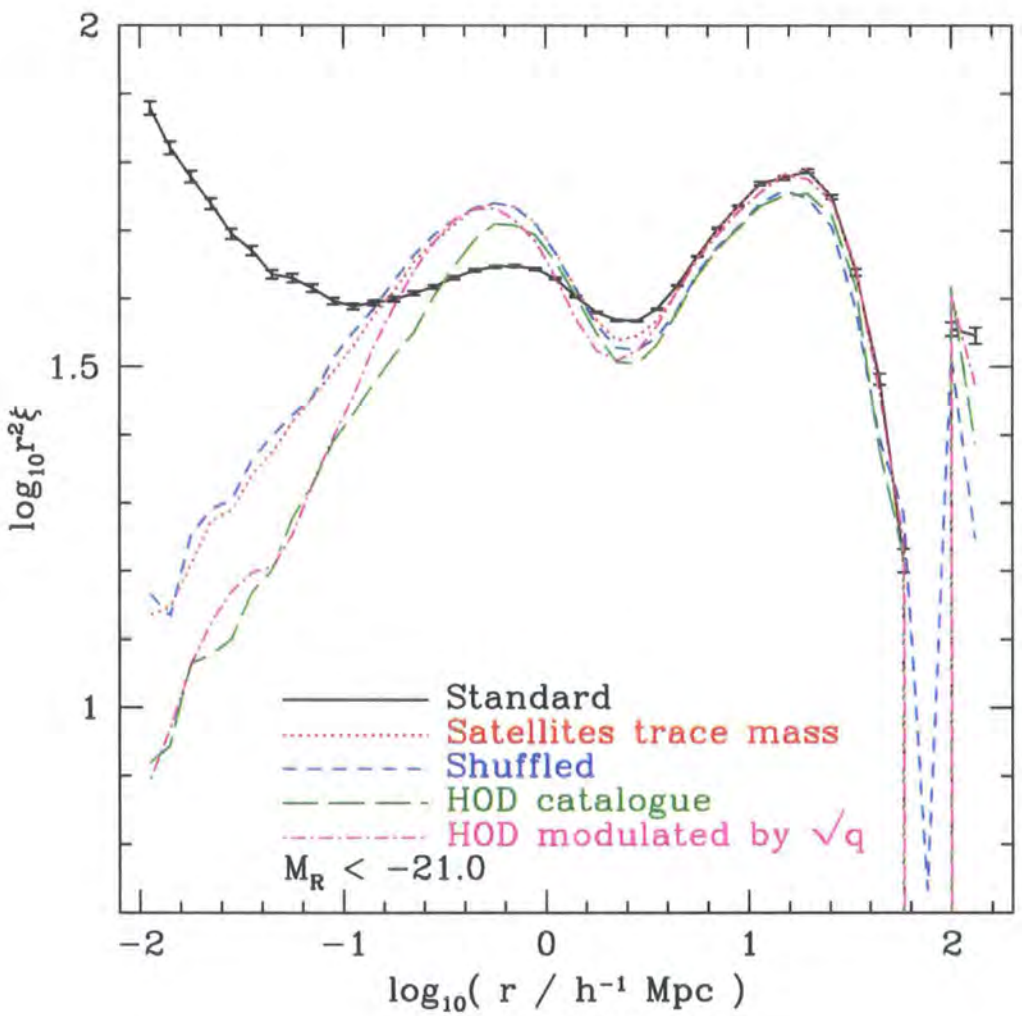

Figure 3.10: As Fig. 3.9, except that we adjust the size of the scaling parameter, q, in order to fit the correlation function more accurately on large scales.

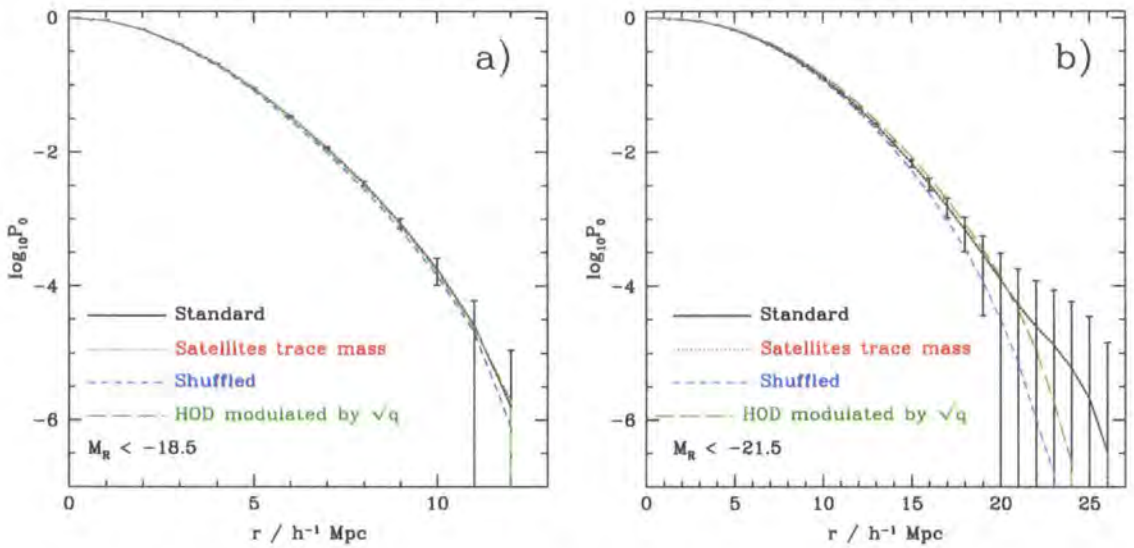

Figure 3.11: The void probability function, P_0, for a faint sample (left-hand panel) and a bright sample (right-hand panel) of galaxies. The two panels show the results for the same catalogues as Fig. 3.6, except that we show in addition the effect of populating the simulation with a HOD modulated by the square root of our scaling factor, q, as we have done for the correlation function in Fig. 3.10.

rather than assigning it a Monte Carlo merger tree generated for a halo of mass M, one could assign it a tree generated for a halo of mass $M'(M, \rho)$. In this particular scheme we would have $M'(M, \rho) = q(\rho)M$.

We do caution that, as mentioned above, different implementations of the semi-analytic model can produce different levels of halo assembly bias. Monte Carlo trees differ from N-body trees in aspects other than their environmental dependence (see, e.g., Li et al. 2005 or Chapter 2 of this thesis). The effects on the correlation function are not independent of scale, and at small to intermediate scales the placement scheme for galaxies within haloes is a more important factor. When we go on to use the correlation function predicted by a semi-analytic model using Monte Carlo trees in the next chapter, therefore, we do not routinely apply this small and uncertain correction. We do, though, attempt to estimate the impact of the uncertainties described in this chapter on the cosmological constraints we achieve.

Chapter 4

Constraining cosmology via galaxy clustering

4.1 Methods

4.1.1 Semi-analytic models

General overview

The properties of galaxies in our catalogues are generated using the semi-analytic galaxy formation code, GALFORM (Cole et al., 2000; Benson et al., 2003), mentioned in Section 3.1.1. An earlier version of the code is used for the work described in this chapter than in Chapter 3, however.

For our purposes here, we may consider a semi-analytic model as being a means of predicting, given some dark matter halo at a redshift of interest, the galaxy population of that halo. Having that information, we can construct galaxy luminosity functions, correlation functions, etc. that might be considered the results or predictions of the model.

The first step in predicting the galaxy population of a halo is calculating the merger history of the halo. In the Millennium Simulation, used in Chapter 3, this could be extracted from the N-body data. The simulations we will describe below, by contrast, do not have sufficient resolution for us to extract reliable merger trees for the haloes of interest. A Monte Carlo scheme based on the work of Lacey & Cole (1993) is used instead, therefore. This generates a merger tree for a halo based only on the halo mass, the cosmology and the initial power spectrum, and does not use other data from the simulation.

Given the merger history of a halo, the model computes the evolution of the baryonic content of the halo using a variety of analytic prescriptions, which we now describe briefly. First, it is assumed that every dark matter halo comes with enough baryons to match the cosmic baryon fraction. If a halo is not undergoing mergers, or is just slowly accreting small lumps of material (which is of course also accounted for in the merger

trees), the cooling time of the halo's quota of gas is estimated analytically (assuming spherical symmetry) to provide an estimate of the amount of cold gas available to form stars in the galaxy at the centre of the halo. Assumptions about the angular momentum distribution of haloes also allow an estimate of the size of the disc produced in this mode of star formation.

If two haloes merge, then their galaxies may also merge. When running GALFORM tied to a particular N-body simulation, for example the Millennium Simulation, we can explicitly track the orbits of the particles associated with a galaxy to determine when it might merge with another galaxy. Otherwise, the timescale for merging is estimated by consideration of dynamical friction. In fact, this analytical estimate is sometimes also necessary in the N-body mode, since subhaloes hosting galaxies may be destroyed near the centre of larger haloes, removing our ability to track the associated galaxy. Galaxy-galaxy mergers may induce bursts of star formation (with perhaps a different initial stellar mass function from quiescent star formation), and in this model they also trigger the formation of spheroids.

Once star formation has occurred, supernovae are able to inject energy into the interstellar medium, heating the gas and suppressing further star formation. They also enrich the interstellar medium with metals, in turn affecting the cooling rate of the gas and the properties of any stars which subsequently form from it. The stellar populations and the evolution of their properties are accounted for by the model. To synthesize observed properties of the galaxies, such as their spectra or broad band luminosities, GALFORM also models dust extinction and the generation of emission lines. The extinction depends on the inclination of the galaxy to the line of sight, which is assigned randomly.

Many of the equations governing the physical processes modelled by GALFORM contain parameters which may be adjusted. Some of these have a 'natural' value determined by the physics; others are derived by comparison to more detailed simulations. The function of allowing these parameters to change, then, is to allow investigation into the magnitude of the effect of different physical processes on the resulting galaxy properties in the model. Other parameters have no natural value, and can only be fixed by requiring they take values which allow the model to fit observations. Much of the time, if we are able to fit some set of observations satisfactorily by choosing the parameters of the model judiciously, the same set of observations could also be fit reasonably well by some very different choice of parameters. Therefore, within the GALFORM framework, we have different models using different physics which are equally good at matching the observations (though this may

not, of course, be the case if we were to choose a different set of observations to constrain the model).

Our three models

Our aim here is to try to constrain cosmological parameters by comparing clustering statistics from a simulation populated with semi-analytic galaxies to the corresponding measurements in an observational survey. We would hope that our constraints are robust, in the sense of being insensitive to the precise semi-analytic model used, and we would like to test whether this is the case. Therefore, although we use only one code, GALFORM, we use three different 'models', in the sense of different combinations of the physics we attempt to model and the parameters governing that physics. The three models are as follows:

- The fiducial model of Cole et al. (2000). This is successful in matching several sets of observations, including the B- and K-band luminosity functions, galaxy colours and mass-to-light ratios for galaxies of different morphologies, the cold gas mass in galaxies, galaxy disc sizes and the slope and scatter of the I-band Tully-Fisher (1977) relation. Unfortunately, though, it assumes a cosmic baryon fraction, $\Omega_{\rm b}$, of only 0.02. This is inconsistent with recent estimates from Big Bang nucleosynthesis (e.g., O'Meara et al., 2001) and the cosmic microwave background (Spergel et al., 2006). Nevertheless, we feel it is worthwhile to include this model in our analysis as a well recognized and well understood model that has been thoroughly described and studied. In our figures, lines corresponding to output from this model are given the label 'Cole2000'.

- A model similar to the first, but with $\Omega_{\rm b} = 0.04$, which is closer to current estimates. Since there are twice as many baryons as in the first model, if we leave the rest of the parameters unchanged then, as expected, the model is unable to match observations such as the luminosity function. Therefore we introduce a new physical process: thermal conduction in massive haloes (this is analysed in greater detail by Benson et al. 2003). We simply assume that gas is unable to cool if the halo circular velocity, $V_{\rm circ}$, satisfies

$$V_{\rm circ} > V_{\rm cond}\sqrt{1+z} \quad , \tag{4.1}$$

where $V_{\rm cond}$ is a parameter we may adjust. This suppresses the problematic bright end of the luminosity function; the effect is similar, in fact, to more recent and

more physically motivated implementations of feedback from active galactic nuclei in GALFORM (Bower et al., 2006). Though it is clearly rather crude, note that our objective here is only to produce a realistic enough galaxy catalogue to compare to observations. We are trying to mimic the effect of whatever physical process suppresses the bright end of the luminosity function, without having to adopt a complicated parametrization that is no better physically motivated than a more simple and understandable one. The label we give to this model in our figures is 'C2000hib' (where 'hib' stands for 'high baryon fraction').

- A model incorporating 'superwinds'. In this model it is postulated that a galaxy's cold gas is heated strongly enough for it to be expelled completely from the halo, rather than returning to the reservoir of hot gas associated with the halo. In fact, the model is derived from that used by Baugh et al. (2005) to reproduce the abundance of faint galaxies detected at submillimetre wavelengths. This also incorporates the additions and refinements to GALFORM described by Benson et al. (2003). These include a modification to the assumed profile of the halo gas, a more sophisticated treatment of conduction, and a more detailed treatment of galaxy mergers, in particular the effects of tidal stripping and dynamical friction (Benson et al., 2002). They also include a simple model of the effect of reionization on small haloes, where cooling is prevented if $V_{\rm circ} < V_{\rm cut}$ and $z < z_{\rm cut}$ for two parameters $V_{\rm cut}$ and $z_{\rm cut}$. The strength of superwind feedback is parametrized by $V_{\rm sw}$, the characteristic velocity of the wind. The model is denoted 'Model M' in our figures.

We wish to run each of these models in many different cosmologies, in order to generate galaxy catalogues in which the N-body component and the semi-analytic component are consistent. Changing cosmology naturally changes the galaxy population predicted by each model, however, so that even if we fix the parameters such that the galaxies match observational constraints in one fiducial cosmology, they are unlikely to match in other cosmologies. We therefore tweak the parameters between different cosmologies to try to match the data. It is not possible to do this for the full range of even the primary constraints described by Cole et al. (2000). We restrict ourselves to a comparison with the ${}^{0.1}r$-band SDSS luminosity function of Blanton et al. (2003b) at $z = 0.1$ (for a description of what is meant by the ${}^{0.1}r$-band, see Blanton et al. 2003a). Even then, to make the problem tractable and to ensure our three models remain distinct, we restrict the parameters we allow ourselves to adjust to try to match the luminosity function. The

parameters we allow to vary are:

- $V_{\rm sw}$, for Model M only.
- $V_{\rm cond}$, for the C2000hib model only.
- $V_{\rm cut}$, one of the parameters controlling reionization. Though we experimented with changing this for all the models, all the ones used below have either $V_{\rm cut} = 0$ (Cole2000 and C2000hib) or $V_{\rm cut} = 60$ (Model M). As well as being simpler, this also helps make Model M more distinct from the other two.
- $V_{\rm hot}$ and $\alpha_{\rm hot}$. These are closely linked but we vary them independently. They control the strength of standard (i.e. not superwind) supernova feedback in the following way. The rate of change of the mass of hot gas and of cool gas in a halo are linked with the instantaneous star formation rate, ψ, by:

$$\dot{M}_{\rm hot} = -\dot{M}_{\rm cool} + \beta\psi \tag{4.2}$$

(Cole et al. (2000), equation 4.7). β is related to the circular velocity of the galaxy disc, $V_{\rm disc}$, by

$$\beta = (V_{\rm disc}/V_{\rm hot})^{-\alpha_{\rm hot}} \tag{4.3}$$

(Cole et al. (2000), equation 4.15).

Some of the cosmologies listed below require quite extreme, perhaps unphysical, parameter values. In some cases, GALFORM is reluctant to run, while in others the fit for some observations is compromised in an attempt to fit the ${}^{0.1}r$-band luminosity function well. In addition to running each model with tweaked parameters in each cosmology, therefore, we also run each model in each cosmology using the same parameters as the run with $\Omega_{\rm m} = 0.3$ and $\sigma_8 = 0.8$ (the central cosmology of simulation Run 1; see below).

We are not able to produce a good fit to the luminosity function in a χ^2 sense, even allowing these parameters to vary. This may be a concern when comparing to observational data. Volume-limited galaxy samples, to which we wish to compare our results later, are chosen such that all the galaxies are brighter than some given magnitude limit. If we choose a sample of semi-analytic galaxies with the same magnitude limit, then because our luminosity function is wrong we may not be choosing a sample that necessarily corresponds to the observational one, even within our model. Therefore we instead select semi-analytic galaxy samples with a magnitude such that the sample has the same space density as the corresponding observational sample. This means that when we adjust the

parameters of the model to match the luminosity function, it is more important for our purposes to match its overall *shape* rather than its magnitude normalization.

The Υ parameter of Cole et al. (2000) is related to this sort of scaling of the luminosity function. It was introduced to account for brown dwarfs, which absorb some of the mass of gas assumed to be tied up in stars, but without producing light. It is defined by

$$\Upsilon = \frac{\text{mass in visible stars + mass in brown dwarfs}}{\text{mass in visible stars}} \tag{4.4}$$

(Cole et al. 2000, equation 5.2). Clearly, then, we must have $\Upsilon \geq 1$ given this physical explanation. The result of including this effect is to scale luminosities by a factor $1/\Upsilon$. For each GALFORM model we run, we compare the resulting ${}^{0.1}r$-band luminosity function with the observational value from the SDSS (in fact, we compare only one point near the characteristic luminosity, L_*). We express the difference between the two in terms of the Υ parameter: the (reciprocal of the) amount by which we would have to scale the luminosity of the semi-analytic galaxies to match the data. Sometimes this requires $\Upsilon < 1$. Therefore, when we give a value of Υ below, it should be treated only as an indication of the amount by which we would have to scale luminosities so that when we select a galaxy sample by a number density threshold then it would have the same luminosity threshold as the observational sample. Note that we calculate Υ by reference to a specific point on the SDSS ${}^{0.1}r$-band luminosity function. Its exact value would change if we normalized at a different point (since the model luminosity function is not the same shape as the observational one), or in a different band (since the colour of model galaxies may be incorrect).

Once we have given ourselves the freedom to scale the luminosity function in this way, then, the effect of varying the parameters we allow ourselves to change to try to match the shape of the luminosity function is as follows:

- Increasing $V_{\rm SW}$, or decreasing $V_{\rm cond}$, tends to steepen the bright-end slope, i.e. give fewer very bright galaxies. $V_{\rm SW}$ is only non-zero for Model M; $V_{\rm cond}$ is only finite for the C2000hib model.

- Increasing $V_{\rm cut}$ reduces the slope at the faint end, reducing the number of the faintest of the galaxies we study.

- Increasing $V_{\rm hot}$ tends to suppress the overall space density of galaxies. Because of the effect of other parameters, it is most useful for adjusting the abundance of galaxies of around L_* or a little fainter.

- Changes in $\alpha_{\rm hot}$ can be viewed as modulating the effect of changing $V_{\rm hot}$. Visually, for typical values of $V_{\rm hot}$, increasing $\alpha_{\rm hot}$ flattens the faint-end slope, typically over a wider range of luminosities than $V_{\rm cut}$.

We usually find that to make the bright-end slope steeper and to make the faint-end slope shallower, as required by the data, needs all parameters tweaked to give larger amounts of feedback. This tends to have the overall effect of reducing the predicted luminosities, leading to $\Upsilon < 1$ as mentioned above. Requiring $\Upsilon \geq 1$ would therefore require us to compromise one component or the other of the shape in these models. Since we later rescale to match space densities anyway, we opt not to make this compromise. Given two parameter combinations which both match the luminosity function reasonably well and which both give $\Upsilon < 1$, we use the Υ parameter as a tie-breaker, selecting the combination which gives Υ closer to unity. We have also checked that each model is at least qualitatively consistent with the other primary GALFORM constraints (the Tully-Fisher relation, disc sizes, morphological mix, metallicities and gas fractions — see Cole et al. 2000).

The r-band luminosity function for each of our models in our fiducial cosmology ($\Omega_{\rm m} = 0.3$ and $\sigma_8 = 0.8$) is shown in Figure 4.1. Red corresponds to the Cole2000 model, blue to the C2000hib model, and green to Model M. The black line shows the SDSS r-band luminosity function of Blanton et al. (2003b); we have converted from the ${}^{0.1}r$-band to the r-band for this plot. Each model luminosity function is scaled to agree with the data at one point, and the scaling factor is given in the legend. Qualitatively, the agreement between the models and the data is reasonable. The very sharp cutoff at the bright end of the luminosity function in Model M is a generic feature of the model. The lower space density of very faint galaxies in this model is also generic, and comes from the introduction of reionization (non-zero $V_{\rm cut}$). At first glance, it appears that the Cole2000 model gives better agreement with the data at the bright end than the C2000hib model, despite the inclusion of a feedback mechanism specifically to solve this problem in the latter. Recall, though, that the Cole2000 model has a lower baryon fraction, and that despite this we have to introduce relatively high levels of supernova feedback to match the shape of the luminosity function. We therefore need $\Upsilon \sim 0.5$ to recover the correct luminosities, while the C2000hib model needs a much more physically palatable $\Upsilon \sim 1.2$. It may appear that our requirement for $\Upsilon = 0.5$ is inconsistent with the original Cole et al. (2000) paper, the reference model of which requires $\Upsilon = 1.38$. It is not inconsistent, for a few reasons. Firstly, we use the label 'Cole2000' for our model because it uses an

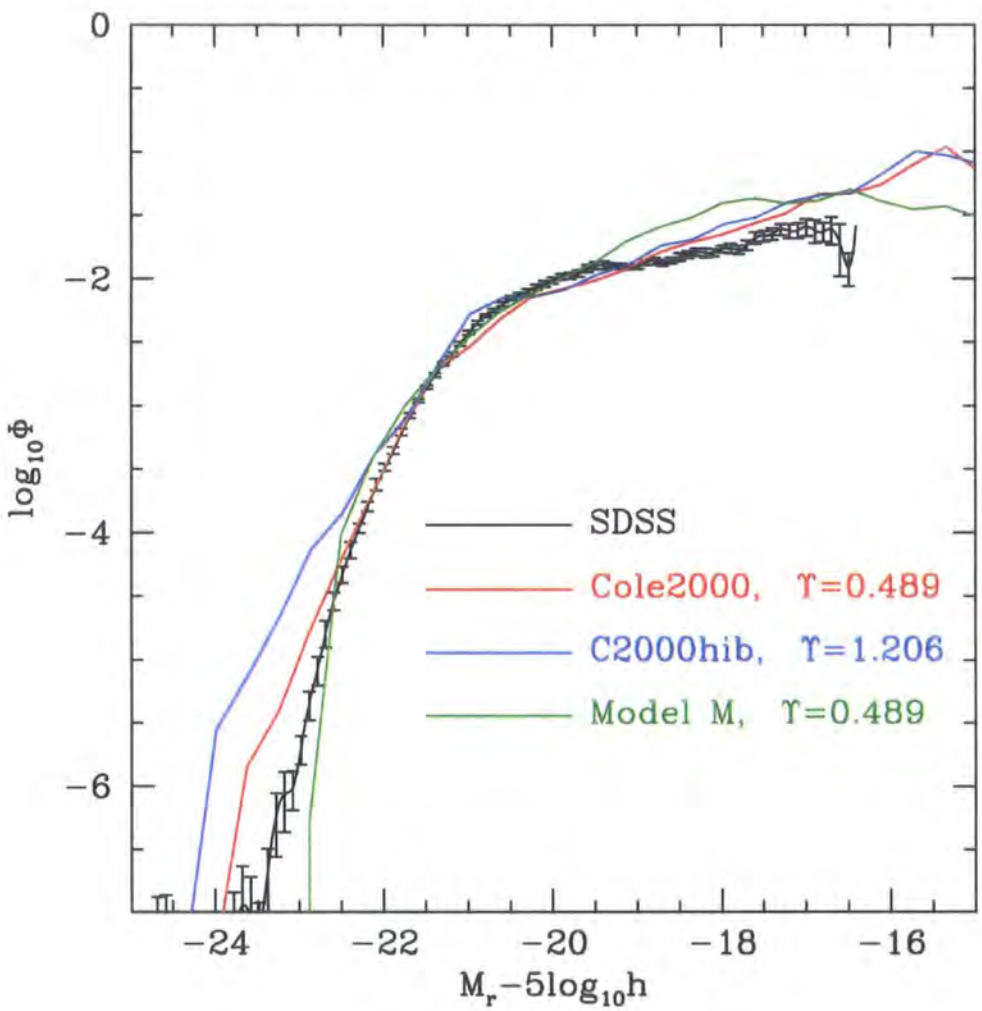

Figure 4.1: r-band luminosity functions for the three fiducial GALFORM models, compared to the SDSS luminosity function of Blanton et al. (2003b). The value of the scaling parameter Υ, required to normalize the model luminosities for galaxies of a particular space density in this band, is also given in the legend. Errors on the SDSS luminosity function are only given for every tenth point, for clarity.

equivalent code with the same physics governed by the same parameters as the models of Cole et al. (2000). As we have just noted, however, some of the parameters take different values in our fiducial model in order to try to match the shape of the r-band luminosity function. Secondly, while the reference model of Cole et al. (2000) had $\sigma_8 = 0.93$, ours has $\sigma_8 = 0.8$. Thirdly, their Υ was calculated by reference to the value of the observed b_J-band luminosity function at L_* (though in fact the same correction also provided a good match to the K-band luminosity function). Ours is calculated by reference to the r-band luminosity function. We match to a point slightly brighter than L_* (where the exponential cutoff has started to bite more deeply and the galaxies are less abundant; this point at $M_r \sim -21.5$ can be seen quite easily in Fig. 4.1 as being where all the lines cross) since we otherwise had problems calculating Υ for some of our models with a very shallow faint-end slope and low galaxy number density.

4.1.2 Simulations

We ran two simulations using the same code as was used for the Millennium Simulation: GADGET2. In each case we have stored the output at several redshifts. These are chosen so that by applying the relabelling procedure described in Appendix A, we have a grid of cosmologies evenly spaced in steps of 0.05 in σ_8 for each of three redshifts: 0, 0.05 and 0.1. We have chosen the simulation parameters so that the first simulation, 'Run 1', has $\Omega_{\rm m} = 0.3$ at its $\sigma_8 = 0.8$ output, while the second simulation, 'Run 2', has $\Omega_{\rm m} = 0.3$ at its $\sigma_8 = 0.9$ output. When we perform a further rescaling of $\Omega_{\rm m}$ (see below) it is these central outputs which remain unchanged. The initial conditions are calculated using a Bardeen et al. (1986) power spectrum with shape parameter $\Gamma = 0.14$. A smooth power spectrum was most convenient in the light of the rescalings we carry out on the final output, but in fact the Bardeen et al. (1986) power spectrum with $\Gamma = 0.14$ was found to be a good fit to the CMBFAST (Seljak & Zaldarriaga, 1996) spectrum with $\Omega_{\rm b} = 0.045$ used for the Millennium Simulation. The cosmological parameters associated with each snapshot when considered as a $z = 0$ output, as a $z = 0.05$ output and as a $z = 0.1$ output are given in Table 4.1 for Run 1 and in Table 4.2 for Run 2. The cosmological parameters of the outputs for our $z = 0.1$ grid are also shown in Fig. 4.2. This figure also shows schematically the rescalings in $\Omega_{\rm m}$ we carry out so that instead of the cosmologies lying on a curve dictated by the evolution of $\Omega_{\rm m}$ and σ_8 in a given simulation they lie on a curve $\sigma_8 \Omega_{\rm m}^{0.5} = $ const. — 'cluster normalization' in other words. Note that for some values of $(\Omega_{\rm m}, \sigma_8)$ on the cluster normalized curves, we have rescaled an output from each of Run 1

Table 4.1: Outputs from Run 1, with central output Ω_m=0.3, σ_8=0.8. Column 1 gives the label of the output, and column 2 gives the redshift of the output before rescaling. Columns 3 and 4 give the matter density and amplitude of clustering in this output, which are the cosmological parameters when the output is relabelled as a $z = 0$ output. The output 22 line gives the input cosmological parameters for the simulation code. Columns 5–8 show the final parameter values if the output is relabelled to the redshift given in the column header. Values of σ_8 highlighted in bold show that for each chosen redshift we can reconstruct a grid of models evenly spaced in σ_8.

Simulation output				For $z = 0.05$ grid		For $z = 0.1$ grid	
Label	z	Ω_m	σ_8	Ω_m	σ_8	Ω_m	σ_8
22	0.00000	0.10000	0.95176	0.08758	0.96404	0.07705	0.97503
21	0.00677	0.10183	**0.95000**	0.08921	0.96239	0.07850	0.97348
20	0.05713	0.11603	0.93679	0.10184	**0.94999**	0.08977	0.96182
19	0.10742	0.13112	0.92354	0.11532	0.93744	0.10183	**0.95001**
18	0.19492	0.15936	**0.90000**	0.14072	0.91536	0.12467	0.92908
17	0.25463	0.17995	0.88388	0.15935	**0.90001**	0.14153	0.91467
16	0.31441	0.20148	0.86773	0.17896	0.88464	0.15936	**0.90000**
15	0.38019	0.22608	**0.85000**	0.20150	0.86772	0.17998	0.88386
14	0.44916	0.25270	0.83151	0.22607	**0.85001**	0.20259	0.86692
13	0.51821	0.27996	0.81316	0.25143	0.83237	0.22608	**0.85000**
12	0.56826	0.30000	**0.80000**	0.27018	0.81968	0.24356	0.83778
11	0.64673	0.33162	0.77966	0.30001	**0.79999**	0.27155	0.81877
10	0.72511	0.36324	0.75972	0.33010	0.78062	0.30000	**0.80000**
9	0.76404	0.37885	**0.74999**	0.34507	0.77114	0.31425	0.79078
8	0.85223	0.41386	0.72837	0.37885	**0.74999**	0.34661	0.77017
7	0.94043	0.44806	0.70739	0.41220	0.72939	0.37885	**0.75000**
6	0.97227	0.46017	**0.70000**	0.42408	0.72209	0.39041	0.74283
5	1.07090	0.49668	0.67761	0.46017	**0.70000**	0.42575	0.72107
4	1.16952	0.53153	0.65610	0.49498	0.67866	0.46018	**0.69999**
3	1.19825	0.54134	**0.65000**	0.50485	0.67259	0.46999	0.69398
2	1.30816	0.57741	0.62736	0.54135	**0.65000**	0.50655	0.67154
1	1.41808	0.61104	0.60581	0.57574	0.62842	0.54135	**0.65000**

Table 4.2: Outputs from Run 2, with central output Ω_m=0.3, σ_8=0.9. Columns are as for Table 4.1

Simulation output				For $z = 0.05$ grid		For $z = 0.1$ grid	
Label	z	Ω_m	σ_8	Ω_m	σ_8	Ω_m	σ_8
28	0.00000	0.10000	1.07073	0.08758	1.08455	0.07705	1.09691
27	0.07020	0.11987	**1.05000**	0.10527	1.06509	0.09283	1.07862
26	0.12371	0.13619	1.03409	0.11987	**1.05001**	0.10591	1.06441
25	0.17721	0.15345	1.01793	0.13539	1.03486	0.11986	**1.05001**
24	0.23611	0.17346	**1.00000**	0.15346	1.01792	0.13620	1.03408
23	0.29792	0.19545	0.98121	0.17346	**1.00000**	0.15435	1.01711
22	0.35972	0.21834	0.96245	0.19439	0.98211	0.17346	**1.00000**
21	0.40082	0.23397	**0.95001**	0.20876	0.97021	0.18664	0.98864
20	0.47092	0.26124	0.92892	0.23399	**0.94999**	0.20991	0.96928
19	0.54093	0.28904	0.90807	0.25991	0.92993	0.23397	**0.95000**
18	0.56823	0.29998	**0.90001**	0.27017	0.92215	0.24355	0.94251
17	0.64673	0.33162	0.87711	0.30001	**0.89999**	0.27155	0.92111
16	0.72514	0.36325	0.85469	0.33011	0.87819	0.30001	**0.89999**
15	0.74174	0.36992	**0.85000**	0.33650	0.87363	0.30608	0.89556
14	0.82884	0.40464	0.82580	0.36992	**0.84999**	0.33803	0.87254
13	0.91595	0.43866	0.80229	0.40300	0.82693	0.36993	**0.84999**
12	0.92455	0.44197	**0.80001**	0.40624	0.82469	0.37307	0.84779
11	1.02085	0.47835	0.77497	0.44200	**0.79999**	0.40791	0.82353
10	1.11706	0.51321	0.75086	0.47664	0.77615	0.44199	**0.80000**
9	1.12056	0.51445	**0.75001**	0.47787	0.77530	0.44322	0.79915
8	1.22656	0.55086	0.72458	0.51444	**0.75001**	0.47957	0.77413
7	1.33267	0.58512	0.70027	0.54920	0.72574	0.51447	**0.74999**
6	1.33387	0.58549	**0.70001**	0.54958	0.72547	0.51485	0.74973
5	1.45057	0.62052	0.67460	0.58549	**0.70000**	0.55127	0.72429
4	1.56728	0.65279	0.65055	0.61891	0.67578	0.58550	**0.70000**
3	1.56998	0.65350	**0.65000**	0.61966	0.67523	0.58626	0.69945
2	1.69849	0.68586	0.62504	0.65350	**0.65000**	0.62126	0.67406
1	1.82699	0.71513	0.60156	0.68440	0.62619	0.65351	**0.65000**

and Run 2. This was to check that our rescaling technique was consistent, and indeed we find that our results are unchanged when we decide to use the rescaled output from Run 1 or from Run 2 for any given cosmology on the cluster normalized curve. None the less, the similar shape of the cluster normalization curve and the simulation evolution curve means that for our carefully chosen simulation parameters we never have to make a big rescaling. For the remainder of our results, we always choose which simulation from which to take an output so as to minimize the size of the rescaling of $\Omega_{\rm m}$. Note that the other reason for choosing cosmologies along this curve was to test if, by distinguishing between cosmologies on this curve, we could break degeneracies found in attempts to constrain cosmological parameters through, e.g., weak lensing analyses. Munshi & Kilbinger (2006), for example, find that cosmic shear surveys constrain the combination $\sigma_8\Omega_{\rm m}^{0.48}$ for flat ΛCDM when marginalising over the spectral index and shape parameter.

At the suggestion of David Weinberg of Ohio State University, who helped to initiate and plan some aspects of this project, we have named the simulations the 'DOH' simulations (Durham-OHio). Since the two simulations for which we have tabulated the outputs have 512^3 particles, we have denoted them the 'doh512' simulations. We ran a simulation with 256^3 particles as a precursor to these, as a test that the resolution was sufficient for our purposes and to test our rescaling algorithms. This is denoted the 'doh256' simulation, and has parameters chosen such that it has an output at $(\Omega_{\rm m}, \sigma_8) = (0.3, 0.8)$. Its resolution is similar to the doh512 simulations, but it is in a smaller, 153.6 h^{-1} Mpc box compared to the 300 h^{-1} Mpc of our larger simulations. All results below are for the doh512 simulations unless explicitly stated.

We populate the simulations in a similar way to the shuffled catalogues described in Chapter 3. That is, to each halo in the simulation we assign a semi-analytic galaxy population for a random tree of the same mass. We then place the central galaxy at the position of the particle with least gravitational potential energy, and place the satellite galaxies on random particles within the halo. Note, however, that the resolution of the DOH simulations is inferior to the resolution of the Millennium Simulation. This makes it possible for the model to predict that a halo in the DOH simulation contains a galaxy even though it is not resolved with at least 20 particles, which is our normal criterion for considering the halo to be resolved. To take account of these galaxies, we calculate the number of such haloes expected for the simulation volume for the Jenkins et al. (2001) mass function. We then take the galaxy populations predicted by GALFORM for these haloes and place the galaxies on random particles in the simulation which are not in

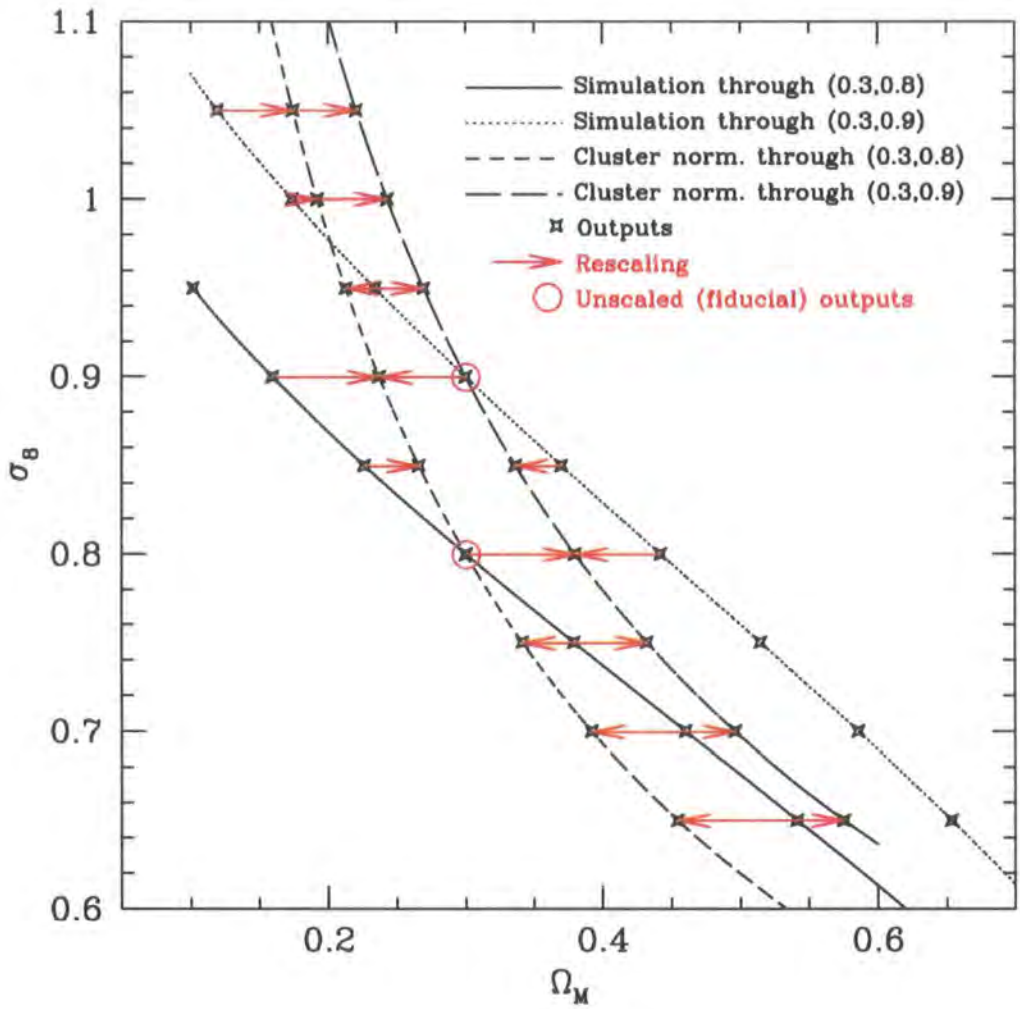

Figure 4.2: The position in the (Ω_m, σ_8) plane of the outputs of the two doh512 simulations. The line connecting the outputs shows how the values of Ω_m and σ_8 change as the simulation evolves, where we track the instantaneous values of these parameters rather than the values they will have at the final time, which would be the more conventional labelling (and would, of course, not change during the course of the simulation). The solid line corresponds to Run 1 and the dotted line corresponds to Run 2. Low redshift outputs (lower density, more clustered) are in the top left, while high redshift outputs (higher density, less clustered) are in the bottom right. Also shown are the curves described by the cluster normalization condition that $\sigma_8 \Omega_m^{0.5} = \text{const.}$ for two different values of this constant. We rescale simulation outputs so that they lie on these curves. The rescaling is shown schematically by the red arrows.

haloes. We do not expect this to have a significant effect on clustering statistics, since almost all galaxies which would be placed in unresolved haloes are very faint, and in any case the halo bias as a function of mass is not a strong function of mass in this regime (Cole & Kaiser, 1989; Mo et al., 1999) so that we do not lose too much accuracy by placing galaxies in haloes of the wrong mass. None the less, we have checked that employing this scheme has only a small effect on our measured correlation functions, the results being given in Figs. 4.3 and 4.4. These show that changing the minimum resolved mass from 20 particles to 50 particles has only a very small effect on the correlation function, as does ignoring the 'unresolved' galaxies entirely, even for a conservative mass limit of 50 particles. Moreover, both these tests were conducted on a rather faint sample of galaxies since this provides the most stringent resolution test. When we compare to SDSS data, the magnitude limit will be somewhat brighter and so we expect the unresolved haloes to have an even smaller effect.

So, summarizing the data to which we intend to apply our clustering analysis, we have two N-body simulations, from each of which we extract nine outputs. Each output is relabelled (and rescaled, if necessary) to represent a $z = 0.1$ cosmology lying on a cluster normalization curve, these cosmologies being selected to give a regular grid in σ_8. For each of these outputs we run three variants of our semi-analytic model, using cosmological parameters consistent with the simulation. Each of these variants comes in two versions: a version in which we adjust the semi-analytic parameters to try to match the shape of the observed ${}^{0.1}r$-band luminosity function, and a version in which we use the same parameters as the model calibrated in the $(\Omega_{\rm m}, \sigma_8) = (0.3, 0.8)$ cosmology. This gives us $2 \times 9 \times 3 \times 2 = 108$ different semi-analytic catalogues, in which each galaxy is assigned a position within a 300 h^{-1} Mpc box.

4.2 Results

4.2.1 Sample definition

In their study of the luminosity and colour dependence of the galaxy correlation function using the main galaxy sample of the SDSS, Zehavi et al. (2005) calculated the projected two-point correlation function for ten different galaxy samples defined by thresholds in absolute magnitude. The faintest threshold is given by $M_r^{\rm max} = -18.0$ and the brightest by $M_r^{\rm max} = -22.0$, the others being regularly spaced between these values in steps of 0.5 magnitudes (there are two $M_r^{\rm max} = -20.0$ samples, one of which is cut in redshift to excise

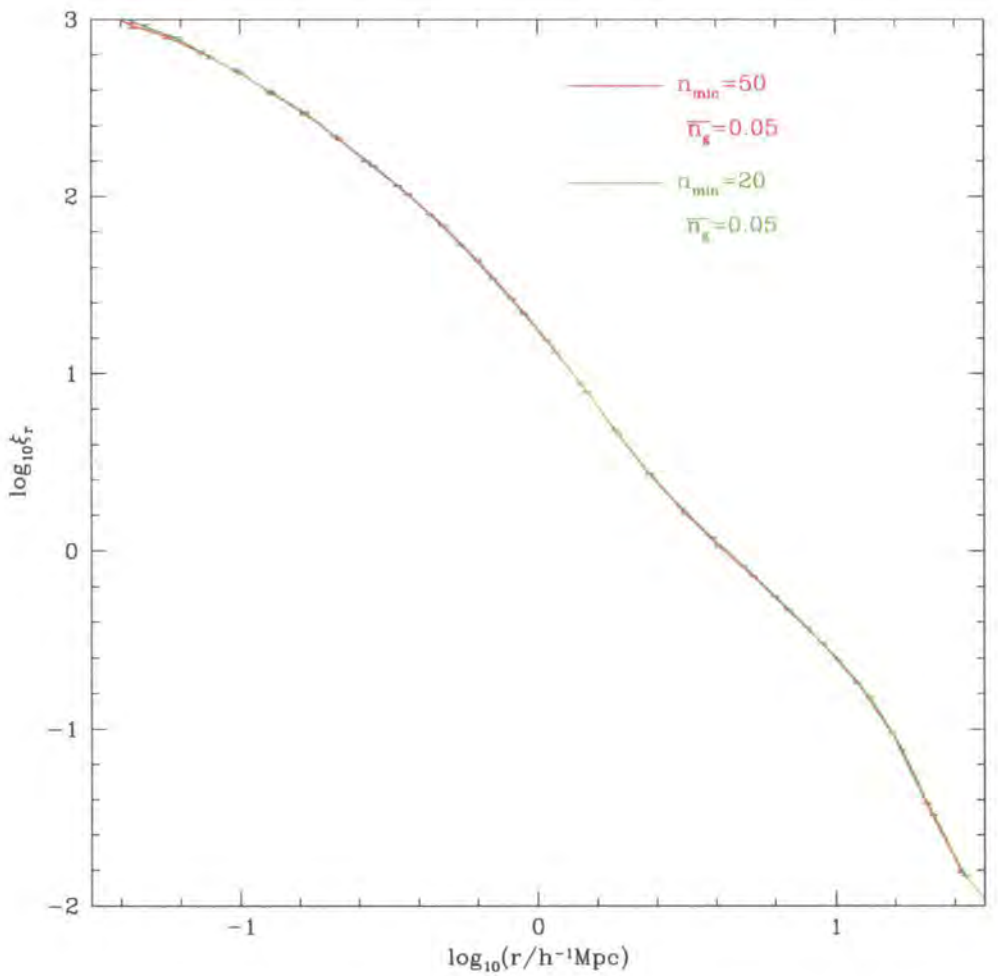

Figure 4.3: A resolution test in the doh256 simulation. The green line shows the correlation function for galaxies with absolute r-band magnitude, $M_r < -17.54$ when we use our default parameters for populating the simulation, i.e. where the minimum mass for a halo we consider to be resolved corresponds to 20 simulation particles. The red line shows the correlation function when we increase this to 50 particles.

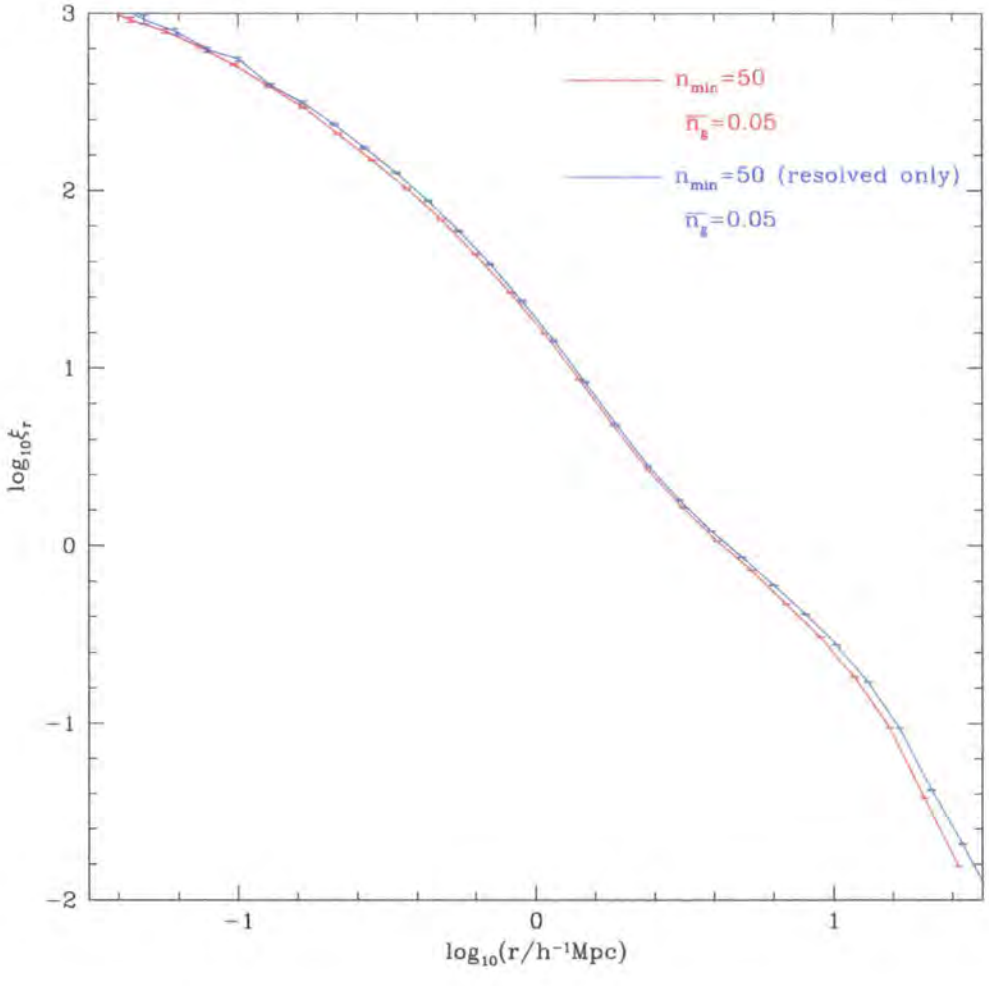

Figure 4.4: A further resolution test in the doh256 simulation. The red line is the same as in Fig. 4.3, and gives the correlation function for galaxies with $M_r < -17.54$ when we conservatively consider only haloes with more than 50 particles to be resolved, but where we employ our normal scheme for assigning galaxies to unresolved haloes. The blue line gives the result when we entirely neglect galaxies which would reside in haloes with mass corresponding to less than 50 simulation particles.

Table 4.3: The space density of the SDSS samples to which we compare our semi-analytic catalogues. Also shown is the corresponding magnitude threshold, the maximum redshift of the sample (the minimum redshift always being 0.02) and the total number of galaxies in the sample. The asterisk indicates the sample for which the maximum redshift was reduced to excise a large, very overdense region.

$M_r^{\max}$	$z^{\max}$	$N_{\rm gal}$	$100\bar{n}_{\rm g}$ / h^3 Mpc^{-3}
-22.0	0.22	3626	0.006
-21.5	0.19	11712	0.031
-21.0	0.15	26015	0.117
-20.5	0.13	36870	0.308
-20.0	0.10	40660	0.611
-20.0	0.06*	9161	0.574
-19.5	0.08	35854	1.015
-19.0	0.06	23560	1.507
-18.5	0.05	14244	2.060
-18.0	0.04	8730	2.692

a large, very overdense region). We have been provided with these correlation functions, and their covariance matrices calculated by jackknife resampling. Zehavi et al. (2005) also tabulate the space density of each sample, so it is straightforward for us to select corresponding samples of semi-analytic galaxies. We reproduce the first four columns of their table 2 in Table 4.3 for convenience; for further details of the sample selection we refer the reader to Zehavi et al. (2005).

4.2.2 The halo occupation distribution

We discussed the halo occupation distribution (HOD) formalism in Section 1.2.3. Recall that, if we know how haloes cluster and how galaxies are distributed within haloes, the functions $\langle N(M)\rangle$ (the mean number of galaxies in a halo of mass M) and $P(N|\langle N\rangle)$ (the dispersion about this mean) completely specify the galaxy clustering, subject to the caveats we discussed in Section 1.2.3. Our scheme for populating haloes specifies that the central galaxy is stationary at the centre of a halo, and that satellite galaxies trace the mass of the halo. The remaining part of the HOD, $P(N|M)$, is a rather direct output

of our semi-analytic model. Figs. 4.5–4.8 show the HODs produced by our GALFORM models for samples with galaxy space density $\bar{n}_g = 0.00308\ h^3\ \mathrm{Mpc}^{-3}$. In Figs. 4.5 and 4.6 we show the mean occupation functions for the grid of cosmologies from Run 1, while in Figs. 4.7 and 4.8 we show those from Run 2. Figs. 4.5 and 4.7 are for the models where we allow ourselves to change the parameters to match the luminosity function, while Figs. 4.6 and 4.8 are for those where we fix the parameters to the ones calibrated in the fiducial $(\Omega_m, \sigma_8) = (0.3, 0.8)$ output. Most of the HODs have the canonical 'step function + power law' form, and for many cosmologies the mean occupation function is very similar for all three models. The ragged HODs for some of the high Ω_m models illustrate the difficulty we had fitting parameters in extreme cosmologies.

As for the models of Chapter 3, we find the mean occupation function is usually well fit by the parametrization of Zheng et al. (2005) given in Equation 3.2. We also find that the scatter, $P(N|\langle N\rangle)$, is consistent with the model suggested by Kravtsov et al. (2004) for the occupation of haloes by dark matter substructures (rather than galaxies): the central galaxies follow a 'nearest integer' distribution with mean $\langle N_{\mathrm{cen}}\rangle$ while the satellite galaxies follow a Poisson distribution with mean $\langle N_{\mathrm{sat}}\rangle$, where $\langle N_{\mathrm{sat}}\rangle + \langle N_{\mathrm{cen}}\rangle = \langle N\rangle$.

To quantify this, we define α by

$$\alpha^2 \equiv \frac{\langle N(N-1)\rangle}{\langle N\rangle^2} \quad . \tag{4.5}$$

It gives an indication of the width of a distibution, larger α corresponding to a broader distribution. For a Poisson distribution, $\alpha = 1$. If the central and satellite galaxies do indeed follow the above distributions, then for $N > 1$ we have $N = 1 + N_{\mathrm{sat}}$ with

$$\frac{\langle N_{\mathrm{sat}}(N_{\mathrm{sat}}-1)\rangle}{\langle N_{\mathrm{sat}}\rangle^2} = 1 \quad . \tag{4.6}$$

Then,

$$\alpha^2 = \frac{\langle N_{\mathrm{sat}}(N_{\mathrm{sat}}+1)\rangle}{\langle N\rangle^2} \tag{4.7}$$

$$= \frac{\langle N_{\mathrm{sat}}(N_{\mathrm{sat}}-1) + 2N_{\mathrm{sat}}\rangle}{\langle N\rangle^2} \tag{4.8}$$

so that by using Equation 4.6 we have

$$\alpha^2 = \frac{\langle N_{\mathrm{sat}}\rangle^2 + 2\langle N_{\mathrm{sat}}\rangle}{\langle N\rangle^2} \tag{4.9}$$

$$= \frac{(\langle N_{\mathrm{sat}}\rangle + 1)^2 - 1}{\langle N\rangle^2} \tag{4.10}$$

$$= \frac{\langle N\rangle^2 - 1}{\langle N\rangle^2} \tag{4.11}$$

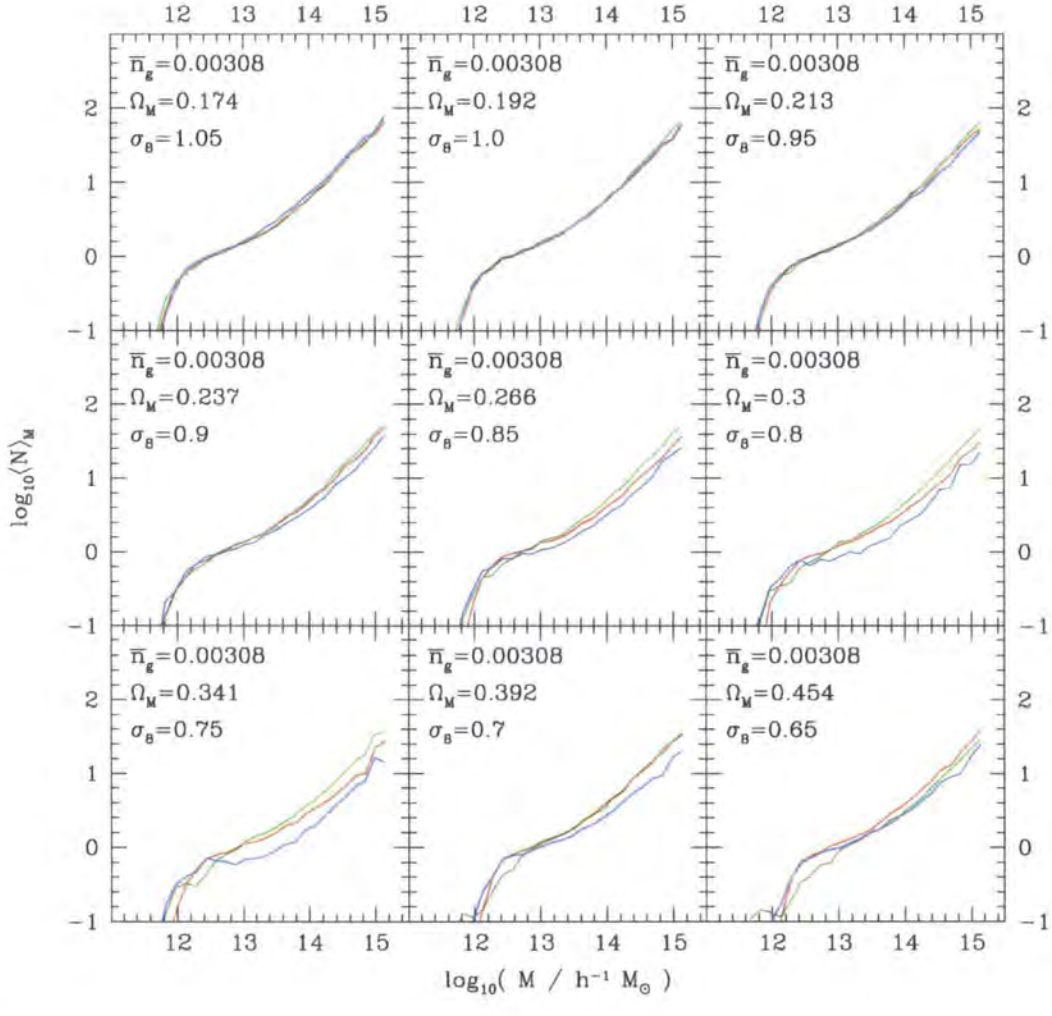

Figure 4.5: The mean occupation function of the HOD for cosmologies from doh512 Run 1, for a galaxy sample with space density $\bar{n}_g = 0.00308\ h^3\ \mathrm{Mpc}^{-3}$ from each of our models. The red line corresponds to the Cole2000 model, green to C2000hib and blue to Model M (we use this colour scheme consistently henceforth). This is the set of models for which we allow ourselves to tweak the parameters to match the luminosity function.

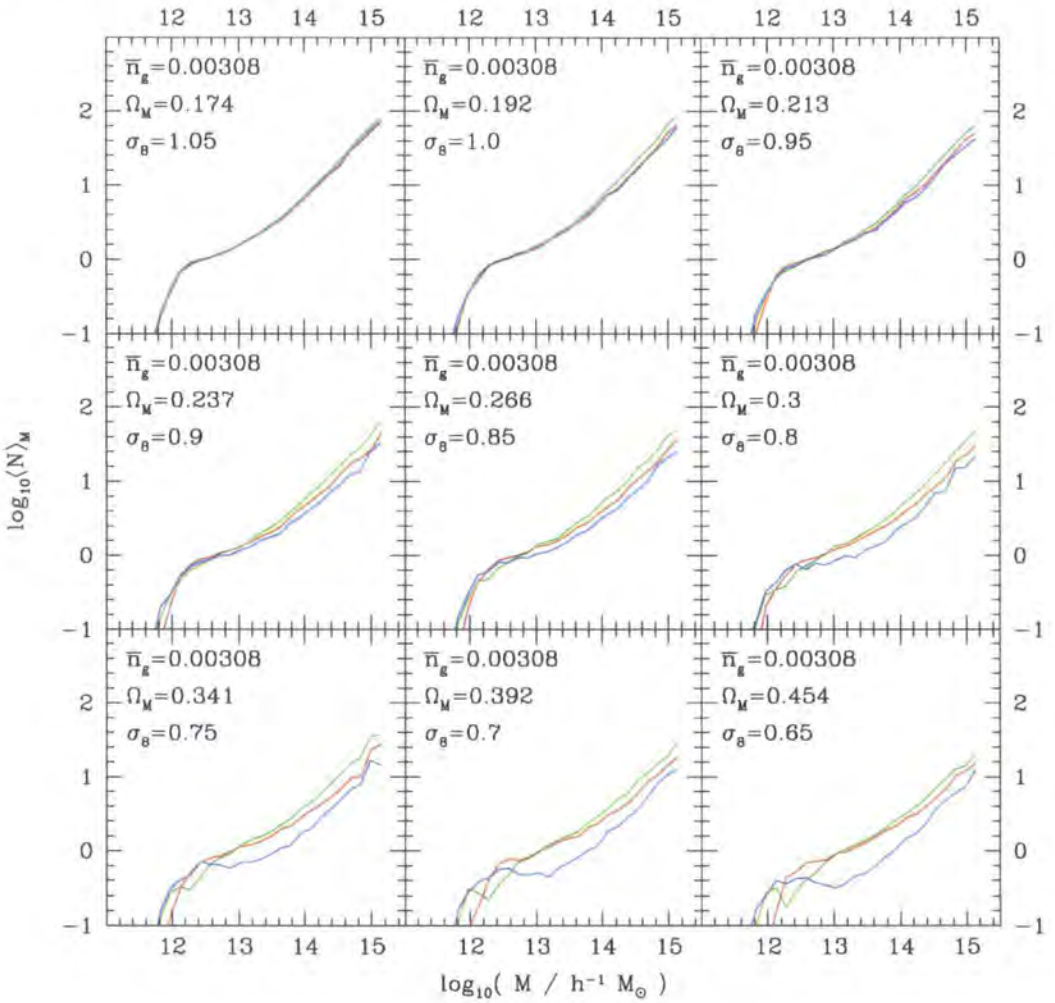

Figure 4.6: $\langle N(M)\rangle$ for cosmologies from doh512 Run 1, without varying parameters.

giving, finally,

$$\alpha^2 = 1 - \frac{1}{\langle N\rangle^2} \quad . \tag{4.12}$$

Given $\langle N(M)\rangle$, comparing the value of α^2 given by the GALFORM prediction for $\langle N(N-1)\rangle$ with the prediction given by Equation 4.12 as a function of mass, as done by Kravtsov et al. (2004) for their substructures, confirms the prediction. This can be seen in Figure 4.9. The scatter from the model (black points) agrees with that predicted by Equation 4.12 (green curve) over most of the mass range. For low mass haloes with $0 < \langle N\rangle < 1$, there is some indication that the model produces slightly more scatter than assumed if we take the probability of a central galaxy being present as given by the 'nearest integer' distribution. The *overall* scatter in the HOD for small $\langle N\rangle$ is sub-Poisson, as noted by other authors. The satellite galaxies on their own give values of α closer to unity. Finally, note that

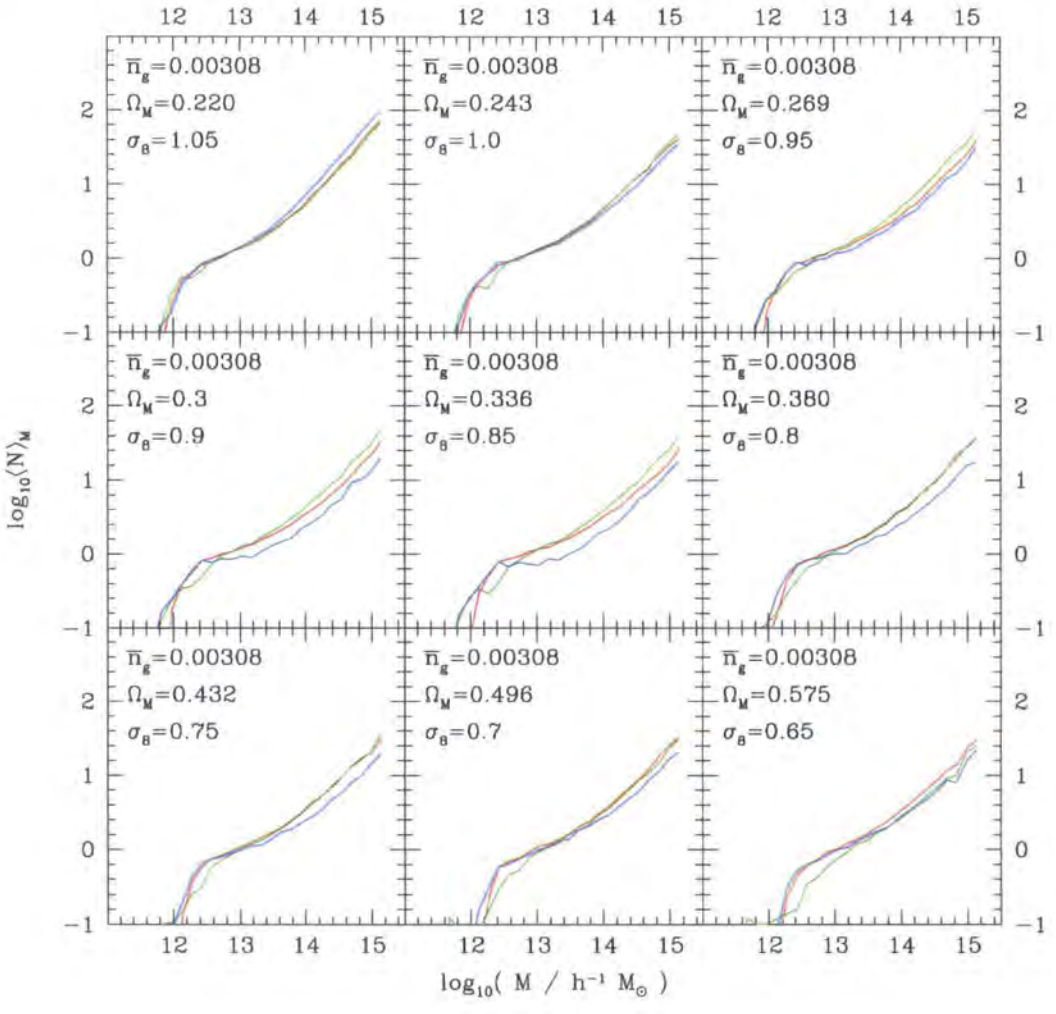

Figure 4.7: $\langle N(M)\rangle$ for cosmologies from doh512 Run 2.

the blue curve, which shows the case when the probability distribution $P(N|\langle N\rangle)$ is very narrow, is clearly inconsistent with our model.

4.2.3 Clustering results

We show the projected correlation function $w_p(r_p)$, a function of projected radius r_p, for our models and for the SDSS in Figs. 4.10–4.13. The order in which our four grids of models appear is the same as for Figs. 4.5–4.8. In fact, we plot $r_p w_p(r_p)$ since this scales out much of the r_p-dependence and makes differences in shape easier to see. The projected correlation function is related to the three-dimensional correlation function $\xi(r_p, \pi)$ (where

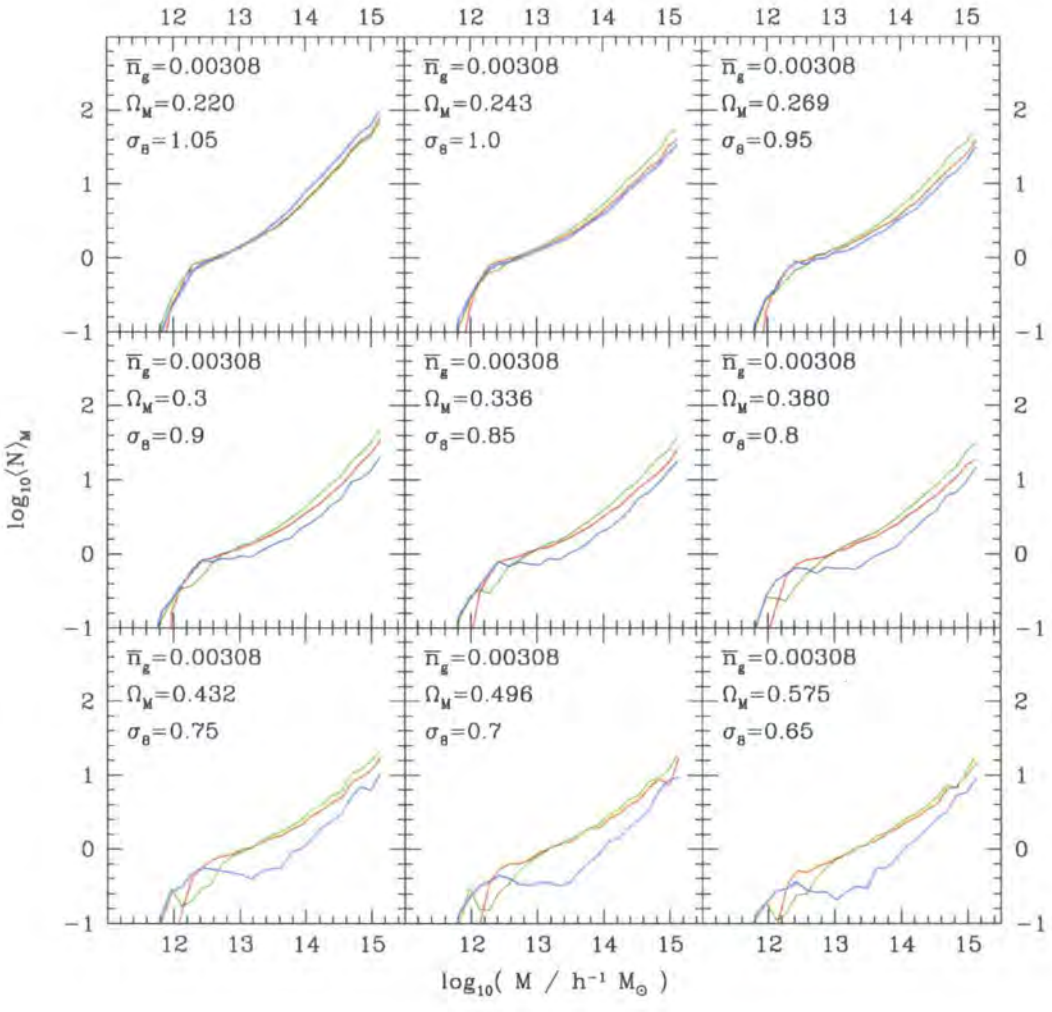

Figure 4.8: $\langle N(M) \rangle$ for cosmologies from doh512 Run 2, without varying parameters.

π is the coordinate in the redshift direction) by

$$w_{\rm p}(r_{\rm p}) = 2 \int_0^\infty \xi(r_{\rm p}, \pi) {\rm d}\pi \quad . \tag{4.13}$$

In the models, it is as convenient for us to compute $w_{\rm p}(r_{\rm p})$ directly, or from the spherical real-space correlation function $\xi(r)$ by

$$w_{\rm p}(r_{\rm p}) = 2 \int_{r_{\rm p}}^\infty r\xi(r) \left(r^2 - r_{\rm p}^2\right)^{-1/2} {\rm d}r \tag{4.14}$$

(Davis & Peebles, 1983). Although in principle the upper limit of the integral is infinity, we only have the real-space correlation function tabulated out to a radius of $\sim 130\ h^{-1}$ Mpc. We extrapolate the correlation function to infinity by fitting a power-law on large scales and extrapolating that, though we have also checked that our results are robust if we use

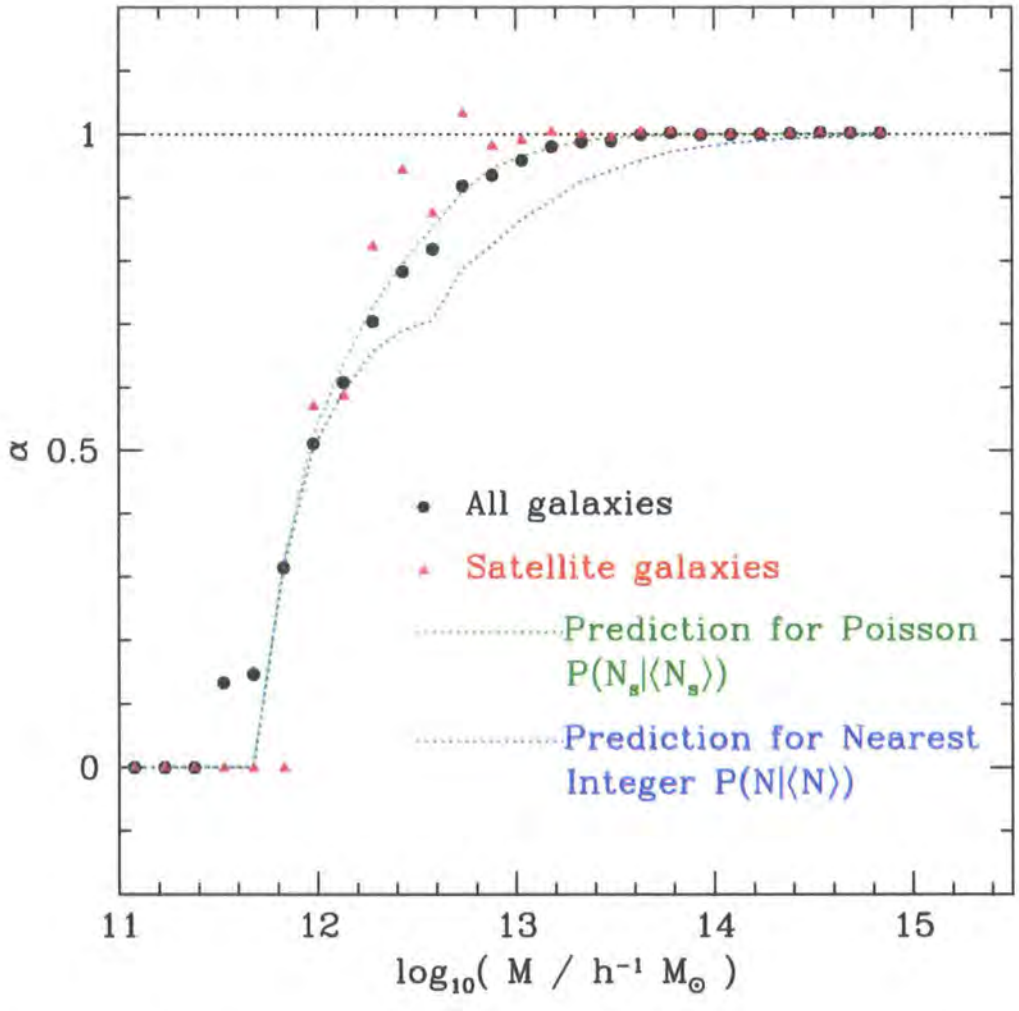

Figure 4.9: The width of $P(N|\langle N\rangle)$ as a function of mass in our GALFORM model, compared a simple prescription. We plot α as defined in Equation 4.5 for a typical GALFORM model with $\bar{n}_{\rm g} = 0.02$. To calculate α for the points we use the scatter predicted by the model, for all galaxies (black points) and for satellite galaxies only (red triangles). To obtain the green curve we use Equation 4.12, which tells us, given $\langle N\rangle$ from the model, what α we would expect if $P(N_{\rm sat}|\langle N_{\rm sat}\rangle)$ follows a Poisson distribution. To obtain the blue curve we assume instead that the number of galaxies follows the very narrow 'nearest integer' distribution.

the dark matter correlation function to extrapolate further (with a bias measured from the large-scale galaxy correlation function), or even if we merely truncate the integral, so long as we do not use the $w_{\rm p}(r_{\rm p})$ information for $r_{\rm p} \gtrsim 50\ h^{-1}$ Mpc.

The space density of galaxies in Figs. 4.10–4.13 is $\bar{n}_{\rm g} = 0.00308\ h^3\ {\rm Mpc}^{-3}$, so that the samples are the same as those in Figs. 4.5–4.8. We choose this space density to compute the values of χ^2 from which we try to constrain σ_8, since it provides a good compromise between volume and space density (and hence has relatively small errors) without the ambiguity in the redshift cutoff of the $M_r = -20.0$ sample. The different panels of Figs. 4.10–4.13 show the results for different cosmologies.

For the higher σ_8 cosmologies, the shape of the models fits that of the data rather well. The trend between cosmologies is consistent between the three models: a higher amplitude of clustering for higher σ_8, as expected. There are differences between the models, however, especially on small scales.

We calculate the correlation length of the samples by fitting a power law to $\xi(r)$ for $2 < r/(\,h^{-1}\ {\rm Mpc}) < 20$; that is, we parametrize the correlation function as $\xi(r) = (r/r_0)^{-\gamma}$ where r_0 is the correlation length. We have done this for all our samples of all luminosities, so we are able to plot the correlation length as a function of sample space density (or, equivalently, as a function of sample luminosity threshold) in Figs. 4.14–4.17. The order in which we show the grids is, again, the same as for Figs. 4.5–4.8. The black line in the plots shows the corresponding result from the SDSS. The SDSS data show a steady increase in clustering strength with luminosity (i.e. with decreasing space density) apart from a feature at $\bar{n}_{\rm g} \approx 0.006\ h^3\ {\rm Mpc}^{-3}$ corresponding to the difference between the two $M_r^{\rm max} = -20.0$ samples: the one which has a large, overdense region excised has lower space density but, as might be expected, weaker clustering.

For many cosmologies, the Cole2000 and C2000hib models do a reasonable job of matching the luminosity-dependent clustering in the SDSS, especially for samples of moderate to low space density. Model M does not do so well, predicting very little luminosity dependence. This may be because the feedback effects are so extreme in large haloes that their central galaxies are little brighter (if at all) than those at the centre of less massive, less biased haloes. The other two models tend to have the opposite problem in the brightest samples: they tend to predict too high an amplitude of clustering. This could be due to too tight a relationship between halo mass and galaxy luminosity (perhaps because feedback is not quite efficient or stochastic enough): none of the brightest galaxies are scattered into lower mass, less biased haloes. A generic feature of the GALFORM models

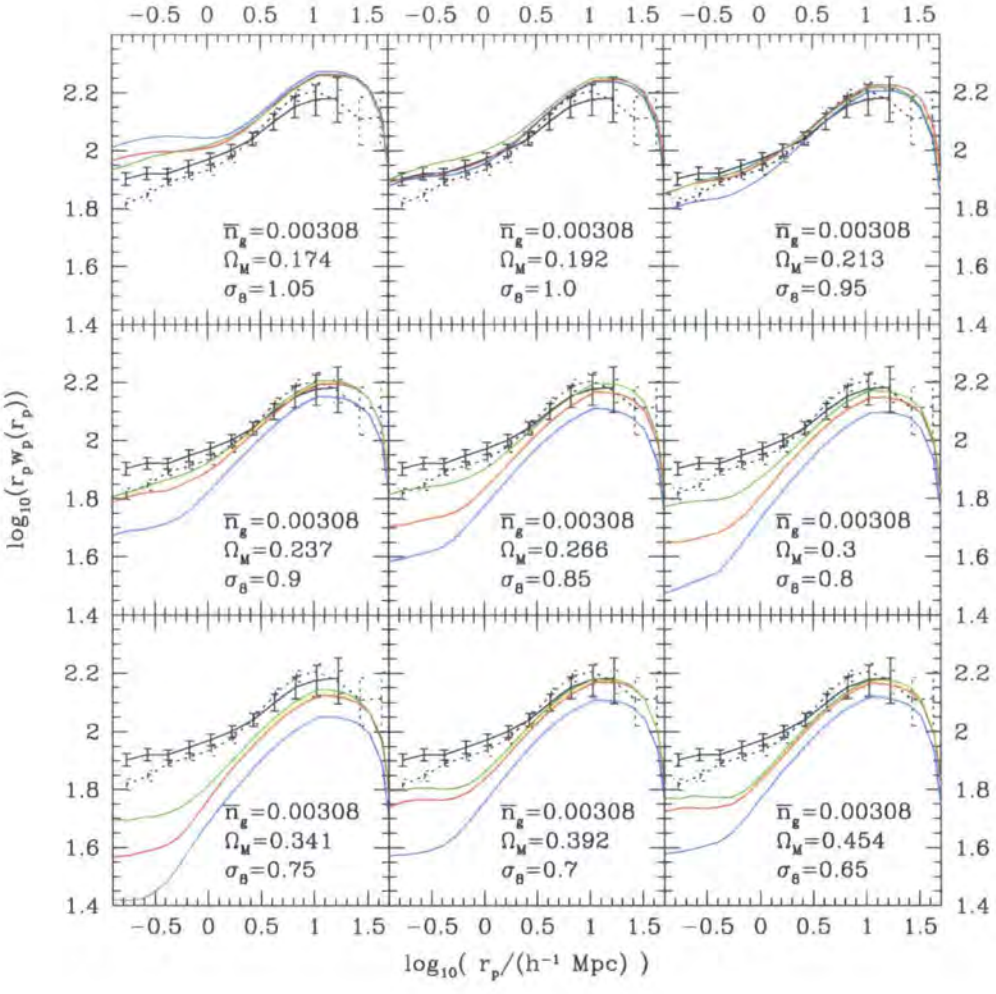

Figure 4.10: The projected correlation function for the same models in the same grid of cosmologies as in Fig. 4.5. The galaxy sample is also the same, having space density $\bar{n}_g = 0.00308\ h^3\ \mathrm{Mpc}^{-3}$. We compare to a corresponding sample in the SDSS. $r_p w_p(r_p)$ is plotted to scale out most of the r_p-dependence. The solid, black line with error bars is the SDSS data; the dotted line shows the correlation function of the SDSS flux-limited sample for comparison. The coloured lines are from our three models: red for Cole2000, green for C2000hib and blue for Model M, as in Fig. 4.5.

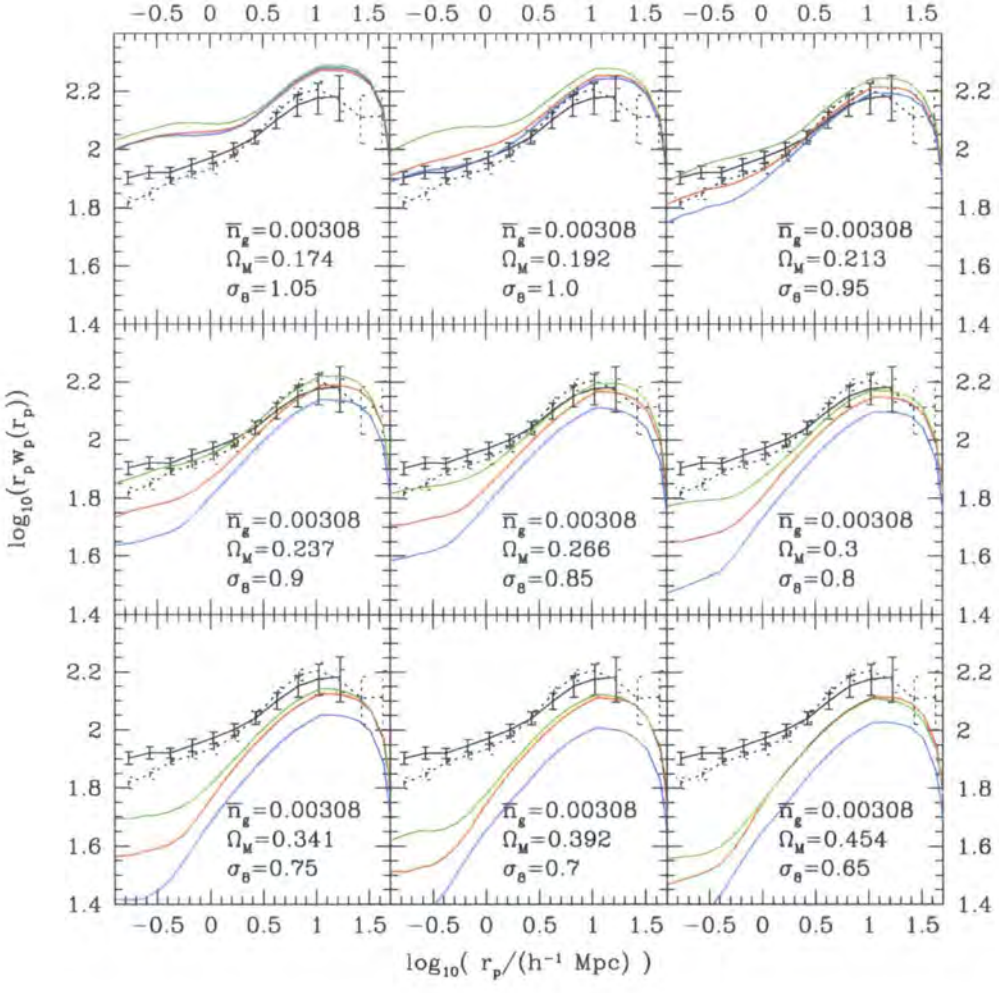

Figure 4.11: The projected correlation function for cosmologies from doh512 Run 1, without varying parameters.

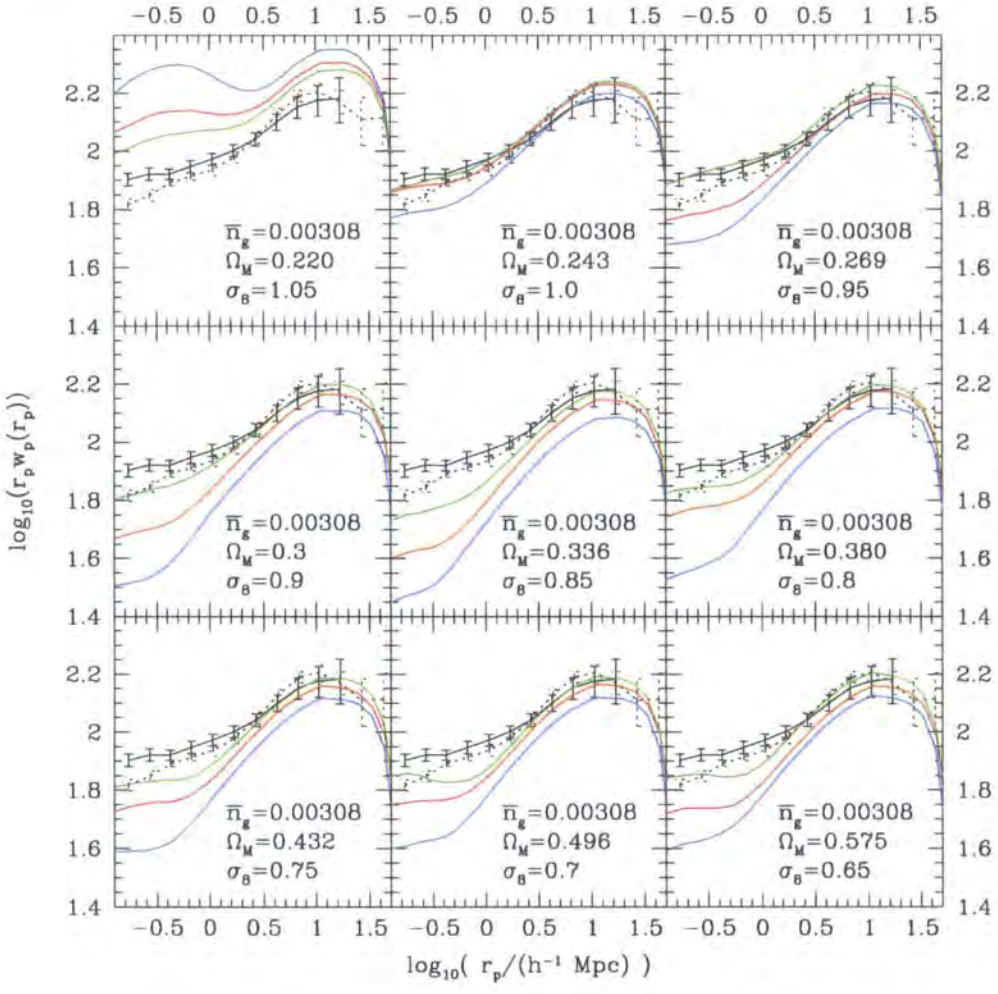

Figure 4.12: The projected correlation function for cosmologies from doh512 Run 2.

seems to be an upturn in the clustering amplitude at high space density. This suggests that too many of the faint galaxies generated by the model reside in high mass haloes: in HOD terms, the high mass slope of the mean occupation function at low luminosity thresholds may be too steep. This may be related to the fact that it is hard to produce a luminosity function with a flat enough faint-end slope, the excess of faint galaxies perhaps being satellites in massive haloes.

Clearly, matching the luminosity-dependent clustering of galaxies will continue to be a very stringent test for semi-analytic models. Even if the models were provided with the correct cosmology as an input, matching the clustering would still seem to require that the models predict the correct galaxy population for haloes as a function of luminosity and mass, rather than predicting quantities which implicitly average over a range of

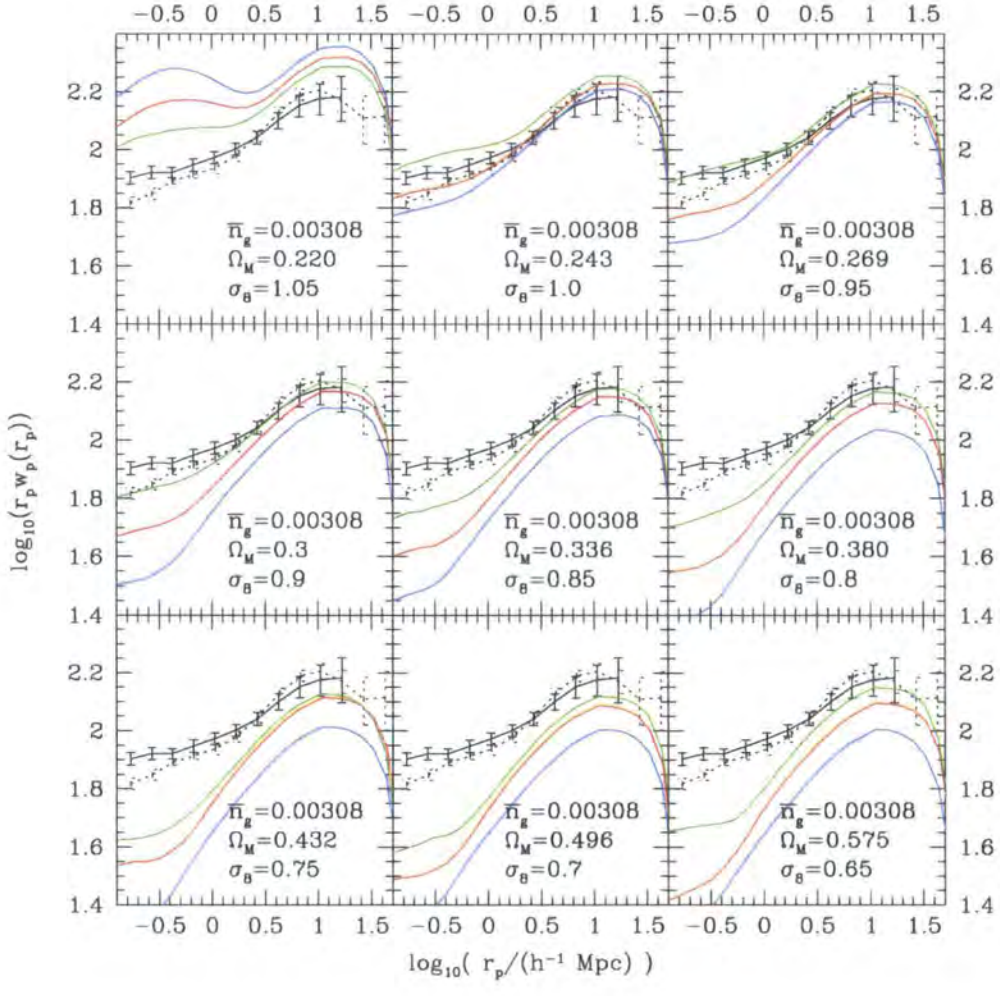

Figure 4.13: The projected correlation function for cosmologies from doh512 Run 2, without varying parameters.

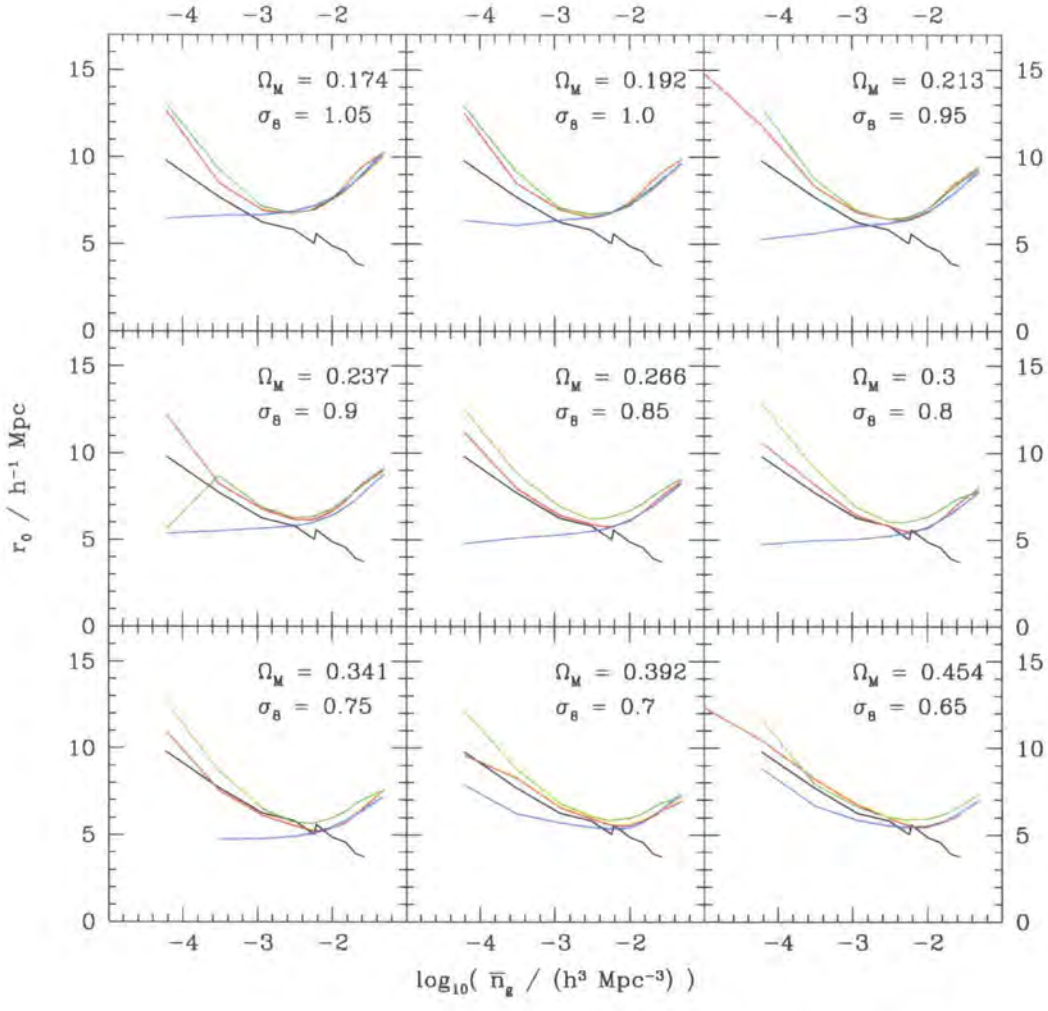

Figure 4.14: Correlation length as a function of sample space density for the cosmologies in Run 1, compared to the SDSS. Zehavi et al. (2005) compute the correlation length in the SDSS by fitting a power law to the projected correlation function and using an analytic formula to find the corresponding value for the three-dimensional correlation function. We calculate it directly by fitting a power law to the three-dimensional correlation function between 2 and 20 h^{-1} Mpc, giving $\xi(r) = (r/r_0)^{-\gamma}$ where r_0 is the correlation length. The colour coding is as in Figs. 4.5 and 4.10.

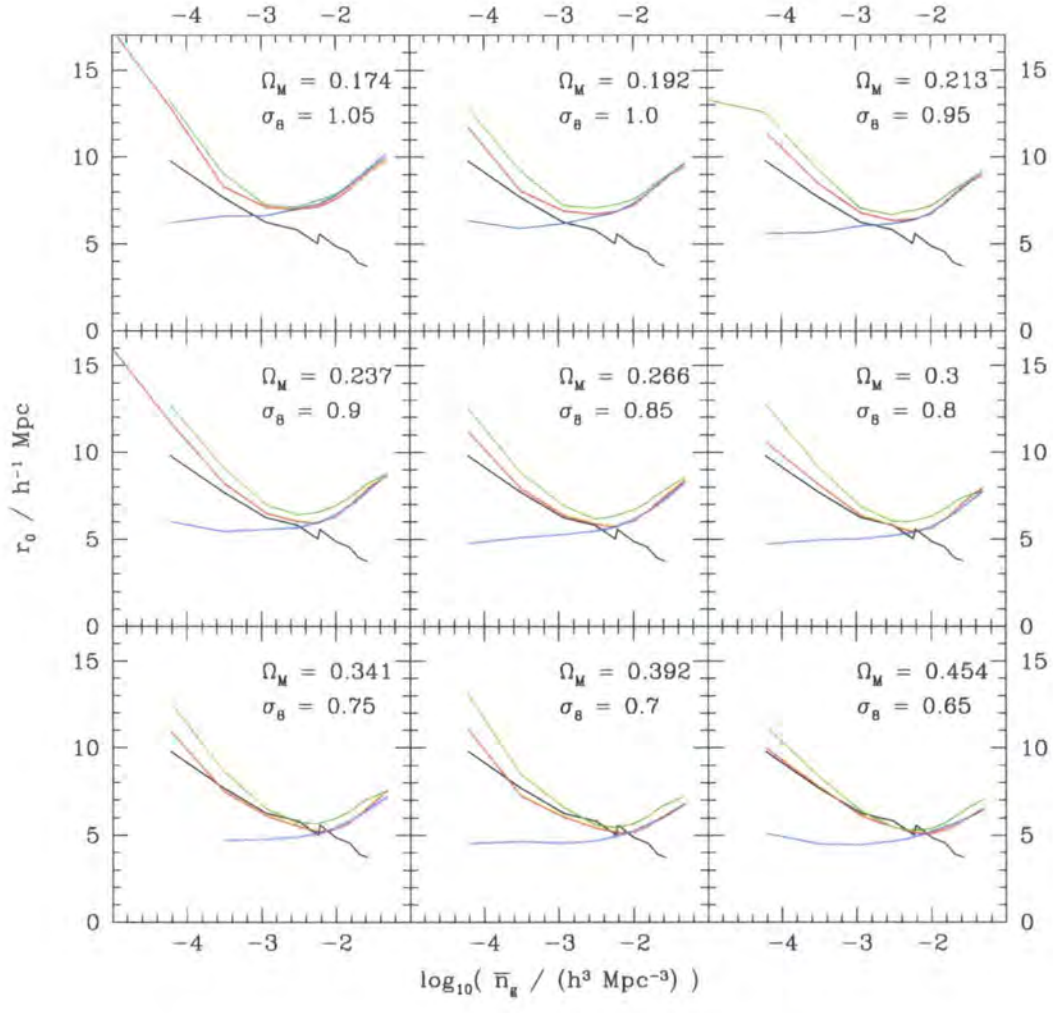

Figure 4.15: Correlation length as a function of sample space density for Run 1, without varying parameters.

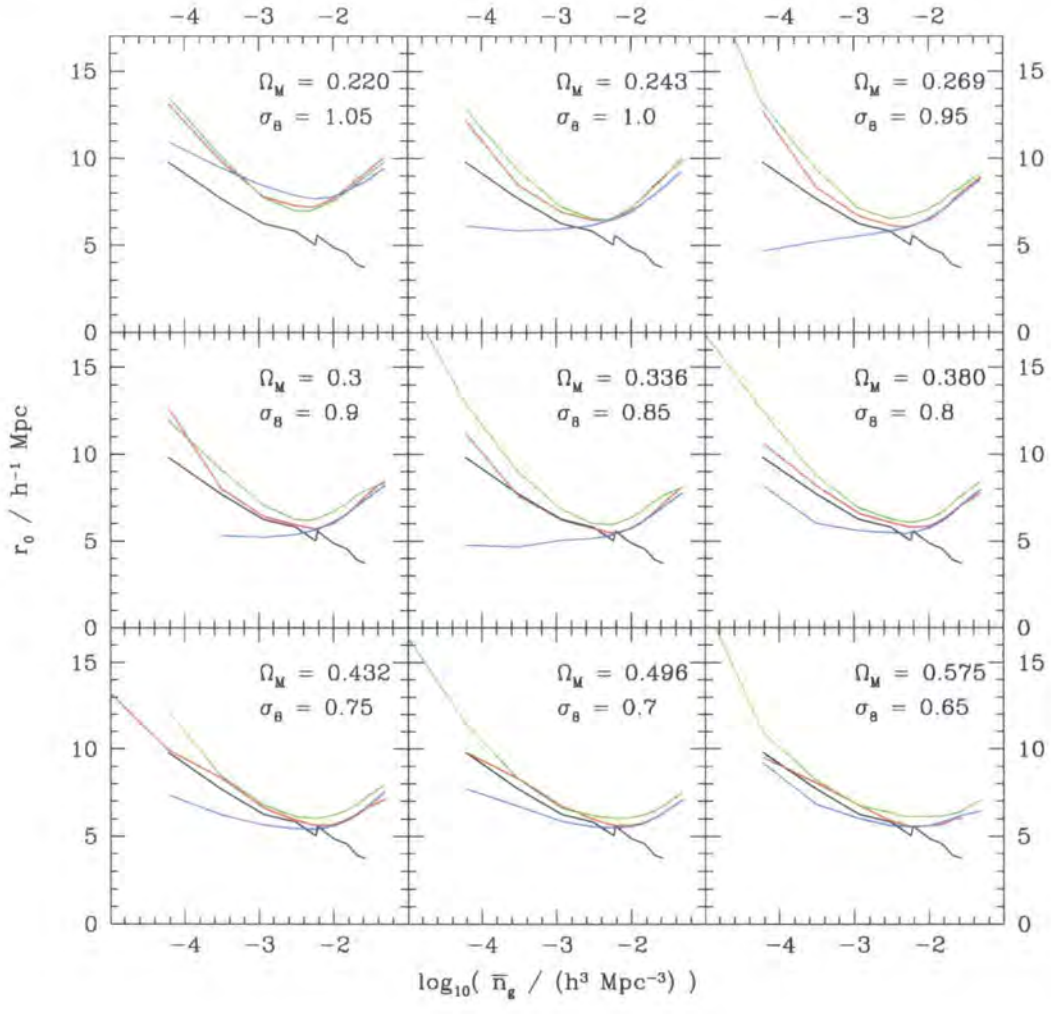

Figure 4.16: Correlation length as a function of sample space density for Run 2.

halo mass, such as the (unconditional) galaxy luminosity function. Conversely, if the models were able to correctly capture the trends of luminosity dependent clustering, it would give us more confidence that they were predicting realistic galaxy populations on a halo-by-halo basis, and give a firmer foundation for attempts to constrain cosmology with methods involving semi-analytic catalogues. Though we bear this in mind, it seems unrealistic to require a perfect and complete model of galaxy formation before considering the information it can provide us on cosmological parameters. Our models provide realistic catalogues in many other respects, and in the next section we examine the precision with which we might expect to measure cosmological parameters using the models.

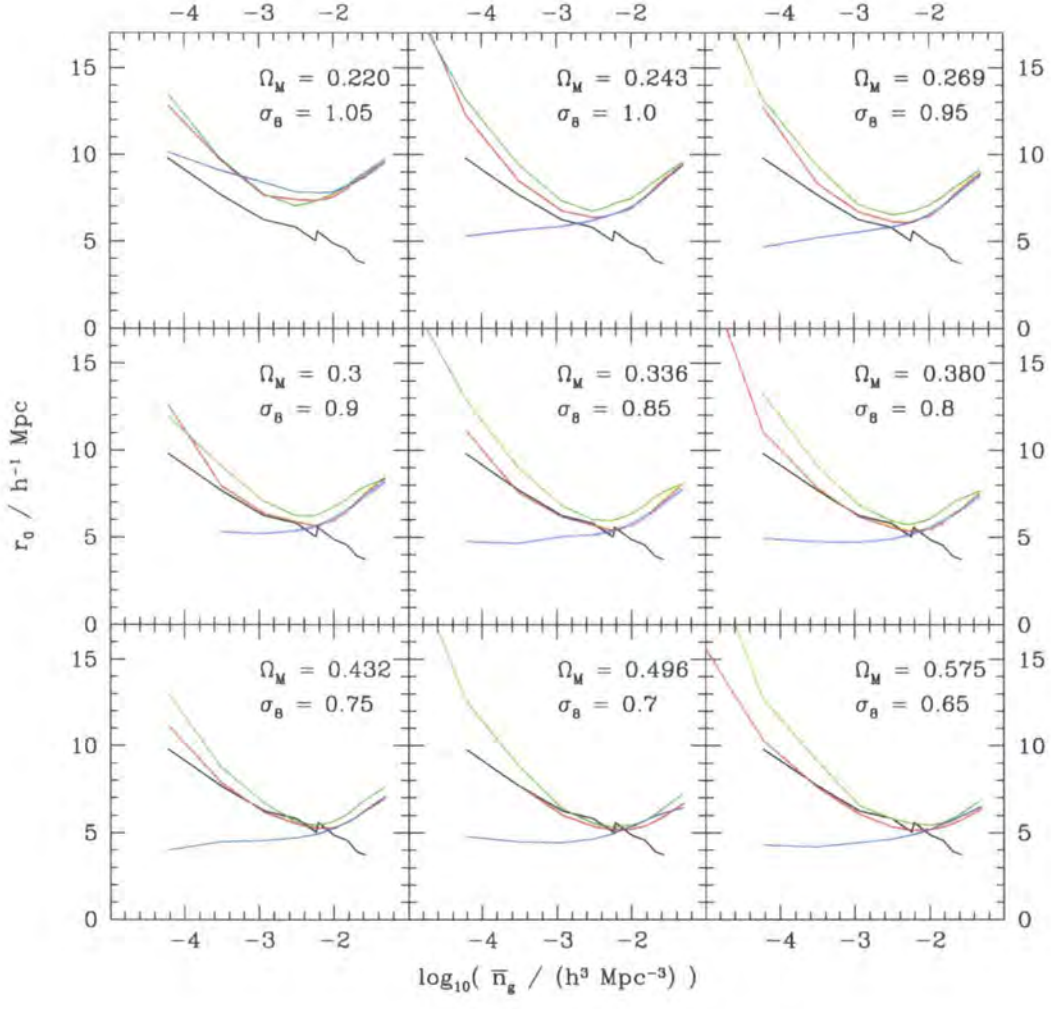

Figure 4.17: Correlation length as a function of sample space density for Run 2, without varying parameters.

Table 4.4: The key to the model numbering used in Fig. 4.18. The first column gives the label we assign to each of our 12 grids of populated simulations (each of which has nine cosmologies, regularly spaced in σ_8).

Model no.	Grid	Same/diff. pars.	GALFORM model
1	1	diff.	C2000hib
2	1	diff.	Cole2000
3	1	diff.	M
4	1	same	C2000hib
5	1	same	Cole2000
6	1	same	M
7	2	diff.	C2000hib
8	2	diff.	Cole2000
9	2	diff.	M
10	2	same	C2000hib
11	2	same	Cole2000
12	2	same	M

4.2.4 Cosmological constraints

For each of our populated simulations, we calculate χ^2 between the model and measured $w_{\rm p}(r_{\rm p})$ by reference to the $\bar{n}_{\rm g} = 0.00308\ h^3\ {\rm Mpc}^{-3}$ SDSS correlation function and covariance matrix. Then, for each grid of models (i.e. a set of nine χ^2 values, one for each of the different cosmologies in one of the simulation runs, for one variant of one of the GALFORM models) we are able to calculate a best-fitting σ_8 value and error bars, by fitting a quadratic through the three points with lowest χ^2. We therefore have 12 grids (two variants of each of three GALFORM models in each of two simulation runs) each of which generates an estimate, with errors, of σ_8. To plot our constraints, it is convenient to assign a label to each of these 12 grids. The numbering scheme is shown in Table 4.4.

The constraints themselves are shown in Fig. 4.18. The consistency between the first six models (in Run 1) and the second six models (in Run 2, which for any given σ_8 has lower $\Omega_{\rm m}$ than Run 1) confirms that we obtain an almost pure constraint on σ_8. This is as expected, since changing the overall amplitude of clustering has a large effect on χ^2. Since we use only two simulations so that the different estimates cannot be considered

independent and have their constraints combined, we can see only that overall we predict $\sigma_8 \approx 0.96$, with a statistical error of approximately ± 0.03. We do not give much weight to the constraints from models 8, 9, 11 and 12 since the best-fitting cosmology in each case is not a good fit in the χ^2 sense, while the other models all give an acceptable reduced χ^2 of ~ 1 for their best-fitting σ_8. The error bars for models 8, 9, 11 and 12 are artificially small, the large values of χ^2 involved giving an artificially steep minimum in χ^2 as a function of σ_8. Looking at models 1–6, which are all constructed in doh512 Run 1, gives us some idea of the systematic errors arising from our choice of semi-analytic model. The best-fitting models of Run 1 cover a range of ~ 0.07 in σ_8. Therefore we estimate this source of error gives an uncertainty of approximately ± 0.04, so that our final constraint is $\sigma_8 = 0.96 \pm 0.05$, adding the above systematic errors to the statistical errors in quadrature.

For each model shown in Fig. 4.18 we plot two estimates of σ_8. The black points show the estimates if we use the correlation functions plotted in Figs. 4.10–4.13. To obtain the red points, we use information from the models described in Chapter 3. We take the catalogue of the same space density used for our cosmological constraints, and calculate the ratio (as a function of scale) between the correlation function of the shuffled catalogue and the catalogue in which satellite galaxies are forced to trace the mass of the halo. We then divide the correlation functions of the catalogues in this chapter by this ratio, recompute the projected correlation functions and repeat our χ^2 analysis. This avoids the complications of altering the way we populate our simulations. Clearly, assembly bias of the magnitude seen in the models of Chapter 3 does not seriously affect our ability to constrain cosmology. Of more concern is the uncertainty in the small scale clustering arising from the ambiguity as to how to place galaxies within haloes. This affects our estimates of the correlation function on the nonlinear scales where we would most expect a halo-based model to help, and where observational clustering data are very precise.

4.3 Discussion

As we note in Chapter 1, galaxy clustering is not normally used to constrain σ_8, except insofar as by constraining other parameters it can break degeneracies inherent in using other techniques. Therefore it is interesting to compare our independent, low-redshift constraint on σ_8 with estimates from other data.

Arguably the most important recent measurement of cosmological parameters has come from WMAP. For flat, power-law ΛCDM, Spergel et al. (2006) report that WMAP

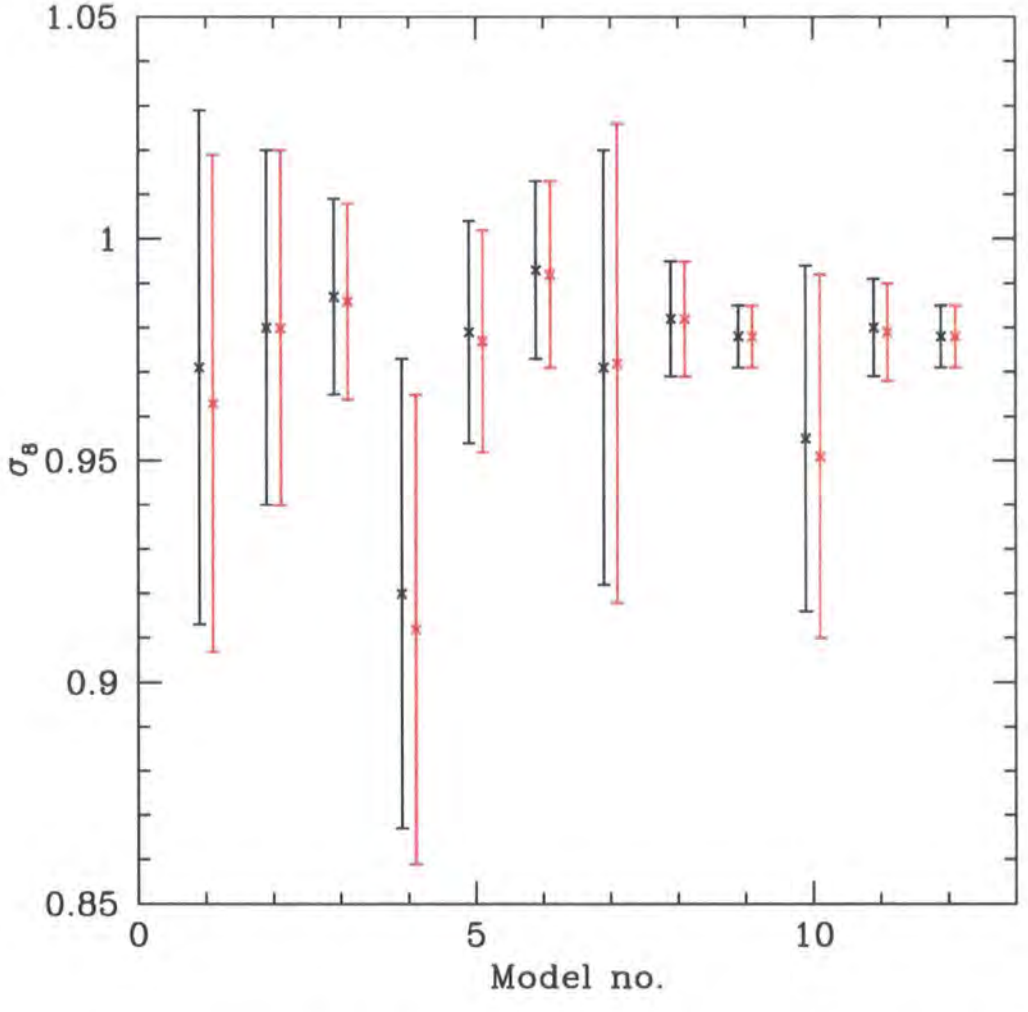

Figure 4.18: Constraints on σ_8. The x-axis shows the model number, the key to which is given in Table 4.4. The y-axis shows the 1σ constraint on σ_8 achieved in that particular model. The black points and error bars are for the unmodified catalogues. The red points and error bars show how the constraints change when we modify the correlation function according to the scale-dependent bias between shuffled and unshuffled GALFORM catalogues calculated from the data used in Chapter 3.

on its own constrains $\sigma_8 = 0.744^{+0.050}_{-0.060}$. This is clearly inconsistent with our estimate. The WMAP constraints change little if their data are combined with small-scale CMB measurements or the 2dFGRS power spectrum. Combining the WMAP data with recent supernova measurements (Knop et al., 2003; Riess et al., 2004; Astier et al., 2006) increases their best-fitting estimate to $\sigma_8 \sim 0.76$–0.78, with similar errors. The SDSS main galaxy or LRG power spectrum also pulls up the estimate, to $\sigma_8 \sim 0.77$–0.78, though the joint analysis by Tegmark et al. (2006) of the SDSS LRGs and WMAP gives $\sigma_8 = 0.756 \pm 0.035$.

Measurements of Ω_m and σ_8 from weak lensing surveys may be particularly interesting since their parameter constraints are nearly orthogonal to those from CMB measurements and complement them well (Tereno et al., 2005). Spergel et al. (2006) find that a joint analysis of the WMAP data with cosmic shear measurements from the Canada-France-Hawaii Telescope Legacy Survey (CFHTLS; Hoekstra et al., 2006; Semboloni et al., 2006) gives $\sigma_8 = 0.826^{+0.022}_{-0.035}$. On their own, weak lensing surveys tend to favour even higher values of σ_8 for typical WMAP values of Ω_m. For example, Hoekstra et al. (2006) report $\sigma_8 = 0.85 \pm 0.06$ (and would find larger values if $\Omega_m < 0.3$, as currently favoured); Seljak et al. (2005a) find $\sigma_8 = 0.88 \pm 0.06$ in their weak lensing analysis of SDSS galaxies; and Jarvis et al. (2006) find $\sigma_8 = 0.81^{+0.15}_{-0.10}$ from the CTIO lensing survey. These estimates are marginally consistent with ours. Not *all* weak lensing surveys produce such high values; Heymans et al. (2005) find $\sigma_8(\Omega_m/0.3)^{0.65} = 0.68 \pm 0.13$ in the HST GEMS survey, though they note the field used in their survey, the Chandra Deep Field South, is underdense in massive galaxies by a factor of two (Wolf et al., 2003).

As we note in Chapter 1, Lyman-α forest data help to constrain the spectral index and its possible scale-dependence. They can be used to constrain σ_8, though: Jena et al. (2005) find their measurements are consistent with $\sigma_8 = 0.9$, while Seljak et al. (2005b) quote $\sigma_8 = 0.90 \pm 0.03$ (reducing to 0.84 incorporating the new constraints on reionization from WMAP's 2006 data release). Measurements of cluster abundance have frequently been used to constrain σ_8, but provide a very wide range of estimates because of the difficulty in relating the properties of an observed cluster to its mass (e.g., Rasia et al., 2005). Recent estimates are, though, consistent with the WMAP determination of σ_8 (e.g. Pierpaoli et al., 2003).

The overall picture of the value of σ_8 from other methods is therefore a little confusing, but even the highest recent estimates are only marginally consistent with ours. As far as using galaxy data alone goes, methods involving higher-order correlations, particularly the three-point correlation function (or its Fourier counterpart the bispectrum) are promising

(e.g., Gaztañaga & Scoccimarro, 2005; Sefusatti et al., 2006), for example because of their ability to constrain the galaxy bias. The addition of dynamical information, for example redshift space distortions (Kaiser, 1987; Cole et al., 1994b; Tinker et al., 2006b) or the pairwise velocity dispersion (PVD; e.g., Peacock & Dodds, 1994; Jing & Börner, 2004) can also help constrain cosmological parameters and galaxy bias. An analysis including PVD information in the conditional luminosity function (CLF) framework by Yang et al. (2004, 2005) suggested relatively low values of σ_8, though this was inferred from their models with high σ_8 since low σ_8 simulations were not explicitly analysed.

An alternative approach using the 2dFGRS is employed by van den Bosch et al. (2005). Their methods are fundamentally halo-based: they study the abundance and radial distribution of satellite galaxies within the CLF framework, using mock galaxy catalogues produced by a semi-analytic code to calibrate their model. This calibration quantifies the impact of the inevitable imperfections in the halo finder that lead to satellite galaxies being spuriously identified as central galaxies of separate haloes, and vice versa. It also accounts for incompleteness effects in the 2dFGRS. Their results are consistent with other CLF analyses in suggesting that simultaneously matching the observed cluster mass-to-light ratio and the fraction of satellite galaxies in the 2dFGRS requires a low value of σ_8, lowering the abundance of very massive haloes with a great number of satellites. Again, they do not directly construct mock galaxy redshift surveys for a low σ_8 model, but using the same calibration parameters as for their $\sigma_8 = 0.9$ model leads them to believe that adopting $\sigma_8 = 0.7$ provides a better fit to the data.

The parameters of the conditional luminosity functions van den Bosch et al. (2005) use to fit the 2dFGRS data are tabulated in the paper. We have used these parameters to construct the corresponding HODs, then used the HODs to populate the Millennium Simulation and outputs of doh512 Run 1 with $\sigma_8 \approx 0.7$ and $\sigma_8 \approx 0.9$. We find the HODs look reasonable, though in some cases they are not quite monotonic (as one can see from Fig. 4.19), and in other cases they do not exhibit so clean a 'step function + power law' form as the GALFORM HODs, the step being somewhat washed out (see Fig. 4.20). We have checked that in the Millennium Simulation the CLF HOD catalogues match the 2dFGRS b_J-band luminosity function (Fig. 4.21), as they should by construction. Their clustering is consistent with the GALFORM catalogues of the same space density in the corresponding doh512 catalogues, as can be seen in Fig. 4.22. For $\sigma_8 = 0.7$, the CLF catalogues give too steep a faint-end slope of the 2dFGRS luminosity function, so that strictly speaking the CLF is incorrect, but they still match the clustering of the GALFORM

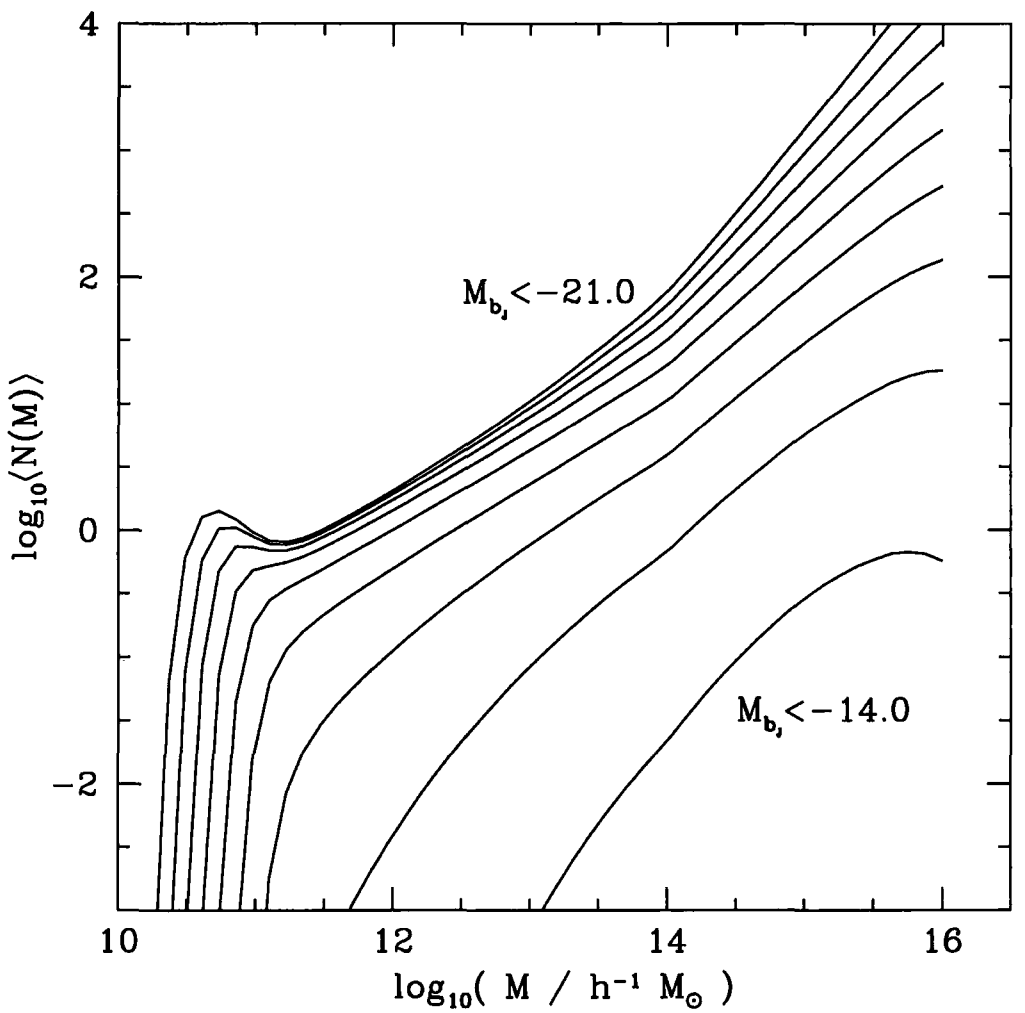

Figure 4.19: Mean occupation functions from the CLF for different sample luminosity thresholds between $M_{b_J} < -14$ and $M_{b_J} < -21$ in steps of 1. The CLF parameters are given by the model with ID 5 in table 1 of van den Bosch et al. (2005).

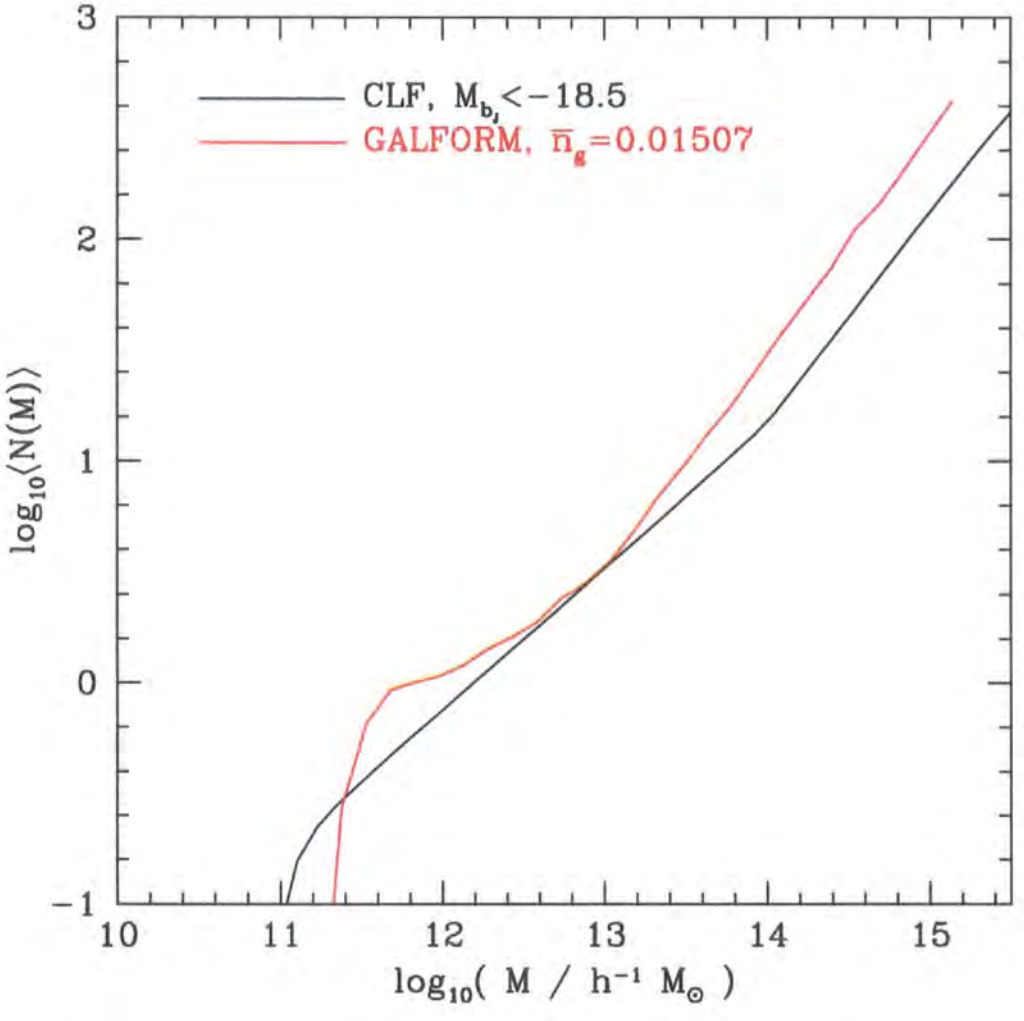

Figure 4.20: A mean occupation function using the CLF parameters given by the model with ID 5 in table 1 of van den Bosch et al. (2005) (as used in Fig. 4.19). It is compared to a GALFORM HOD for galaxies with a similar space density.

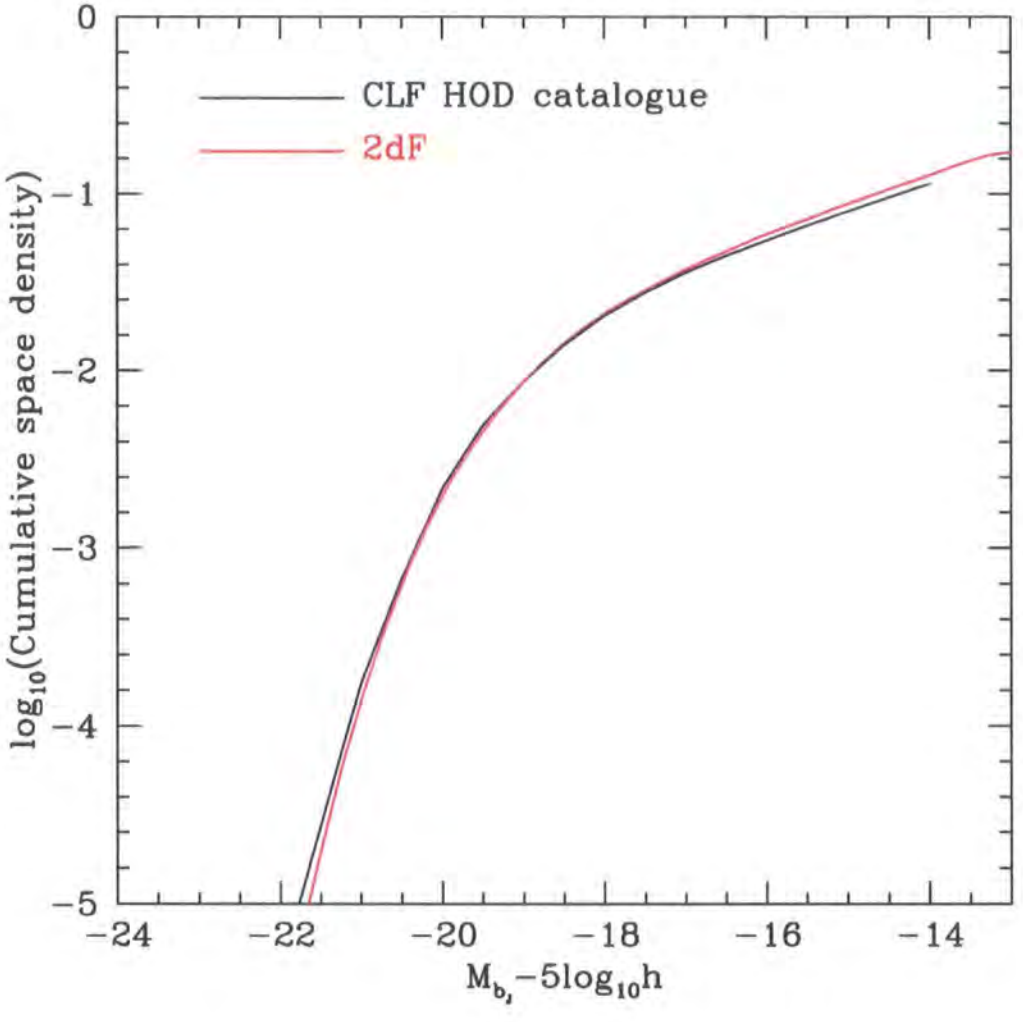

Figure 4.21: The luminosity function from a CLF catalogue in the Millennium Simulation, compared to the 2dFGRS luminosity function against which the CLF is calibrated. The CLF parameters are given by the model with ID 5 in table 1 of van den Bosch et al. (2005), as for Figs. 4.19 and 4.20.

catalogues in the same cosmology reasonably well.

The 2dFGRS correlation function, binned by luminosity, has been kindly provided to us by Peder Norberg. The low and high σ_8 CLF catalogues match the correlation function reasonably well (as do our GALFORM catalogues due to the agreement mentioned above and seen in Fig. 4.22), though perhaps the models give slightly too high an amplitude of clustering (surprisingly) in the $\sigma_8 = 0.7$ catalogues. Despite this agreement, by comparing to the SDSS data we have come to the conclusion that our best-fitting models have a high value of σ_8. We might conclude, then, that the difference between our value of σ_8 and that of van den Bosch et al. (2005) is driven by the data: we use the (r-selected)

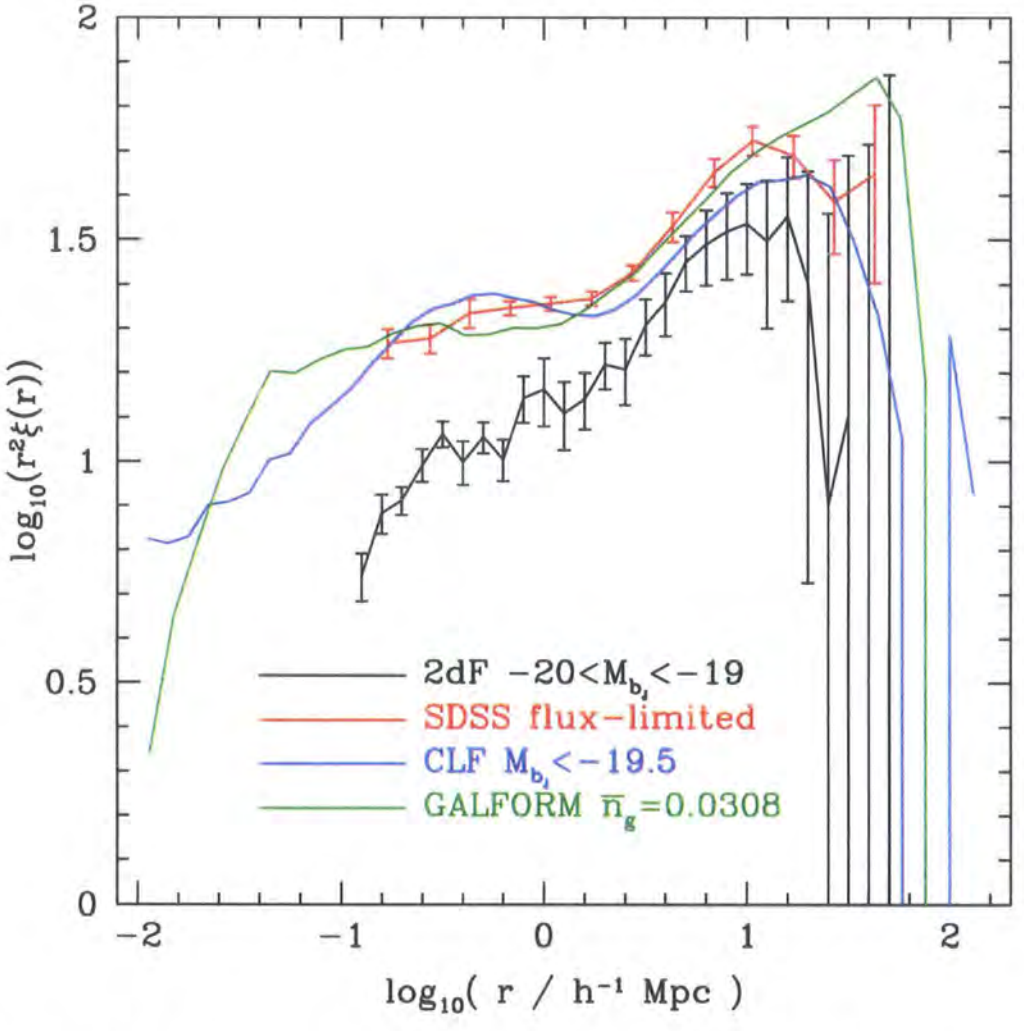

Figure 4.22: $r^2\xi(r)$ from a CLF catalogue in doh512 Run 1 (blue line), for the same CLF parameters as Figs. 4.19–4.21. We compare to a GALFORM catalogue of the same space density in the same cosmology (green line). Also shown (in red) is $r^2\xi(r)$ for the flux-limited SDSS main galaxy catalogue, which corresponds to the dotted lines in Figs. 4.10–4.13 showing the projected correlation function of the same sample. The black line shows $r^2\xi(r)$ for a sample of 2dFGRS galaxies in the *bin* of luminosity given in the legend.

projected correlation function of SDSS galaxies, while they use the abundance and radial distribution of satellite galaxies in the (b_J-selected) 2dFGRS. This may seem at odds with Tinker et al. (2006a), who show that in their HOD model the projected correlation function tightly constrains the satellite fraction. The answer may lie in the fact that their parametrized HOD, and our semi-analytic HOD, are unable to match the form of the HODs produced by the CLF approach, in which the parametrizations adopted for different parts of the CLF are a few steps removed from HOD parameters.

It would be exciting to conclude that there is a real difference between low-redshift estimates of σ_8 (e.g. from weak lensing) and estimates using CMB data, and that this indicates something about, say, evolving dark energy (e.g., Bartelmann et al., 2006). Other analyses find lower values, though, and there are still one or two concerns about our constraints. Our HODs are more ragged for our high $\Omega_{\rm m}$, low σ_8 GALFORM runs. As we hoped, a large part of our constraint comes from the intermediate-scale clustering for which halo-based models are most necessary, but this is affected by the scheme for placing galaxies within haloes. The largest difference between our high and low σ_8 models (and between our low σ_8 models and the data) is manifested at small scales.

It is possible that incorrect galaxy colours in GALFORM could bias our constraint. For example, while we see in Fig. 4.22 that a SDSS sample of given space density is more clustered than a comparable 2dFGRS sample (note, to see this, that the volume-limited sample used for our constraints is more clustered than the flux-limited sample of Fig. 4.22, as one can see by comparing the solid and dotted black lines of Figs. 4.10–4.13), an r-selected GALFORM sample has similar clustering to a CLF sample with similar space density, the CLF being calibrated via the b_J-selected 2dFGRS. If red GALFORM galaxies do not show a sufficient excess of clustering over blue GALFORM galaxies then using an r-selected sample might be expected to give higher σ_8 than using a b_J-selected sample.

As we show in Figs. 4.14–4.17, while GALFORM does a reasonable job of matching the luminosity-dependent clustering in the SDSS for samples of intermediate luminosity, the overall trend in the SDSS is linear for all luminosities considered, while in our models the correlation length r_0 exhibits a minimum near the space density we use for our cosmological constraints. While one could argue that it is these intermediate luminosity galaxies that GALFORM describe best (since it is constrained to agree with the data near the 'knee' in the luminosity function, and drifts off for very faint and very bright galaxies), it must be worrying that very faint or very bright samples would return a lower value of σ_8, since the model predicts relatively high bias for these samples. Halo assembly bias also acts in

the sense that it biases our estimate for σ_8 upwards. While we find it is a small effect in the model used in Chapter 3, other semi-analytic models may be more severely affected.

While bearing the above caveats in mind, we would still like to emphasize the tight constraints available in principle using our technique. We would also note that other constraints using galaxy data alone, which at first sight seem inconsistent with ours, use different techniques or different data or both. Many other studies which attempt to constrain σ_8 independently of CMB data (notably weak lensing) arrive at values consistent with ours. All the techniques, including those which make use of CMB data, suffer from systematic errors of some kind, the treatment of which may vary with time or between authors. It is always valuable, therefore, to develop new techniques in which, at the very least, the systematic errors are different or can be alleviated in different ways.

Chapter 5 | *Conclusions*

5.1 Environmental dependence

5.1.1 Haloes

In Chapter 2 we looked for evidence of an environmental dependence of halo formation times, using what we consider to be an especially sensitive test, and using a very large simulation which offers excellent statistical power when constraining the properties of haloes with a large range of mass. We have very strong evidence that haloes of a given mass in denser regions formed at higher redshift than those in less dense regions. This result is robust to changes in the mark used as a proxy for formation redshift, and we conclude that the observed dependence is not affected by systematic bias from averaging over a range of halo mass. Our conclusions are also unaffected by the precise definition of the halo catalogue or by the details of the construction of the merger trees.

Separating the haloes for which we wish to measure environment from those used to define environment allows us to look for the origin of the signal in more detail. We see a stronger dependence on environment for low mass haloes, although the effect is still present when more massive haloes are considered. We also note that in this context it only makes sense if the environment of low mass haloes is traced by a population of higher mass haloes. Using numerous, low mass haloes to trace the environment of more massive haloes means that our definition of environment may no longer correspond to an intuitive definition, in that it may no longer be the case that a relatively large number of close neighbours implies a relatively dense environment.

If we revert to a more intuitive test of the dependence of formation time on environment, and look at the mean formation redshift of haloes of a given mass as a function of the local overdensity in dark natter, we note that the size and resolution of the Millennium Simulation allows us to see a highly significant signal of environmental dependence for haloes with a wide range in mass, but again especially for low mass haloes. We are able to perform this test for haloes which we expect to host only a single, bright galaxy, since the

progenitors of these haloes are well resolved. The size of the variation in mean formation redshift is smaller than the (large) dispersion in formation redshift for haloes residing in a region of given overdensity. This makes the impact of this dependence on statistics such as the galaxy correlation function unclear, though this effect is studied in more detail by Gao et al. (2005) (who used the same simulation but different merger trees) where the age dependence of halo clustering is studied and a significant signal is observed. We show that the results of Gao et al. (2005) are reproduced using our trees. This motivates our study of environmental dependence of semi-analytic galaxy populations in Chapter 3.

Our purely dark matter results have, in any case, some implications for galaxy formation models and for halo models of clustering. Any simple version of the halo occupation distribution formalism, for example, has as one of its basic assumptions that knowing the mass of a halo is sufficient to statistically determine the properties of its galaxy population. So long as the properties of the galaxy population depend sufficiently strongly on the merger history of a halo, we see that this assumption is no longer strictly valid, and this therefore calls into question the validity of results based on this formalism. In particular, this is clearly of concern for our attempt to constrain cosmological parameters in Chapter 4.

While we see that extended Press-Schechter theory does a reasonable job of predicting the distribution of halo formation redshifts when averaging over haloes in all environments, it also predicts that the formation history is independent of environment, though, e.g., Sandvik et al. (2006) have attempted to explain why the clustering of haloes depends on their formation history within the framework of the excursion set formalism. We clearly see that it is not the case that halo formation history is independent of environment, so the practice of assigning a Monte Carlo merger tree constructed according to extended Press-Schechter theory to a simulated halo based only on the halo mass is called into question. The magnitude of this effect on any observables drawn from mock galaxy catalogues generated by semi-analytic models using these merger trees is unclear from our pure dark matter results. A comparison between catalogues produced using Monte Carlo merger trees and those produced using trees extracted directly from the simulation appears promising, but other aspects of the trees also differ. We therefore approach the problem through the shuffling method described in Chapter 3, which has become feasible with the advent of simulations with the resolution and volume of the Millennium Simulation.

5.1.2 Model galaxies

Even given the environmental effects on halo properties, it may still be the case that the width of the distribution of formation redshifts in a given environment, and the scatter in other relations such as the halo mass - central galaxy luminosity relation, wash out this effect in the galaxy population. Uncertainties in the galaxy formation models themselves could prove to have a more important contribution. Equally, though, if other halo properties such as the concentration and angular momentum depend strongly enough on formation time and environment, then this may help the models to better match and explain observations of the environmental dependence of galaxy colour and morphology, or the concentration or velocity profiles of galaxies of different ages. We have attempted to start addressing these issues in Chapter 3, though our focus is on the clustering statistics we use subsequently.

We have taken a recent semi-analytic model, designed to use the N-body merger trees which should fully capture the effects of environment, and then explicitly removed their environmental dependence by applying a shuffling algorithm. We show that the changes in the merger trees do indeed have a small effect on the galaxy correlation function, and we show the root of this effect in the way the HOD changes with halo environment. We have shown that modelling the effect on the HOD could help to adjust clustering statistics — in particular the two-point correlation function and the void probability function — produced by models with Monte Carlo trees so that they match statistics produced by models with N-body trees. The small size of the corrections and the uncertainties involved mean, though, that we prefer not to apply this correction when we use these models to try to constrain cosmological parameters in Chapter 4. We have, however, checked that applying such a correction does not change the conclusions of Chapter 4 in any substantial way. We also conclude that modelling the small scale clustering, which is affected by how galaxies are positioned within haloes, is at least as important as accounting for halo assembly bias in matching the observed galaxy correlation function.

5.2 Cosmological constraints

We have tried to use our knowledge of how galaxy formation and large scale structure are linked to improve the constraints we can impose on cosmological parameters from measurements of galaxy clustering. In particular, we connect the two through the technique of semi-analytic modelling, in which we try to predict the properties of the galaxy popula-

tion on a halo-by-halo basis. If we can predict the galaxy content of any dark matter halo then, in conjunction with dark matter simulations, we can completely specify the galaxy clustering in any given cosmology. This allows us to constrain the amplitude of the initial power spectrum σ_8 using galaxy clustering data, independently of other datasets such as the CMB.

We have compared the SDSS projected two-point correlation function at a galaxy space density $\bar{n}_{\rm g} = 0.00308\ h^3\ {\rm Mpc}^{-3}$ to a suite of populated simulations generated using the N-body code GADGET2 and the semi-analytic code GALFORM. Because we require N-body data in a great number of different cosmologies, we have relabelled and rescaled some simulation outputs as described in Appendix A to avoid the need to run a full simulation for each cosmology in our grid. The galaxy catalogues are self-consistent, GALFORM being run afresh for each cosmology we study.

We have attempted to estimate the systematic error in our value of σ_8 due to the particular choice of semi-analytic model by running three different GALFORM variants in each cosmology. For each of these variants we generate a catalogue in which the GALFORM parameters are adjusted to match the SDSS ${}^{0.1}r$-band luminosity function and a catalogue in which the parameters take the same values as they take in the $(\Omega_{\rm m}, \sigma_8) = (0.3, 0.8)$ cosmology. Combining our estimate of this systematic error with the formal statistical error gives the result $\sigma_8 = 0.96 \pm 0.05$. This constraint is impressively tight, given we have attempted to narrow the range of assumptions we require to produce an estimate of σ_8 by using only one well-understood, low redshift dataset. It is particularly interesting to obtain a constraint that is independent of CMB data. By choosing grids of cosmologies which lie on cluster-normalized curves, $\sigma_8 \Omega_{\rm m}^{0.5} = {\rm const.}$ we have shown that the degeneracies inherent in our approach are different to those inherent in cosmic shear measurements, which provide an important low-redshift constraint on $\Omega_{\rm m}$ and σ_8. In fact our method gives an almost pure constraint on σ_8. We have shown that in our model, the so-called halo assembly bias does not severely affect our constraint on σ_8, though this may not be universally the case for other semi-analytic codes. If it were not the case, we would expect it to bias our estimate of σ_8 high.

We recognise that our estimate of σ_8 looks high compared to the values obtained by WMAP, and even high compared to the results of weak lensing observations, which already cause some tension with CMB measurements. Small and intermediate scales in the correlation function contribute strongly to χ^2 and hence to our constraint on σ_8, and yet are not as well understood as the large scales. This is clearly an area where

further modelling effort is required. Moreover, we will not be completely assured that semi-analytic models capture the phenomenology of the galaxy population sufficiently well for high precision cosmological constraints until they are able to match the observed colour- and luminosity-dependent clustering of galaxies. The models need to be able to reproduce the properties of the observed galaxy population on a halo-by-halo basis, not just the properties averaged spatially or over luminosity.

The advent of halo-based methods of analysing redshift surveys should increase the ability of semi-analytic modellers to constrain the galaxy populations produced by their models halo-by-halo. One such approach is the conditional luminosity function (CLF) approach. We have compared our constraints on σ_8 to those obtained using a CLF approach by van den Bosch et al. (2005). The comparison is particularly interesting because we both use only galaxy clustering data. They conclude, though, that their models favour a low value of σ_8 in agreement with that favoured by WMAP. The differences in our parameter constraints could be driven by differences between the datasets we analyse. Whether this is the case will not be totally clear until there is a self-consistent model which can be measured up against their observables and ours in a range of different cosmologies.

We have highlighted the impressively small formal, statistical errors on σ_8 attainable using only galaxy clustering data. This potential highlights the importance of further improving our modelling. To eliminate doubts about the effect of halo assembly bias, we would ideally have a high resolution N-body simulation for each cosmology we consider, in order for each halo to be furnished with a merger tree that incorporates environmental dependence and does not suffer the limitations of trees generated using extended Press-Schechter theory. It is less clear how to tame the fearsome complexity of all the physics involved in the formation and evolution of galaxies. If nothing else, though, to obtain cosmological parameter constraints we require a good phenomenological model that predicts the galaxy population of a halo with a given merger tree. To use the full range of clustering data, it is particularly important to be able to predict the location of a galaxy within its parent halo. With all the above in place, we would be in a position not only to constrain the parameters of ΛCDM, but to demonstrate the consistency and correctness, or otherwise, of the ΛCDM cosmogony itself. Conversely, if cosmological parameters can be tightly constrained by other techniques, it is clear that measurements of galaxy clustering will continue to provide stringent tests of models for galaxy formation.

Bibliography

Aarseth, S. J.: 1963, *MNRAS* **126**, 223

Abazajian, K., Zheng, Z., Zehavi, I., Weinberg, D. H., Frieman, J. A., Berlind, A. A., Blanton, M. R., Bahcall, N. A., Brinkmann, J., Schneider, D. P., & Tegmark, M.: 2005, *ApJ* **625**, 613

Abbas, U. & Sheth, R. K.: 2005, *MNRAS* **364**, 1327

Alcock, C. & Paczynski, B.: 1979, *Nature* **281**, 358

Alpher, R. A., Bethe, H., & Gamow, G.: 1948, *Phys. Rev.* **73**, 803

Amosov, G. & Schuecker, P.: 2004, *A&A* **421**, 425

Astier, P., Guy, J., Regnault, N., Pain, R., Aubourg, E., Balam, D., Basa, S., Carlberg, R. G., Fabbro, S., Fouchez, D., Hook, I. M., Howell, D. A., Lafoux, H., Neill, J. D., Palanque-Delabrouille, N., Perrett, K., Pritchet, C. J., Rich, J., Sullivan, M., Taillet, R., Aldering, G., Antilogus, P., Arsenijevic, V., Balland, C., Baumont, S., Bronder, J., Courtois, H., Ellis, R. S., Filiol, M., Gonçalves, A. C., Goobar, A., Guide, D., Hardin, D., Lusset, V., Lidman, C., McMahon, R., Mouchet, M., Mourao, A., Perlmutter, S., Ripoche, P., Tao, C., & Walton, N.: 2006, *A&A* **447**, 31

Avila-Reese, V., Colín, P., Gottlöber, S., Firmani, C., & Maulbetsch, C.: 2005, *ApJ* **634**, 51

Balogh, M., Eke, V., Miller, C., Lewis, I., Bower, R., Couch, W., Nichol, R., & the 2dFGRS team: 2004, *MNRAS* **348**, 1355

Bardeen, J. M., Bond, J. R., Kaiser, N., & Szalay, A. S.: 1986, *ApJ* **304**, 15

Bartelmann, M., Doran, M., & Wetterich, C.: 2006, *A&A* **454**, 27

Baugh, C. M., Lacey, C. G., Frenk, C. S., Granato, G. L., Silva, L., Bressan, A., Benson, A. J., & Cole, S.: 2005, *MNRAS* **356**, 1191

Beisbart, C. & Kerscher, M.: 2000, *ApJ* **545**, 6

Bekenstein, J. D.: 2004, *Phys. Rev. D* **70(8)**, 083509

Bennett, C. L., Banday, A. J., Gorski, K. M., Hinshaw, G., Jackson, P., Keegstra, P., Kogut, A., Smoot, G. F., Wilkinson, D. T., & Wright, E. L.: 1996, *ApJL* **464**, L1+

Benson, A. J., Bower, R. G., Frenk, C. S., Lacey, C. G., Baugh, C. M., & Cole, S.: 2003, *ApJ* **599**, 38

Benson, A. J., Cole, S., Frenk, C. S., Baugh, C. M., & Lacey, C. G.: 2000, *MNRAS* **311**, 793

Benson, A. J., Kamionkowski, M., & Hassani, S. H.: 2005, *MNRAS* **357**, 847

Benson, A. J., Lacey, C. G., Baugh, C. M., Cole, S., & Frenk, C. S.: 2002, *MNRAS* **333**, 156

Berlind, A. A. & Weinberg, D. H.: 2002, *ApJ* **575**, 587

Berlind, A. A., Weinberg, D. H., Benson, A. J., Baugh, C. M., Cole, S., Davé, R., Frenk, C. S., Jenkins, A., Katz, N., & Lacey, C. G.: 2003, *ApJ* **593**, 1

Bertschinger, E.: 1998, *ARA&A* **36**, 599

Blanton, M. R., Brinkmann, J., Csabai, I., Doi, M., Eisenstein, D., Fukugita, M., Gunn, J. E., Hogg, D. W., & Schlegel, D. J.: 2003a, *AJ* **125**, 2348

Blanton, M. R., Eisenstein, D., Hogg, D. W., & Zehavi, I.: 2006, *ApJ* **645**, 977

Blanton, M. R., Hogg, D. W., Bahcall, N. A., Brinkmann, J., Britton, M., Connolly, A. J., Csabai, I., Fukugita, M., Loveday, J., Meiksin, A., Munn, J. A., Nichol, R. C., Okamura, S., Quinn, T., Schneider, D. P., Shimasaku, K., Strauss, M. A., Tegmark, M., Vogeley, M. S., & Weinberg, D. H.: 2003b, *ApJ* **592**, 819

Boerner, G., Mo, H., & Zhou, Y.: 1989, *A&A* **221**, 191

Bond, J. R., Cole, S., Efstathiou, G., & Kaiser, N.: 1991, *ApJ* **379**, 440

Bond, J. R. & Efstathiou, G.: 1987, *MNRAS* **226**, 655

Bosma, A.: 1978, *Ph.D. Thesis*

Bower, R. G.: 1991, *MNRAS* **248**, 332

Bower, R. G., Benson, A. J., Malbon, R., Helly, J. C., Frenk, C. S., Baugh, C. M., Cole, S., & Lacey, C. G.: 2006, *MNRAS* **370**, 645

Bower, R. G., Coles, P., Frenk, C. S., & White, S. D. M.: 1993, *ApJ* **405**, 403

Burles, S., Nollett, K. M., & Turner, M. S.: 2001, *Phys. Rev. D* **63(6)**, 063512

Chandrasekhar, S.: 1943, *Rev. Mod. Phys.* **15**, 1

Clowe, D., Bradač, M., Gonzalez, A. H., Markevitch, M., Randall, S. W., Jones, C., & Zaritsky, D.: 2006, *ApJL* **648**, L109

Cole, S.: 1991, *ApJ* **367**, 45

Cole, S., Aragon-Salamanca, A., Frenk, C. S., Navarro, J. F., & Zepf, S. E.: 1994a, *MNRAS* **271**, 781

Cole, S., Fisher, K. B., & Weinberg, D. H.: 1994b, *MNRAS* **267**, 785

Cole, S. & Kaiser, N.: 1989, *MNRAS* **237**, 1127

Cole, S. & Lacey, C.: 1996, *MNRAS* **281**, 716

Cole, S., Lacey, C. G., Baugh, C. M., & Frenk, C. S.: 2000, *MNRAS* **319**, 168

Cole, S., Percival, W. J., Peacock, J. A., Norberg, P., Baugh, C. M., Frenk, C. S., Baldry, I., Bland-Hawthorn, J., Bridges, T., Cannon, R., Colless, M., Collins, C., Couch, W., Cross, N. J. G., Dalton, G., Eke, V. R., De Propris, R., Driver, S. P., Efstathiou, G., Ellis, R. S., Glazebrook, K., Jackson, C., Jenkins, A., Lahav, O., Lewis, I., Lumsden, S., Maddox, S., Madgwick, D., Peterson, B. A., Sutherland, W., & Taylor, K.: 2005, *MNRAS* **362**, 505

Coles, P.: 1993, *MNRAS* **262**, 1065

Colless, M., Dalton, G., Maddox, S., Sutherland, W., Norberg, P., Cole, S., Bland-Hawthorn, J., Bridges, T., Cannon, R., Collins, C., Couch, W., Cross, N., Deeley, K., De Propris, R., Driver, S. P., Efstathiou, G., Ellis, R. S., Frenk, C. S., Glazebrook, K., Jackson, C., Lahav, O., Lewis, I., Lumsden, S., Madgwick, D., Peacock, J. A., Peterson, B. A., Price, I., Seaborne, M., & Taylor, K.: 2001, *MNRAS* **328**, 1039

Cooray, A.: 2006, *astro-ph/0601090*

Cooray, A. & Sheth, R.: 2002, *Physics Reports* **372**, 1

Croft, R. A. C., Weinberg, D. H., Katz, N., & Hernquist, L.: 1998, *ApJ* **495**, 44

Croton, D. J., Gao, L., & White, S. D. M.: 2006a, *MNRAS, submitted (astro-ph/0605636)*

Croton, D. J., Springel, V., White, S. D. M., De Lucia, G., Frenk, C. S., Gao, L., Jenkins, A., Kauffmann, G., Navarro, J. F., & Yoshida, N.: 2006b, *MNRAS* **365**, 11

Davis, M., Efstathiou, G., Frenk, C. S., & White, S. D. M.: 1985, *ApJ* **292**, 371

Davis, M. & Peebles, P. J. E.: 1983, *ApJ* **267**, 465

de Bernardis, P., Ade, P. A. R., Bock, J. J., Bond, J. R., Borrill, J., Boscaleri, A., Coble, K., Crill, B. P., De Gasperis, G., Farese, P. C., Ferreira, P. G., Ganga, K., Giacometti, M., Hivon, E., Hristov, V. V., Iacoangeli, A., Jaffe, A. H., Lange, A. E., Martinis, L., Masi, S., Mason, P. V., Mauskopf, P. D., Melchiorri, A., Miglio, L., Montroy, T., Netterfield, C. B., Pascale, E., Piacentini, F., Pogosyan, D., Prunet, S., Rao, S., Romeo, G., Ruhl, J. E., Scaramuzzi, F., Sforna, D., & Vittorio, N.: 2000, *Nature* **404**, 955

De Lucia, G., Springel, V., White, S. D. M., Croton, D., & Kauffmann, G.: 2006, *MNRAS* **366**, 499

Del Popolo, A.: 2006, *AJ* **131**, 2367

Dicke, R. H., Peebles, P. J. E., Roll, P. G., & Wilkinson, D. T.: 1965, *ApJ* **142**, 414

Dressler, A.: 1980, *ApJ* **236**, 351

Efstathiou, G. & Eastwood, J. W.: 1981, *MNRAS* **194**, 503

Efstathiou, G., Moody, S., Peacock, J. A., Percival, W. J., Baugh, C., Bland-Hawthorn, J., Bridges, T., Cannon, R., Cole, S., Colless, M., Collins, C., Couch, W., Dalton, G., de Propris, R., Driver, S. P., Ellis, R. S., Frenk, C. S., Glazebrook, K., Jackson, C., Lahav, O., Lewis, I., Lumsden, S., Maddox, S., Norberg, P., Peterson, B. A., Sutherland, W., & Taylor, K.: 2002, *MNRAS* **330**, L29

Eisenstein, D. J. & Hu, W.: 1998, *ApJ* **496**, 605

Eisenstein, D. J. & Hu, W.: 1999, *ApJ* **511**, 5

Eisenstein, D. J., Zehavi, I., Hogg, D. W., Scoccimarro, R., Blanton, M. R., Nichol, R. C., Scranton, R., Seo, H.-J., Tegmark, M., Zheng, Z., Anderson, S. F., Annis, J., Bahcall, N., Brinkmann, J., Burles, S., Castander, F. J., Connolly, A., Csabai, I., Doi, M., Fukugita, M., Frieman, J. A., Glazebrook, K., Gunn, J. E., Hendry, J. S., Hennessy, G., Ivezić, Z., Kent, S., Knapp, G. R., Lin, H., Loh, Y.-S., Lupton, R. H., Margon, B., McKay, T. A., Meiksin, A., Munn, J. A., Pope, A., Richmond, M. W., Schlegel, D., Schneider, D. P., Shimasaku, K., Stoughton, C., Strauss, M. A., SubbaRao, M., Szalay, A. S., Szapudi, I., Tucker, D. L., Yanny, B., & York, D. G.: 2005, *ApJ* **633**, 560

Eke, V. R., Baugh, C. M., Cole, S., Frenk, C. S., King, H. M., & Peacock, J. A.: 2005, *MNRAS* **362**, 1233

Eke, V. R., Cole, S., & Frenk, C. S.: 1996, *MNRAS* **282**, 263

Faltenbacher, A., Gottlöber, S., Kerscher, M., & Müller, V.: 2002, *A&A* **395**, 1

Fixsen, D. J., Cheng, E. S., Gales, J. M., Mather, J. C., Shafer, R. A., & Wright, E. L.: 1996, *ApJ* **473**, 576

Freedman, W. L., Madore, B. F., Gibson, B. K., Ferrarese, L., Kelson, D. D., Sakai, S., Mould, J. R., Kennicutt, Jr., R. C., Ford, H. C., Graham, J. A., Huchra, J. P., Hughes, S. M. G., Illingworth, G. D., Macri, L. M., & Stetson, P. B.: 2001, *ApJ* **553**, 47

Frenk, C. S., White, S. D. M., Davis, M., & Efstathiou, G.: 1988, *ApJ* **327**, 507

Furlanetto, S. R. & Piran, T.: 2006, *MNRAS* **366**, 467

Gómez, P. L., Nichol, R. C., Miller, C. J., Balogh, M. L., Goto, T., Zabludoff, A. I., Romer, A. K., Bernardi, M., Sheth, R., Hopkins, A. M., Castander, F. J., Connolly, A. J., Schneider, D. P., Brinkmann, J., Lamb, D. Q., SubbaRao, M., & York, D. G.: 2003, *ApJ* **584**, 210

Gamow, G.: 1948, *Phys. Rev.* **74**, 505

Gao, L., Springel, V., & White, S. D. M.: 2005, *MNRAS* **363**, L66

Gaztañaga, E. & Scoccimarro, R.: 2005, *MNRAS* **361**, 824

Gottlöber, S., Łokas, E. L., Klypin, A., & Hoffman, Y.: 2003, *MNRAS* **344**, 715

Gottlöber, S., Kerscher, M., Kravtsov, A. V., Faltenbacher, A., Klypin, A., & Müller, V.: 2002, *A&A* **387**, 778

Gunn, J. E. & Gott, J. R. I.: 1972, *ApJ* **176**, 1

Guth, A. H.: 1981, *Phys. Rev. D* **23**, 347

Hanany, S., Ade, P., Balbi, A., Bock, J., Borrill, J., Boscaleri, A., de Bernardis, P., Ferreira, P. G., Hristov, V. V., Jaffe, A. H., Lange, A. E., Lee, A. T., Mauskopf, P. D., Netterfield, C. B., Oh, S., Pascale, E., Rabii, B., Richards, P. L., Smoot, G. F., Stompor, R., Winant, C. D., & Wu, J. H. P.: 2000, *ApJL* **545**, L5

Harrison, E. R.: 1970, *Phys. Rev. D* **1**, 2726

Helly, J. C., Cole, S., Frenk, C. S., Baugh, C. M., Benson, A., & Lacey, C.: 2003a, *MNRAS* **338**, 903

Helly, J. C., Cole, S., Frenk, C. S., Baugh, C. M., Benson, A., Lacey, C., & Pearce, F. R.: 2003b, *MNRAS* **338**, 913

Heymans, C., Brown, M. L., Barden, M., Caldwell, J. A. R., Jahnke, K., Peng, C. Y., Rix, H.-W., Taylor, A., Beckwith, S. V. W., Bell, E. F., Borch, A., Häußler, B., Jogee, S., McIntosh, D. H., Meisenheimer, K., Sánchez, S. F., Somerville, R., Wisotzki, L., & Wolf, C.: 2005, *MNRAS* **361**, 160

Hinshaw, G., Nolta, M. R., Bennett, C. L., Bean, R., Dore', O., Greason, M. R., Halpern, M., Hill, R. S., Jarosik, N., Kogut, A., Komatsu, E., Limon, M., Odegard, N., Meyer, S. S., Page, L., Peiris, H. V., Spergel, D. N., Tucker, G. S., Verde, L., Weiland, J. L., Wollack, E., & Wright, E. L.: 2006, *ApJ, submitted (astro-ph/0603451)*

Hoekstra, H., Mellier, Y., van Waerbeke, L., Semboloni, E., Fu, L., Hudson, M. J., Parker, L. C., Tereno, I., & Benabed, K.: 2006, *ApJ* **647**, 116

Hoyle, F. & Vogeley, M. S.: 2004, *ApJ* **607**, 751

Hu, W. & Dodelson, S.: 2002, *ARA&A* **40**, 171

Hubble, E.: 1929, *P. Natl. Acad. Sci. USA* **15**, 168

Jarosik, N., Barnes, C., Greason, M. R., Hill, R. S., Nolta, M. R., Odegard, N., Weiland, J. L., Bean, R., Bennett, C. L., Dore', O., Halpern, M., Hinshaw, G., Kogut, A., Komatsu, E., Limon, M., Meyer, S. S., Page, L., Spergel, D. N., Tucker, G. S., Wollack, E., & Wright, E. L.: 2006, *ApJ, submitted (astro-ph/0603432)*

Jarvis, M., Jain, B., Bernstein, G., & Dolney, D.: 2006, *ApJ* **644**, 71

Jassal, H. K., Bagla, J. S., & Padmanabhan, T.: 2005, *Phys. Rev. D* **72(10)**, 103503

Jena, T., Norman, M. L., Tytler, D., Kirkman, D., Suzuki, N., Chapman, A., Melis, C., Paschos, P., O'Shea, B., So, G., Lubin, D., Lin, W.-C., Reimers, D., Janknecht, E., & Fechner, C.: 2005, *MNRAS* **361**, 70

Jenkins, A., Frenk, C. S., Pearce, F. R., Thomas, P. A., Colberg, J. M., White, S. D. M., Couchman, H. M. P., Peacock, J. A., Efstathiou, G., & Nelson, A. H.: 1998, *ApJ* **499**, 20

Jenkins, A., Frenk, C. S., White, S. D. M., Colberg, J. M., Cole, S., Evrard, A. E., Couchman, H. M. P., & Yoshida, N.: 2001, *MNRAS* **321**, 372

Jing, Y. P. & Börner, G.: 2004, *ApJ* **617**, 782

Kaiser, N.: 1984, *ApJL* **284**, L9

Kaiser, N.: 1987, MNRAS **227**, 1

Kauffmann, G., Colberg, J. M., Diaferio, A., & White, S. D. M.: 1999, *MNRAS* **303**, 188

Kauffmann, G., White, S. D. M., & Guiderdoni, B.: 1993, *MNRAS* **264**, 201

Knop, R. A., Aldering, G., Amanullah, R., Astier, P., Blanc, G., Burns, M. S., Conley, A., Deustua, S. E., Doi, M., Ellis, R., Fabbro, S., Folatelli, G., Fruchter, A. S., Garavini, G., Garmond, S., Garton, K., Gibbons, R., Goldhaber, G., Goobar, A., Groom, D. E., Hardin, D., Hook, I., Howell, D. A., Kim, A. G., Lee, B. C., Lidman, C., Mendez, J., Nobili, S., Nugent, P. E., Pain, R., Panagia, N., Pennypacker, C. R., Perlmutter, S., Quimby, R., Raux, J., Regnault, N., Ruiz-Lapuente, P., Sainton, G., Schaefer, B., Schahmaneche, K., Smith, E., Spadafora, A. L., Stanishev, V., Sullivan, M., Walton, N. A., Wang, L., Wood-Vasey, W. M., & Yasuda, N.: 2003, *ApJ* **598**, 102

Kravtsov, A. V., Berlind, A. A., Wechsler, R. H., Klypin, A. A., Gottlöber, S., Allgood, B., & Primack, J. R.: 2004, *ApJ* **609**, 35

Lacey, C. & Cole, S.: 1993, *MNRAS* **262**, 627

Lacey, C. & Cole, S.: 1994, *MNRAS* **271**, 676

Lacey, C. & Silk, J.: 1991, *ApJ* **381**, 14

Lahav, O., Lilje, P. B., Primack, J. R., & Rees, M. J.: 1991, *MNRAS* **251**, 128

Landy, S. D. & Szalay, A. S.: 1993, *ApJ* **412**, 64

Leitch, E. M., Kovac, J. M., Halverson, N. W., Carlstrom, J. E., Pryke, C., & Smith, M. W. E.: 2005, *ApJ* **624**, 10

Lemson, G. & Kauffmann, G.: 1999, *MNRAS* **302**, 111

Li, Y., Mo, H. J., & van den Bosch, F. C.: 2005, *MNRAS, submitted (astro-ph/0510372)*

Linde, A. D.: 1982, *Phys. Lett. B* **108**, 389

Lynden-Bell, D.: 1967, *MNRAS* **136**, 101

Makino, J., Fukushige, T., Koga, M., & Namura, K.: 2003, *Publ. Astron. Soc. Japan* **55**, 1163

Marquardt, D. W.: 1963, *J. Soc. Ind. Appl. Math.* **11**, 431

Maulbetsch, C., Avila-Reese, V., Colin, P., Gottloeber, S., Khalatyan, A., & Steinmetz, M.: 2006, *ApJ, submitted (astro-ph/0606360)*

Mészáros, P.: 1974, *A&A* **37**, 225

Milgrom, M.: 1983, *ApJ* **270**, 365

Mo, H. J., Mao, S., & White, S. D. M.: 1999, *MNRAS* **304**, 175

Mo, H. J. & White, S. D. M.: 1996, *MNRAS* **282**, 347

Mo, H. J., Yang, X., van den Bosch, F. C., & Jing, Y. P.: 2004, *MNRAS* **349**, 205

Moffat, J. W.: 2006, *JCAP* **3**, 4

Monaghan, J. J. & Lattanzio, J. C.: 1985, *A&A* **149**, 135

Munshi, D. & Kilbinger, M.: 2006, *A&A* **452**, 63

Neistein, E., van den Bosch, F. C., & Dekel, A.: 2006, *MNRAS, submitted (astro-ph/0605045)*

Norman, M. L. & Bryan, G. L.: 1999, in S. M. Miyama, K. Tomisaka, & T. Hanawa (eds.), *ASSL Vol. 240: Numerical Astrophysics*, pp 19–+

O'Meara, J. M., Tytler, D., Kirkman, D., Suzuki, N., Prochaska, J. X., Lubin, D., & Wolfe, A. M.: 2001, *ApJ* **552**, 718

Page, L., Hinshaw, G., Komatsu, E., Nolta, M. R., Spergel, D. N., Bennett, C. L., Barnes, C., Bean, R., Dore', O., Halpern, M., Hill, R. S., Jarosik, N., Kogut, A., Limon, M., Meyer, S. S., Odegard, N., Peiris, H. V., Tucker, G. S., Verde, L., Weiland, J. L., Wollack, E., & Wright, E. L.: 2006, *ApJ, submitted (astro-ph/0603450)*

Peacock, J. A., Cole, S., Norberg, P., Baugh, C. M., Bland-Hawthorn, J., Bridges, T., Cannon, R. D., Colless, M., Collins, C., Couch, W., Dalton, G., Deeley, K., De Propris, R., Driver, S. P., Efstathiou, G., Ellis, R. S., Frenk, C. S., Glazebrook, K., Jackson, C., Lahav, O., Lewis, I., Lumsden, S., Maddox, S., Percival, W. J., Peterson, B. A., Price, I., Sutherland, W., & Taylor, K.: 2001, *Nature* **410**, 169

Peacock, J. A. & Dodds, S. J.: 1994, *MNRAS* **267**, 1020

Peebles, P. J. & Ratra, B.: 2003, *Rev. Mod. Phys.* **75**, 559

Peebles, P. J. E.: 1980, *The large-scale structure of the universe*, Princeton University Press

Peebles, P. J. E. & Yu, J. T.: 1970, *ApJ* **162**, 815

Penzias, A. A. & Wilson, R. W.: 1965, *ApJ* **142**, 419

Percival, W. J., Baugh, C. M., Bland-Hawthorn, J., Bridges, T., Cannon, R., Cole, S., Colless, M., Collins, C., Couch, W., Dalton, G., De Propris, R., Driver, S. P., Efstathiou, G., Ellis, R. S., Frenk, C. S., Glazebrook, K., Jackson, C., Lahav, O., Lewis, I., Lumsden, S., Maddox, S., Moody, S., Norberg, P., Peacock, J. A., Peterson, B. A., Sutherland, W., & Taylor, K.: 2001, *MNRAS* **327**, 1297

Perlmutter, S., Aldering, G., Goldhaber, G., Knop, R. A., Nugent, P., Castro, P. G., Deustua, S., Fabbro, S., Goobar, A., Groom, D. E., Hook, I. M., Kim, A. G., Kim, M. Y., Lee, J. C., Nunes, N. J., Pain, R., Pennypacker, C. R., Quimby, R., Lidman, C., Ellis, R. S., Irwin, M., McMahon, R. G., Ruiz-Lapuente, P., Walton, N., Schaefer, B., Boyle, B. J., Filippenko, A. V., Matheson, T., Fruchter, A. S., Panagia, N., Newberg, H. J. M., Couch, W. J., & The Supernova Cosmology Project: 1999, *ApJ* **517**, 565

Pierpaoli, E., Borgani, S., Scott, D., & White, M.: 2003, *MNRAS* **342**, 163

Plummer, H. C.: 1911, *MNRAS* **71**, 460

Postman, M. & Geller, M. J.: 1984, *ApJ* **281**, 95

Press, W. H. & Schechter, P.: 1974, *ApJ* **187**, 425

Press, W. H., Teukolsky, S. A., Vetterling, W. T., & Flannery, B. P.: 1992, *Numerical recipes in FORTRAN. The art of scientific computing*, Cambridge: University Press, —c1992, 2nd ed.

Rajguru, N., Myers, S. T., Battye, R. A., Bond, J. R., Cleary, K., Contaldi, C. R., Davies, R. D., Davis, R. J., Dickinson, C., Genova-Santos, R., Grainge, K., Hafez, Y. A., Hobson, M. P., Jones, M. E., Kneissl, R., Lancaster, K., Lasenby, A., Mason, B. S., Pearson, T. J., Pooley, G. G., Readhead, A. C. S., Rebolo, R., Rocha, G., Rubiño-Martin, J. A., Saunders, R. D. E., Savage, R. S., Scaife, A., Scott, P. F., Sievers, J. L., Slosar, A., Taylor, A. C., Titterington, D., Waldram, E., Watson, R. A., & Wilkinson, A.: 2005, *MNRAS* **363**, 1125

Rasia, E., Mazzotta, P., Borgani, S., Moscardini, L., Dolag, K., Tormen, G., Diaferio, A., & Murante, G.: 2005, *ApJL* **618**, L1

Reed, D., Governato, F., Quinn, T., Gardner, J., Stadel, J., & Lake, G.: 2005, *MNRAS* **359**, 1537

Reed, D. S., Governato, F., Quinn, T., Stadel, J., & Lake, G.: 2006, *MNRAS, submitted (astro-ph/0602003)*

Refregier, A.: 2003, *ARA&A* **41**, 645

Riess, A. G., Filippenko, A. V., Challis, P., Clocchiatti, A., Diercks, A., Garnavich, P. M., Gilliland, R. L., Hogan, C. J., Jha, S., Kirshner, R. P., Leibundgut, B., Phillips, M. M., Reiss, D., Schmidt, B. P., Schommer, R. A., Smith, R. C., Spyromilio, J., Stubbs, C., Suntzeff, N. B., & Tonry, J.: 1998, *AJ* **116**, 1009

Riess, A. G., Strolger, L.-G., Tonry, J., Casertano, S., Ferguson, H. C., Mobasher, B., Challis, P., Filippenko, A. V., Jha, S., Li, W., Chornock, R., Kirshner, R. P., Leibundgut, B., Dickinson, M., Livio, M., Giavalisco, M., Steidel, C. C., Benítez, T., & Tsvetanov, Z.: 2004, *ApJ* **607**, 665

Rubin, V. C., Thonnard, N., & Ford, Jr., W. K.: 1980, *ApJ* **238**, 471

Sachs, R. K. & Wolfe, A. M.: 1967, *ApJ* **147**, 73

Sandvik, H. B., Moeller, O., Lee, J., & White, S. D. M.: 2006, *astro-ph/0610172*

Schechter, P.: 1976, *ApJ* **203**, 297

Sefusatti, E., Crocce, M., Pueblas, S., & Scoccimarro, R.: 2006, *Phys. Rev. D* **74(2)**, 023522

Seljak, U.: 2000, *MNRAS* **318**, 203

Seljak, U., Makarov, A., Mandelbaum, R., Hirata, C. M., Padmanabhan, N., McDonald, P., Blanton, M. R., Tegmark, M., Bahcall, N. A., & Brinkmann, J.: 2005a, *Phys. Rev. D* **71(4)**, 043511

Seljak, U., Makarov, A., McDonald, P., Anderson, S. F., Bahcall, N. A., Brinkmann, J., Burles, S., Cen, R., Doi, M., Gunn, J. E., Ivezić, Ž., Kent, S., Loveday, J., Lupton, R. H., Munn, J. A., Nichol, R. C., Ostriker, J. P., Schlegel, D. J., Schneider, D. P., Tegmark, M., Berk, D. E., Weinberg, D. H., & York, D. G.: 2005b, *Phys. Rev. D* **71(10)**, 103515

Seljak, U., Slosar, A., & McDonald, P.: 2006, *astro-ph/0604335*

Seljak, U. & Zaldarriaga, M.: 1996, *ApJ* **469**, 437

Semboloni, E., Mellier, Y., van Waerbeke, L., Hoekstra, H., Tereno, I., Benabed, K., Gwyn, S. D. J., Fu, L., Hudson, M. J., Maoli, R., & Parker, L. C.: 2006, *A&A* **452**, 51

Shen, J., Abel, T., Mo, H. J., & Sheth, R. K.: 2006, *ApJ* **645**, 783

Sheth, R. K.: 2005, *MNRAS* **364**, 796

Sheth, R. K., Connolly, A. J., & Skibba, R.: 2005, *MNRAS, submitted (astro-ph/0511773)*

Sheth, R. K. & Lemson, G.: 1999, *MNRAS* **305**, 946

Sheth, R. K., Mo, H. J., & Tormen, G.: 2001, *MNRAS* **323**, 1

Sheth, R. K. & Tormen, G.: 2002, *MNRAS* **329**, 61

Sheth, R. K. & Tormen, G.: 2004a, *MNRAS* **349**, 1464

Sheth, R. K. & Tormen, G.: 2004b, *MNRAS* **350**, 1385

Sheth, R. K. & van de Weygaert, R.: 2004, *MNRAS* **350**, 517

Silk, J.: 1968, *ApJ* **151**, 459

Sirko, E.: 2005, *ApJ* **634**, 728

Skibba, R., Sheth, R. K., Connolly, A. J., & Scranton, R.: 2006, *MNRAS* **369**, 68

Smith, R. E., Peacock, J. A., Jenkins, A., White, S. D. M., Frenk, C. S., Pearce, F. R., Thomas, P. A., Efstathiou, G., & Couchman, H. M. P.: 2003, *MNRAS* **341**, 1311

Smoluchowski, M. V.: 1916, *Zeitschrift fur Physik* **17**, 557

Smoot, G. F., Bennett, C. L., Kogut, A., Wright, E. L., Aymon, J., Boggess, N. W., Cheng, E. S., de Amici, G., Gulkis, S., Hauser, M. G., Hinshaw, G., Jackson, P. D., Janssen, M., Kaita, E., Kelsall, T., Keegstra, P., Lineweaver, C., Loewenstein, K., Lubin, P., Mather, J., Meyer, S. S., Moseley, S. H., Murdock, T., Rokke, L., Silverberg, R. F., Tenorio, L., Weiss, R., & Wilkinson, D. T.: 1992, *ApJL* **396**, L1

Somerville, R. S. & Kolatt, T. S.: 1999, *MNRAS* **305**, 1

Somerville, R. S. & Primack, J. R.: 1999, *MNRAS* **310**, 1087

Spergel, D. N., Bean, R., Dore', O., Nolta, M. R., Bennett, C. L., Hinshaw, G., Jarosik, N., Komatsu, E., Page, L., Peiris, H. V., Verde, L., Barnes, C., Halpern, M., Hill, R. S., Kogut, A., Limon, M., Meyer, S. S., Odegard, N., Tucker, G. S., Weiland, J. L., Wollack, E., & Wright, E. L.: 2006, *ApJ, submitted (astro-ph/0603449)*

Springel, V.: 2005, *MNRAS* **364**, 1105

Springel, V., White, S. D. M., Jenkins, A., Frenk, C. S., Yoshida, N., Gao, L., Navarro, J., Thacker, R., Croton, D., Helly, J., Peacock, J. A., Cole, S., Thomas, P., Couchman, H., Evrard, A., Colberg, J., & Pearce, F.: 2005, *Nature* **435**, 629

Springel, V., White, S. D. M., Tormen, G., & Kauffmann, G.: 2001a, *MNRAS* **328**, 726

Springel, V., Yoshida, N., & White, S. D. M.: 2001b, *New Astronomy* **6**, 79

Stoyan, D. & Stoyan, H.: 1994, *Fractals, Random Shapes and Point Fields: Methods of Geometrical Statistics*, John Wiley & Sons

Sugiyama, N.: 1995, *ApJS* **100**, 281

Sunyaev, R. A. & Zel'dovich, Y. B.: 1970, *Astrophysics and Space Science* **7**, 3

Szapudi, I., Branchini, E., Frenk, C. S., Maddox, S., & Saunders, W.: 2000, *MNRAS* **318**, L45

Tegmark, M., Blanton, M. R., Strauss, M. A., Hoyle, F., Schlegel, D., Scoccimarro, R., Vogeley, M. S., Weinberg, D. H., Zehavi, I., Berlind, A., Budavari, T., Connolly, A., Eisenstein, D. J., Finkbeiner, D., Frieman, J. A., Gunn, J. E., Hamilton, A. J. S., Hui, L., Jain, B., Johnston, D., Kent, S., Lin, H., Nakajima, R., Nichol, R. C., Ostriker, J. P., Pope, A., Scranton, R., Seljak, U., Sheth, R. K., Stebbins, A., Szalay, A. S., Szapudi, I., Verde, L., Xu, Y., Annis, J., Bahcall, N. A., Brinkmann, J., Burles, S., Castander, F. J., Csabai, I., Loveday, J., Doi, M., Fukugita, M., Gott, J. R. I., Hennessy, G., Hogg, D. W., Ivezić, Ž., Knapp, G. R., Lamb, D. Q., Lee, B. C., Lupton, R. H., McKay, T. A., Kunszt, P., Munn, J. A., O'Connell, L., Peoples, J., Pier, J. R., Richmond, M., Rockosi, C., Schneider, D. P., Stoughton, C., Tucker, D. L., Vanden Berk, D. E., Yanny, B., & York, D. G.: 2004, *ApJ* **606**, 702

Tegmark, M., Eisenstein, D., Strauss, M., Weinberg, D., Blanton, M., Frieman, J., Fukugita, M., Gunn, J., Hamilton, A., Knapp, G., Nichol, R., Ostriker, J., Padmanabhan, N., Percival, W., Schlegel, D., Schneider, D., Scoccimarro, R., Seljak, U., Seo, H., Swanson, M., Szalay, A., Vogeley, M., Yoo, J., Zehavi, I., Abazajian, K., Anderson, S., Annis, J., Bahcall, N., Bassett, B., Berlind, A., Brinkmann, J., Budavari, T., Castander, F., Connolly, A., Csabai, I., Doi, M., Finkbeiner, D., Gillespie, B., Glazebrook, K., Hennessy, G., Hogg, D., Ivezic, Z., Jain, B., Johnston, D., Kent, S., Lamb, D., Lee, B., Lin, H., Loveday, J., Lupton, R., Munn, J., Pan, K., Park, C., Peoples, J., Pier, J., Pope, A., Richmond, M., Rockosi, C., Scranton, R., Sheth, R., Stebbins, A., Stoughton, C., Szapudi, I., Tucker, D., Vanden Berk, D., Yanny, B., & York, D.: 2006, *astro-ph/0608632*

Tereno, I., Doré, O., van Waerbeke, L., & Mellier, Y.: 2005, *A&A* **429**, 383

Tinker, J. L., Weinberg, D. H., & Warren, M. S.: 2006a, ApJ **647**, 737

Tinker, J. L., Weinberg, D. H., & Zheng, Z.: 2006b, *MNRAS* **368**, 85

Tinker, J. L., Weinberg, D. H., Zheng, Z., & Zehavi, I.: 2005, *ApJ* **631**, 41

Tully, R. B. & Fisher, J. R.: 1977, *A&A* **54**, 661

van den Bosch, F. C., Yang, X., Mo, H. J., & Norberg, P.: 2005, *MNRAS* **356**, 1233

Weinberg, S.: 1972, *Gravitation and Cosmology: Principles and Applications of the General Theory of Relativity*, Wiley

Weinmann, S. M., van den Bosch, F. C., Yang, X., & Mo, H. J.: 2006, *MNRAS* **366**, 2

White, S. D. M.: 1979, *MNRAS* **186**, 145

White, S. D. M. & Frenk, C. S.: 1991, *ApJ* **379**, 52

White, S. D. M. & Rees, M. J.: 1978, *MNRAS* **183**, 341

Wolf, C., Meisenheimer, K., Rix, H.-W., Borch, A., Dye, S., & Kleinheinrich, M.: 2003, *A&A* **401**, 73

Yang, X., Mo, H. J., Jing, Y. P., van den Bosch, F. C., & Chu, Y.: 2004, *MNRAS* **350**, 1153

Yang, X., Mo, H. J., & van den Bosch, F. C.: 2003, *MNRAS* **339**, 1057

Yang, X., Mo, H. J., & van den Bosch, F. C.: 2006, *ApJL* **638**, L55

Yang, X., Mo, H. J., van den Bosch, F. C., & Jing, Y. P.: 2005, *MNRAS* **356**, 1293

York, D. G., Adelman, J., Anderson, J. E., Anderson, S. F., Annis, J., Bahcall, N. A., Bakken, J. A., Barkhouser, R., Bastian, S., Berman, E., Boroski, W. N., Bracker, S., Briegel, C., Briggs, J. W., Brinkmann, J., Brunner, R., Burles, S., Carey, L., Carr, M. A., Castander, F. J., Chen, B., Colestock, P. L., Connolly, A. J., Crocker, J. H., Csabai, I., Czarapata, P. C., Davis, J. E., Doi, M., Dombeck, T., Eisenstein, D., Ellman, N., Elms, B. R., Evans, M. L., Fan, X., Federwitz, G. R., Fiscelli, L., Friedman, S., Frieman, J. A., Fukugita, M., Gillespie, B., Gunn, J. E., Gurbani, V. K., de Haas, E., Haldeman, M., Harris, F. H., Hayes, J., Heckman, T. M., Hennessy, G. S., Hindsley, R. B., Holm, S., Holmgren, D. J., Huang, C.-h., Hull, C., Husby, D., Ichikawa, S.-I., Ichikawa, T., Ivezić, Ž., Kent, S., Kim, R. S. J., Kinney, E., Klaene, M., Kleinman, A. N., Kleinman, S., Knapp, G. R., Korienek, J., Kron, R. G., Kunszt, P. Z., Lamb, D. Q., Lee, B., Leger, R. F., Limmongkol, S., Lindenmeyer, C., Long, D. C., Loomis, C., Loveday, J., Lucinio, R., Lupton, R. H., MacKinnon, B., Mannery, E. J., Mantsch, P. M., Margon, B., McGehee, P., McKay, T. A., Meiksin, A., Merelli, A., Monet, D. G., Munn, J. A., Narayanan, V. K., Nash, T., Neilsen, E., Neswold, R., Newberg, H. J.,

Nichol, R. C., Nicinski, T., Nonino, M., Okada, N., Okamura, S., Ostriker, J. P., Owen, R., Pauls, A. G., Peoples, J., Peterson, R. L., Petravick, D., Pier, J. R., Pope, A., Pordes, R., Prosapio, A., Rechenmacher, R., Quinn, T. R., Richards, G. T., Richmond, M. W., Rivetta, C. H., Rockosi, C. M., Ruthmansdorfer, K., Sandford, D., Schlegel, D. J., Schneider, D. P., Sekiguchi, M., Sergey, G., Shimasaku, K., Siegmund, W. A., Smee, S., Smith, J. A., Snedden, S., Stone, R., Stoughton, C., Strauss, M. A., Stubbs, C., SubbaRao, M., Szalay, A. S., Szapudi, I., Szokoly, G. P., Thakar, A. R., Tremonti, C., Tucker, D. L., Uomoto, A., Vanden Berk, D., Vogeley, M. S., Waddell, P., Wang, S.-i., Watanabe, M., Weinberg, D. H., Yanny, B., & Yasuda, N.: 2000, *AJ* **120**, 1579

Zehavi, I., Weinberg, D. H., Zheng, Z., Berlind, A. A., Frieman, J. A., Scoccimarro, R., Sheth, R. K., Blanton, M. R., Tegmark, M., Mo, H. J., Bahcall, N. A., Brinkmann, J., Burles, S., Csabai, I., Fukugita, M., Gunn, J. E., Lamb, D. Q., Loveday, J., Lupton, R. H., Meiksin, A., Munn, J. A., Nichol, R. C., Schlegel, D., Schneider, D. P., SubbaRao, M., Szalay, A. S., Uomoto, A., & York, D. G.: 2004, *ApJ* **608**, 16

Zehavi, I., Zheng, Z., Weinberg, D. H., Frieman, J. A., Berlind, A. A., Blanton, M. R., Scoccimarro, R., Sheth, R. K., Strauss, M. A., Kayo, I., Suto, Y., Fukugita, M., Nakamura, O., Bahcall, N. A., Brinkmann, J., Gunn, J. E., Hennessy, G. S., Ivezić, Ž., Knapp, G. R., Loveday, J., Meiksin, A., Schlegel, D. J., Schneider, D. P., Szapudi, I., Tegmark, M., Vogeley, M. S., & York, D. G.: 2005, *ApJ* **630**, 1

Zel'dovich, Y. B.: 1970, *A&A* **5**, 84

Zel'dovich, Y. B.: 1972, *MNRAS* **160**, 1P

Zhang, J. & Hui, L.: 2006, *ApJ* **641**, 641

Zheng, Z.: 2004, *ApJ* **610**, 61

Zheng, Z., Berlind, A. A., Weinberg, D. H., Benson, A. J., Baugh, C. M., Cole, S., Davé, R., Frenk, C. S., Katz, N., & Lacey, C. G.: 2005, *ApJ* **633**, 791

Zheng, Z., Tinker, J. L., Weinberg, D. H., & Berlind, A. A.: 2002, *ApJ* **575**, 617

Zhu, G., Zheng, Z., Lin, W. P., Jing, Y. P., Kang, X., & Gao, L.: 2006, *ApJL* **639**, L5

Zwicky, F.: 1937, *ApJ* **86**, 217

Appendix A | *Simulation rescaling*

A.1 Introduction

In studying the cosmological dependence of, for example, clustering statistics, it is convenient to have N-body simulations in a variety of cosmologies. Then mock galaxy catalogues etc. can be constructed for these different cosmologies and their properties studied.

We describe here some methods by which a simulation in one cosmology can be used to mimic a simulation in a different cosmology sufficiently well that the errors are not significant in the context of properties of the mock catalogues. Fewer computationally expensive N-body simulations are then required, which may be a considerable saving if the simulations are large. Where relevant, we concentrate on rescaling the output from the N-body code GADGET (Springel et al., 2001b).

A.2 Preliminaries

Let comoving distances be denoted by x, and physical distances be denoted by $r = ax$, so that a is the conventional scale factor, normalized such that its value at redshift zero is $a_0 = 1$. Let the Hubble Parameter $H(a) = H_0 h(a)$, where $H_0 = 100$ km s^{-1} Mpc^{-1} and the present value of the Hubble Parameter is $H(1) = H_0 h_0$, that is $h_0 = h(1)$.

Now we may write the critical density

$$\rho_{\rm crit}(a) = \frac{3H_0^2 h^2(a)}{8\pi G} \quad . \tag{A.1}$$

By definition, we have $\rho = \rho_{\rm crit}\Omega$. Below, we will consider ρ without a subscript to be the matter density and Ω to be the ratio of matter density to critical density. A subscript zero denotes their values at redshift zero as is conventional. Then,

$$\rho(a) = \frac{\rho_0}{a^3} = \rho_{\rm crit}(a)\Omega(a) = \frac{3H_0^2}{8\pi G} h^2(a)\Omega(a) \quad , \tag{A.2}$$

that is,

$$h^2(a)a^3\Omega(a) = \frac{8\pi G}{3H_0^2}\rho_0 \tag{A.3}$$

$$= h_0^2\frac{8\pi G}{3H_0^2h_0^2}\rho_0 \tag{A.4}$$

$$= h_0^2\Omega_0 \tag{A.5}$$

which is a constant in any given cosmology.

Consider an isolated halo in its centre-of-mass frame in this cosmology, consisting of particles labelled by $i = 1, 2, \ldots, n$. Its potential energy is given by

$$E_{\rm P} = -\sum_i\sum_{j>i}\frac{Gm_im_j}{|r_i - r_j|} \tag{A.6}$$

$$= -\frac{1}{2a}\sum_i\sum_{j\neq i}\frac{Gm_im_j}{|x_i - x_j|} \quad , \tag{A.7}$$

where we treat the positions as scalar quantities for clarity, since the generalization to three dimensions is trivial. Its kinetic energy is then given by

$$E_{\rm K} = \frac{1}{2}\sum_i m_i\left(\frac{{\rm d}r_i}{{\rm d}t}\right)^2 \tag{A.8}$$

$$= \frac{1}{2}\dot{a}^2\sum_i m_i\left(x_i + a\frac{{\rm d}x_i}{{\rm d}a}\right)^2 \tag{A.9}$$

$$= \frac{1}{2}a^2H_0^2h^2(a)\sum_i m_i\left(x_i + a\frac{{\rm d}x_i}{{\rm d}a}\right)^2 \tag{A.10}$$

after some elementary manipulation.

There is a slight complication, in that it is conventional to use a system of units in which

$$m_i = \frac{\widetilde{m}_i}{h_0} \quad \text{and} \quad x_i = \frac{\tilde{x}_i}{h_0} = ar_i = \frac{a\tilde{r}_i}{h_0} \quad . \tag{A.11}$$

In this system, the energies are also scaled in the same way, $\widetilde{E} = h_0E$. Then,

$$\widetilde{E}_P = \frac{-1}{2a}\sum_i\sum_{j\neq i}\frac{G\widetilde{m}_i\widetilde{m}_j}{|\tilde{x}_i - \tilde{x}_j|} \tag{A.12}$$

and

$$\widetilde{E}_K = \frac{1}{2}\left(\frac{aH_0h(a)}{h_0}\right)^2\sum_i\widetilde{m}_i\left(\tilde{x}_i + a\frac{{\rm d}\tilde{x}_i}{{\rm d}a}\right)^2 \quad . \tag{A.13}$$

GADGET stores the particle positions $\tilde{x}$, using units of h_0^{-1} Mpc. Storing the velocities is slightly more problematic. In fact, the quantity stored is

$$w = a^{1/2}H_0h(a)a\frac{{\rm d}x}{{\rm d}a} \quad , \tag{A.14}$$

which corresponds to peculiar, physical velocities in km s^{-1}, divided by $a^{1/2}$. The factor of $a^{1/2}$ is introduced for numerical convenience — velocities are expected to scale with $a^{1/2}$ in linear theory, so dividing by this factor ensures that velocities do not change by several orders of magnitude during the calculation which could introduce numerical errors. We can see this correspondence between w and peculiar, physical velocities by observing that

$$\frac{\mathrm{d}r}{\mathrm{d}t} = \frac{\mathrm{d}(ax)}{\mathrm{d}t} \tag{A.15}$$

$$= \dot{a}x + a\frac{\mathrm{d}x}{\mathrm{d}t} \tag{A.16}$$

$$= \dot{a}x + a\dot{a}\frac{\mathrm{d}x}{\mathrm{d}a} \tag{A.17}$$

$$= \dot{a}x + a^2 H(a)\frac{\mathrm{d}x}{\mathrm{d}a} \tag{A.18}$$

$$= \dot{a}x + a^{1/2}w \tag{A.19}$$

where the $\dot{a}x$ term corresponds to the Hubble flow.

So, we may now write the expressions to compute the kinetic and potential energy of our isolated halo in terms of the quantities w, $\tilde{x}$ and $\tilde{m}$, where w and $\tilde{x}$ are as above and $\tilde{m}$ is in units of h_0^{-1} M$_\odot$, such that the energies are numerically in units of h_0^{-1} M$_\odot$ (100 km s^{-1})^2 :

$$\widetilde{E}_P = -\frac{1}{a}\sum_i \sum_{j>i} \frac{G\tilde{m}_i\tilde{m}_j}{|\tilde{x}_i - \tilde{x}_j|} \quad ; \tag{A.20}$$

$$\widetilde{E}_K = \frac{1}{2}\sum_i \tilde{m}_i \left(\frac{h(a)}{h_0}a\tilde{x}_i + \frac{a^{1/2}w}{H_0}\right)^2 \quad . \tag{A.21}$$

Note that here $G = 4.301 \times 10^{-13}$ M$_\odot^{-1}$ Mpc (100 km s^{-1})^2.

These expressions will be useful in checking the validity of rescalings. The virial theorem indicates that, for an isolated halo in equilibrium,

$$\frac{2\widetilde{E}_K}{|\widetilde{E}_P|} \approx 1 \quad , \tag{A.22}$$

so that an analytic check on a rescaling of particle positions, velocities and masses is that the ratio of the kinetic and potential energies of halos is preserved. A numerical check on our results is that (A.22) holds before and after rescaling.

A.3 Simple Relabelling

Possibly the simplest useful rescaling to consider is one in which a $z > 0$ output with scale factor a_i from some simulation is treated as a $z = 0$ output from a simulation in a different cosmology. We wish the scale factor, a, to retain the conventional normalization,

i.e. $a_0 = 1$. So we must have $a \to 1$ under rescaling. Since the value of h_0 in the original simulation was presumably chosen to agree with available data, we also require $h_0 \to h_0$. Similarly, the peak in the initial power spectrum of density fluctuations will change unless $x \to x$. Then inspection of, e.g., (A.9) suggests that we also require

$$a\frac{\mathrm{d}x}{\mathrm{d}a} \to a\frac{\mathrm{d}x}{\mathrm{d}a} \quad . \tag{A.23}$$

This does not mean that the transformation is entirely trivial. If $\Omega \neq 1$ then the matter density in a simulation is a function of a, $\Omega \equiv \Omega(a)$. Since the point of doing the rescaling is that we acquire a simulation in a different cosmology, we preserve the value of Ω from the output we have rescaled; this becomes the value of Ω_0 in the new file. In other words, $\Omega_0 \to \Omega(a_\mathrm{i})$. For a flat, ΛCDM cosmology, this means the rescaled simulation has a higher Ω_0 than the old simulation. Since we have preserved our length scales, this implies that the particle mass must scale as

$$m \to \frac{\Omega(a_\mathrm{i})}{\Omega_0} m \quad , \tag{A.24}$$

where here Ω_0 refers to the $z = 0$ matter density before rescaling. Since (A.23) implies that $a^{-1/2}w/h(a)$ is also preserved, we require

$$w \to a_\mathrm{i}^{-1/2} \frac{h_0}{h(a_\mathrm{i})} w = a_\mathrm{i} \left(\frac{\Omega(a_\mathrm{i})}{\Omega_0}\right)^{\frac{1}{2}} w \quad , \tag{A.25}$$

where we have used (A.5) to infer the equality on the right-hand side.

It remains to check that the kinetic and potential energies in an isolated halo scale the same way under this scheme. Substituting the new quantities into (A.20) and (A.21), and using (A.5) again, reveals that

$$E_K \to a_\mathrm{i} \left(\frac{\Omega(a_\mathrm{i})}{\Omega_0}\right)^2 E_K \quad \text{and} \quad E_P \to a_\mathrm{i} \left(\frac{\Omega(a_\mathrm{i})}{\Omega_0}\right)^2 E_P \quad , \tag{A.26}$$

so that we do indeed have consistency. Note that since h_0 is preserved, $\{m, x, E\}$ scale in the same way as $\{\widetilde{m}, \tilde{x}, \widetilde{E}\}$. Therefore the above gives us directly a prescription for how to alter the data in a GADGET output file to achieve the desired rescaling, bearing in mind that the output at any time contains the values of Ω_0 and h_0 — the values of $\Omega(a)$ and $h(a)$ at the final time — and not their instantaneous values at the output time. It is also worth noting that it is conventional to label a simulation by the value of σ_8 — the scale of mass fluctuations in spheres of 8 h^{-1} Mpc according to linear theory — at the final time. However, this quantity also evolves with time, $\sigma_8 \equiv \sigma_8(a)$, becoming larger as structure forms in the simulation. So, $\sigma_8(z = 0) \to \sigma_8(a_\mathrm{i})$, where $\sigma_8(a_\mathrm{i})$ can be calculated in linear theory.

A.4 More General Relabelling

Suppose that instead of relabelling the $a = a_\mathrm{i}$ output as an $a = 1$ output we decide to relabel the $a = a_\mathrm{i}$ output as an $a = a_\mathrm{f}$ output, for some $a_\mathrm{f} \neq a_\mathrm{i}$. A little more care in notation is required, but the transformations generalize as follows, with primes denoting quantities in the rescaled output:

$$a \rightarrow a' \tag{A.27}$$

$$h_0 \rightarrow h_0' = h_0 \tag{A.28}$$

$$h(a) \rightarrow h'(a') \quad \text{such that } h_0' = h_0 \tag{A.29}$$

$$x \rightarrow x' = x \tag{A.30}$$

$$a\frac{\mathrm{d}x}{\mathrm{d}a} \rightarrow a'\frac{\mathrm{d}x'}{\mathrm{d}a'} = a\frac{\mathrm{d}x}{\mathrm{d}a} \tag{A.31}$$

$$\Omega(a) \rightarrow \Omega'(a') = \Omega(a) \tag{A.32}$$

$$\Omega_0 \rightarrow \Omega_0' \quad \text{such that the above holds} \tag{A.33}$$

$$w \rightarrow w' = \frac{h'(a')}{h(a)}\left(\frac{a'}{a}\right)^{\frac{1}{2}} w \tag{A.34}$$

$$= \left(\frac{\Omega_0'}{\Omega_0}\right)^{\frac{1}{2}} \frac{a}{a'} w \quad \text{using (A.5)} \tag{A.35}$$

$$m \rightarrow m' = \frac{\Omega_0'}{\Omega_0} m \quad . \tag{A.36}$$

Then it is easily checked, again using (A.5), that the kinetic and potential energies scale as

$$E \rightarrow E' = \frac{a}{a'}\left(\frac{\Omega_0'}{\Omega_0}\right)^2 E \quad . \tag{A.37}$$

A.5 Rescaling Ω

It has been observed that rescaling some parameters in cosmological simulations results, at least to first order, in a relatively straightforward scaling of some observables. For example, Zheng et al. (2002) state (note that they write Ω_m where elsewhere in this appendix we write Ω_0):

> For fixed linear theory $P(k)$, the effect of changing Ω_m is simple: the halo mass scale M_* shifts in proportion to Ω_m, pairwise velocities (at fixed M/M_*) are proportional to $\Omega_\mathrm{m}^{0.6}$, and halo clustering at fixed M/M_* is unchanged.

While this is an empirical effect rather than a consequence of an analytic calculation, we hope that the scaling is good enough so that our catalogues will still be sufficiently

accurate when we rescale our simulations such that σ_8 remains constant but Ω_0 changes. The factor of $\Omega_{\rm m}^{0.6}$ is expected since, to a good approximation,

$$\frac{\mathrm{d}\ln D}{\mathrm{d}\ln a} \approx \Omega_{\rm m}^{0.6} \quad , \tag{A.38}$$

where D is the linear growth factor (Peebles, 1980; Lahav et al., 1991).

For example, suppose we choose our simulation such that one output has some fiducial values of Ω_0 and σ_8, once we take care of the relabelling described above. Presumably these values have been chosen to agree at some level with observations. Note, now, that Ω_0 and σ_8 may be constrained via some function of both parameters, for example using the observed abundance of clusters (Eke et al., 1996). It seems sensible, then, to generate an ensemble of catalogues such that they are all consistent with a cluster normalization condition, where the curve of allowed values of (Ω_0, σ_8) passes through the fiducial point. This curve is not the same as the curve traced out by (Ω_0, σ_8) as the dark matter distribution in the simulation evolves. Therefore to generate our ensemble of catalogues we need not only to relabel the simulation outputs according to our analytic scheme above, but also to rescale the outputs (preferably by a small amount) so that the members of the ensemble lie on a convenient grid or on a suitable normalization curve. This is the situation encapsulated in Fig. 4.2.

It is convenient to achieve this rescaling in practice by altering the particle mass to change Ω_0, and compensating by changing particle velocities. So,

$$\Omega_0 \rightarrow \Omega_0' \tag{A.39}$$

$$m \rightarrow m' = \frac{\Omega_0'}{\Omega_0} m \tag{A.40}$$

$$w \rightarrow w' = \left(\frac{\Omega_0'}{\Omega_0}\right)^{0.6} w \tag{A.41}$$

Note that although we would require w to scale as $(\Omega_0'/\Omega_0)^{0.5}$ to maintain the virial relation, the scaling we use is close to the linear theory prediction, and that in practice we only ever intend to rescale by small amounts. This is helped by the fact that the cluster normalization curve and the curve describing the evolution of the simulation parameters look qualitatively similar close to the fiducial point if we choose sensible parameter values.